REPORT NO. 2

MELT-GROWN OXIDE-METAL COMPOSITES

FINAL TECHNICAL REPORT

(Period: 10 June 1970 to 9 June 1971)

Project Director
A. T. Chapman

Principal Investigators
J.F. Benzel R.J. Gerdes
R.K. Feeney J.W. Hooper

Sponsored By
Advanced Research Projects Agency
Department of Defense
ARPA ORDER NO. 1637

Contract No. DAAHOI-70-C-1157

July 1971

1971

School of Ceramic Engineering
GEORGIA INSTITUTE OF TECHNOLOGY
Atlanta, Georgia

[redacted]

Report No. 2

MELT-GROWN OXIDE-METAL COMPOSITES

FINAL TECHNICAL REPORT

(Period: 10 June 1970 - 9 June 1971)

from

THE SCHOOL OF CERAMIC ENGINEERING

GEORGIA INSTITUTE OF TECHNOLOGY

ATLANTA, GEORGIA 30332

PROJECT DIRECTOR: A. T. CHAPMAN

July 1971

SPONSORED BY

ADVANCED RESEARCH PROJECTS AGENCY

DEPARTMENT OF DEFENSE

ARPA ORDER NO. 1637

CONTRACT NO. DAAHOI-70-C-1157

PERSONNEL PARTICIPATING IN PROJECT

Principal Investigators	Graduate Students
J. F. Benzel	N. E. Grynkewich
R. K. Feeney	C. C. Jen
R. J. Gerdes	T. A. Johnson
J. W. Hooper	Y. S. T. Lin
	W. L. Ohlinger
	J. Pepper
	G. T. Tucker
	M. D. Watson

TABLE OF CONTENTS

TABLE OF CONTENTS (Cont.)

LIST OF ILLUSTRATIONS

LIST OF ILLUSTRATIONS (Cont.)

LIST OF ILLUSTRATIONS (Cont.)

LIST OF ILLUSTRATIONS (Cont.)

LIST OF ILLUSTRATIONS (Cont.)

LIST OF TABLES

FOREWORD

This Research was sponsored by the ADVANCED RESEARCH PROJECTS AGENCY of the DEPARTMENT OF DEFENSE under ARPA ORDER NO. 1637 and was monitored by the U.S. ARMY MISSILE COMMAND under Contract No. DAAHOI-70-C-1157.

Views and conclusions expressed herein are the primary responsibility of the author or the contractor and should not be interpreted as representing the official opinion or policy of USAMICOM, ARPA, DOD or any other agency of the Government.

ABSTRACT

Research was initiated to understand and control the parameters leading to the successful growth of refractory oxide-metal composites consisting of small metal fibers uniformly embedded in the oxide matrix, and to evaluate the electron emission performance of these structures. Numerous oxides, binary oxide compounds, oxide-oxide and oxide-metal mixtures were tested to determine their suitability for induction melting using rf frequencies between 3 and 32 mhz. Procedures employing scanning electron microscopy and x-ray diffraction were developed to characterize oxide-metal composite samples. Metallic fiber shapes have been related to crystallographic morphology. Mutual oxide-metal orientations were determined in selected UO_2-W samples. The influence of growth rate on W fiber density and size was studied in the system UO_2-W. Extensive areas of uniform W fiber growth were achieved in the stabilized ZrO_2-W system. Chemical etching techniques have been developed to shape tungsten pins for enhanced electron field emission. A theoretical analysis of expected electron field emission from an array of metallic pins has been performed using pin geometries and electrical variables. Suitably prepared UO_2-W samples were tested in a simple diode geometry and field emission performance measured as a function of voltage and interelectrode spacing. Post emission damage to the composite structures has been analyzed.

SECTION I

INTRODUCTION

This is the Final Report for the "Melt-Grown Oxide-Metal Composite" Research Project, (DAAHOI-70-C-1157) covering the contract period 10 June 1970 through 9 June 1971. Previously Report No. 1, Semi-Annual Technical Report dated January 1971[1], was issued describing the initial results obtained in this study. The information contained in this Final Report will emphasize work accomplished since the initial report, although some of the earlier information will be repeated to provide informational continuity.

The techniques used to grow the refractory oxide-metal composites containing many millions of less than 1 μ diameter tungsten fibers per square centimeter, uniformly distributed in an oxide matrix, were reviewed in the Semi-Annual Report[1] and will be included again as it provides valuable background information for interpreting the various sections of this Report. The major research objectives in the different project areas are also outlined in this section.

A modified floating-zone technique has been used to grow single crystals of refractory oxides and is employed to grow the

oxide-metal composites. In this technique pressed rods of the oxide-metal mixture are sintered inside rf heated molybdenum tubes in an inert atmosphere to densify and preheat the material. (A typical growth arrangement is shown schematically in Figure 30 of this Report.) After the initial heating, which also serves to increase the electrical conductivity of the oxides, the molybdenum tube heaters are separated to expose approximately 2 cm of the rod to an rf field of 3 to 30 megahertz (mhz), depending on the material to be melted. The concurrent increase of temperature, electrical conductivity and resistance heating continues until the interior of the rod melts at temperatures up to 3000° C. The high radiant heat loss from the surface and the inherent low thermal conductivity of the oxides maintains the skin of the rod well below the eutectic temperature of the mixture. Composite growth is obtained by moving the molten zone up through the rod. In practice a cavity is generated in the molten zone because of the difference in density between the initial polycrystalline rod and solidified composite. During growth the oxide and metal melts from the roof of this cavity and solidifies at the base.

During the growth of pure oxides it was found advantageous to rotate the rods at speeds above 300rpm. During rotation the molten material is centrifugally cast against the sides of the cavity; thus, the liquid-solid interface is modified so that crystallization in the center of the rod leads solidification near the circumference of the rod and promotes the uniform growth

of one crystallographic orientation across the entire melted zone. The need for rotation during the growth of oxide-metal composites is unresolved at present because uniform eutectic structures have been successfully obtained both with and without rotation. Results shown in Section IV, Part B of this Report indicate that the mechanical mixing of the molten liquid achieved through rotation may indeed influence the oxide-metal geometry, especially with non-eutectic oxide-rich mixtures. To date, well-ordered oxide-metal structures have been achieved in the UO_2-W and stabilized ZrO_2-W systems.

The primary technical objective of the project is to understand the solidification processes leading to coupled growth and ordered microstructures after melting oxide-metal mixtures to successfully produce useable samples of these composites and evaluate their potential for practical applications. The evaluation of these composites for electron emitter applications is being investigated initially because structures containing between 4 and 50 million exposed W fibers per square centimeter can readily be attained.

The research program was initially divided into five areas; however, two of the original topics are combined in this Report for continuity purposes and the titles of several areas have been modified to more adequately reflect the nature of the research within these subdivisions. It should be noted that

although this is the Final Report, experimental work is continuing in all of the project areas.

A. INDUCTION COUPLING AND SOLIDIFICATION BEHAVIOR OF OXIDES AND OXIDE-METAL MIXTURES

A study of the chemical, thermal and mechanical variables active during solidification of numerous oxides and oxide-metal systems was performed to study the parameters which control successful oxide-metal composite growth and to find new candidate systems suitable for ordered eutectic growth.

B. STRUCTURAL AND CHEMICAL CHARACTERIZATION OF OXIDE-METAL COMPOSITES

The composite growth morphology with emphasis on the tungsten fiber morphology and oxide-metal orientation relationships were studied using scanning electron microscopy and x-ray diffraction techniques. The SEM information was used extensively to study the composite growth geometries as a function of growth parameters and to characterize samples for emission tests and post-emission damage.

C. COMPOSITE GROWTH IN OXIDE-METAL SYSTEMS AND THE FORMATION OF OPTIMUM EMITTING ARRAYS

Growth experiments were performed in systems which readily

form ordered structures (e.g. W with UO_2 and ZrO_2) to establish the influence that controllable growth parameters, such as oxide-metal ratio and growth rate, exert on tungsten fiber density and size. The existing microstructures were altered using chemical etching techniques to produce fiber shapes that possess optimum emitting characteristics.

D. FIELD EMISSION THEORY AND EXPERIMENTAL RESULTS

Current mathematical descriptions of the electron emission from point sources were used to calculate pin array geometries yielding optimum emission performance. Suitably prepared UO_2-W composites were tested in diodes to evaluate their use as field emitters. The emission performance was studied as a function of fiber array geometry, field strength and interelectrode spacing. The experimental information was correlated with the theoretical analysis to interpret the actual emitter behavior.

SECTION II

INDUCTION COUPLING AND SOLIDIFICATION BEHAVIOR OF OXIDES AND OXIDE-METAL MIXTURES

Melting and subsequent controlled solidification of refractory oxides and oxide-metal mixtures have been previously accomplished[2,3,4,5] using high (4 to 30 mhz) frequency rf heating. This technique is limited to systems that have sufficient electrical conductivity at elevated temperatures to support eddy-current heating at the level required to produce internal melting. During this contract period a number of oxides, binary oxide compounds, oxide-oxide mixtures and oxide-metal mixtures have been tested to determine their suitability for internal melting using the rf coupling scheme.

All of the materials studied were made into 3/4 inch diameter pellets by pressing -325 mesh powders in a two punch steel die at about 2500 psi. These prepressed cylinders were then placed in an evacuated rubber envelope and hydrostatically pressed to 50,000 psi to increase their density. Final pellet height varied from 1/2 to 1 1/2 inches.

Before an attempt was made to rf couple to any pellet, it was either sintered in a ceramic processing furnace or in a one inch diameter inductively heated susceptor cylinder of SiC

or glassy carbon. Silicon carbide susceptor tubes were used to preheat sintered test pellets to temperatures between 1000° and 1670° C in air. Higher preheat temperatures (up to 1900° C) were achieved by using glassy carbon tube susceptors in an atmosphere chamber (see Figure 30) containing a dynamic H_2-N_2 atmosphere. The purpose of preheating the test pellets was to increase their electrical conductivity prior to subjecting them to the rf coupling test. The susceptor tubes were located inside the work coil of an rf generator during the preheat treatment, which allowed the melting behavior of the test material to be determined by simply removing the hot susceptor from around the test pellet and thereby exposing it to the rf field.

Previous work[2,3] in which oxide-metal mixtures have been internally melted by rf fields and then unidirectionally solidified have produced unique composite structures consisting of well-ordered metal fibers approximately 1μ in diameter embedded in an oxide matrix. In the above investigations the only metal utilized was tungsten because of the initial success with this metal.

During the second half of this contract period a limited number of experiments designed to determine the compatability of various refractory metals other than tungsten as the metal component for this type of oxide-metal composite were carried out. These tests were made in H_2-N_2 atmospheres using the chamber shown in Figure 30 and either Mo or SiC tubes as preheat susceptors.

A. BEHAVIOR OF OXIDES, OXIDE COMPOUNDS AND OXIDE MIXTURES

A compilation of the oxide materials coupling test results including preheat temperatures, rf coupling, melting behavior and miscellaneous comments for the three classes of materials - oxides, oxide compounds and oxide mixtures - are presented in Tables I, II, and III respectively.

Of the single oxides tested (Table I), only CeO_2 formed a stable molten zone. Cr_2O_3, TiO_2 and NiO might also be useful composite candidates if their stoichiometry problems can be overcome. Polished cross sections of pellets of these materials are shown in Figure 1. Figure 2 is a micrograph of the dark area of the CeO_2 pellet which shows this area to be a two phase region.

Of the binary oxide compounds tested, Table II, nickel titanate and iron titanate were the only ones to form a stable molten zone. As can be seen in Figure 3, the stoichiometry of that portion of the $NiTiO_3$ pellet that was at the highest temperature has changed. The iron titanate pellet cracked during preheating, and crossectioning revealed (Figure 3) that the molten zone was porous.

TABLE I

INDUCTION MELTING BEHAVIOR OF SINGLE OXIDES AT 27 mhz.

Oxide	Preheating °C	Behavior rf Coupled	Melted	Comments or Problems
Al_2O_3	1600	No	No	-
Al_2O_3	1600	No(1)	No	This pellet had been hot pressed to a density of 3.10 gms/cm^2. Pellet cracked during preheat.
CdO	1300	Yes	No	Sublimed.
CeO_2	1425	Yes	Yes	Molten area turned blue indicating reduction of the oxygen cerium ratio.
Cr_2O_3	1670	Yes	Yes	Stoichiometry change occurred, Cr metal observed in polished specimen.
Gd_2O_3	1540	No(1)	No	Broke in half during cooling.
MgO	1600	No	No	-
NiO	1250	Yes	Yes	Surface of pellet melted, sample was reduced, Ni metal observed in polished specimen.
Pr_2O_3	1600	Yes(1)	Yes	Only very small area melted, sample cracked on cooling.
SrO	1550	No	No	-
TiO_2	1580	Yes(2)	Yes	Molten zone melted through to surface and released liquid, some reduction observed in molten zone.
ThO_2	1900	No(3)	No	Cracked on cooling.
WO_3	1300	Yes	Yes	Liquid released through cracks, areas of different oxidation states present.

Table I Continued

Oxide	Preheating °C	Behavior rf Coupled	Melted	Comments or Problems
Y_2O_3	1600	Slightly	No	-
Y_2O_3	1900	No(3)	No	H_2-N_2 atmosphere.
ZnO	1400	Yes	?	Sublimed.

(1) A 32 mhz field was used for this test.

(2) A 9 mhz induction generator was used instead of the usual 27 mhz generator.

(3) A 7.6 mhz field was used for this test.

TABLE II

INDUCTION MELTING BEHAVIOR OF BINARY OXIDE COMPOUNDS AT 27 mhz.

Oxide Compound	Preheating °C	Behavior rf Coupled	Melted	Comments or Problems
Al_4CaO_7	1560	Very Slightly	No	Cracked on cooling.
Al_2MgO_4	1650	No	No	Spinel.
$Al_4Mg_2Si_5O_{18}$	1500	No	No	Cordierite.
Al_2TiO_5	1650	No	No	-
$BaFe_2O_4$	1010	No	No	Cracked badly on cooling.
$BaFe_{12}O_{19}$	1250	Yes	Yes	Molten material ejected through cracks.
$BaNiO_2$	1150	Yes	?	Nickel metal coating formed just below sample surface.
$BaO \cdot Fe_2O_3$	1150	-	-	Melted during preheat, resulting solid very brittle.
$BaSnO_3$	1150	No	No	Cracked badly during firing.
$BaTiO_3$	1530	Yes(1)	No	Must be preheated very slowly to prevent cracking.
$BaZrO_3$	1520	No	No	Cracked badly on cooling.
$BaZrO_3$	1900	Yes(2)	No	H_2-N_2 atmosphere, considerable smoking after coupling occurred, at least three different colored areas present after cooling, arcing caused the experiment to be terminated.
$CaTiO_3$	1600	No(3)	No	-

Table II Continued

Oxide Compound	Preheating °C	Behavior rf Coupled	Melted	Comments or Problems
$CeTiO_4$	1340	No(3)	No	Cracked badly on cooling.
$Cr_2Y_2O_6$	1610	Yes	No	-
Fe_2TiO_5	1360	Yes	Yes	Cracked during preheating.
$MgTiO_3$	1580	No(3)	No	Cracked badly on cooling.
$NiTiO_3$	1250	Yes(3)	Yes	Molten zone had become dark brown color in contrast to its original yellow color.
$SnTiO_4$	1250	No(3)	No	-
$SrTiO_3$	1550	No	No	Broke up on cooling.
$ZrTiO_4$	1550	No	No	-

(1) A 9 mhz induction generator was used instead of the usual 27 mhz generator.

(2) A 8 mhz field was used for this test.

(3) A 32 mhz field was used for this test.

TABLE III

INDUCTION MELTING BEHAVIOR OF OXIDE MIXTURES AT 27 mhz.

Oxide Mixture	Preheating °C	Behavior rf Coupled	Melted	Comments or Problems
Al_2O_3 + 5%NiO	1550	No	No	Pellet broke up during cooling.
Al_2O_3 + 5%Fe_2O_3	1620	No	No	Broke during cooling.
Al_2O_3 + 10%Pr_2O_3	1550	No	No	Prefired in H_2 atmosphere, broke on cooling.
Al_2O_3 + 10%Co_3O_4	1550	No	No	-
Al_2O_3 + 60%BaO	1600	No	No	-
Al_2O_3 + 50%Cr_2O_3	1650	No	No	-
Al_2O_3 + 50%Cr_2O_3	none	Yes(1)	No	Same pellet as above, but hot pressed in graphite die to about 1550°C at 4500 psi. Broke due to thermal stresses produced by its rapid heating.
Al_2TiO_5 + 5%La_2O_3	1600	No	No	-
Al_2TiO_5 + 10%La_2O_3	1600	No	No	-
Al_2TiO_5 + 1%Fe_2O_3	1650	No	No	-
Al_2TiO_5 + 2%Fe_2O_3	1650	No	No	-

Table III Continued

Oxide Mixture	Preheating °C	Behavior rf Coupled	Melted	Comments or Problems
NiO + 20%MgO	1600	Yes	No	NiO became partially reduced.
NiO + 40%MgO	1600	Yes	No	Same as 20% MgO.
NiO + 60%MgO	1600	Yes	No	Temperature stabilized at 1000°C.
NiO + 80%MgO	1600	Yes	No	Same as 60% MgO.
ZnO + 18%Al_2O_3	1400	Yes	Yes	Sublimed, melted zone very porous. Melting point of this eutectic is listed as 1720°C.
ZnO + 31%Nb_2O_5	1250	No[2]	No	Melting point of this eutectic is listed as 1285°C.
ZnO + 30%TiO_2	1400	Yes	Yes	Liquid expelled through walls of pellet. Melting point of this eutectic is listed as 1549°C.
ZnO + 20%TiO_2	1450	Yes	Yes	Interior became molten in only isolated areas and liquid was expelled through walls of pellet.
ZrO_2 + 5%CaO	1580	Yes	Yes	Stable internal molten zone.
ZrO_2 + 10%Y_2O_3	1600	Yes	Yes	Stable internal molten zone established after 3 minute exposure to rf field.
ZrO_2 + 15%Y_2O_3	1600	Yes	Yes	Stable internal molten zone.

Table III Continued.

(1) A 33 mhz field was used for this test.

(2) A 32 mhz field was used for this test.

The stabilized zirconia mixtures described in Table III all formed stable internal molten zones (see Figure 4) when subjected to a 27 mhz field. If the high MgO compositions of the NiO-MgO solid solution series were preheated to a higher temperature, they also might be good candidates for internal melting. ZnO readily coupled to the rf field but sublimed badly prior to melting (see Table I). The four ZnO mixtures shown in Table III were an attempt to create a stable eutectic melt below the sublimation point of ZnO. The ZnO eutectics involving Al_2O_3 and TiO_2 easily coupled but the melting point of the eutectic composition was too high to prevent the sublimation of ZnO from the samples. The Nb_2O_5-ZnO eutectic composition did not couple to a 32 mhz field even when preheated to within 35°C of its indicated melting point of 1285°C. This was unexpected because of the ease with which the Al_2O_3-ZnO and TiO_2-ZnO eutectic mixtures had coupled previously.

The preceding tables indicated that there were four principle reasons why stable internal molten zones were not achieved in the materials tested. These are:

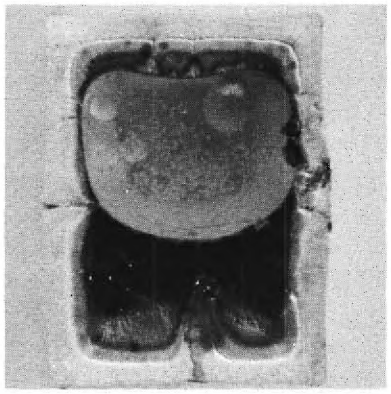

CeO_2

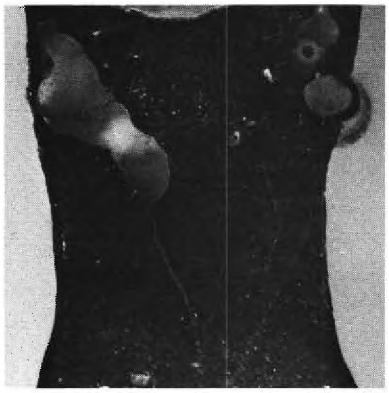

Cr_2O_3

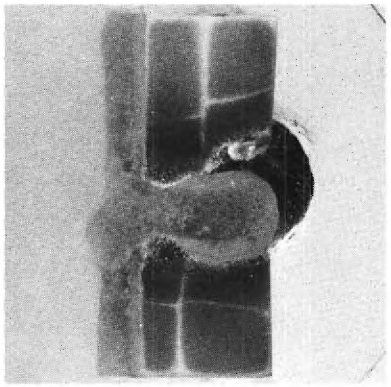

TiO_2

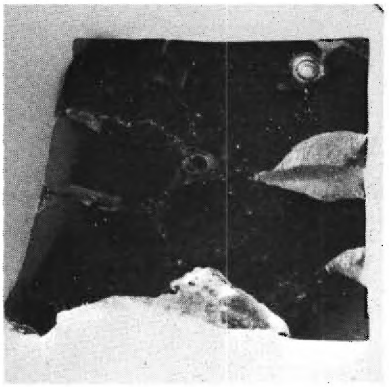

NiO

Figure 1. Polished Cross Sections of Oxide Samples That Were Internally Melted by Induction Heating. ~2X.

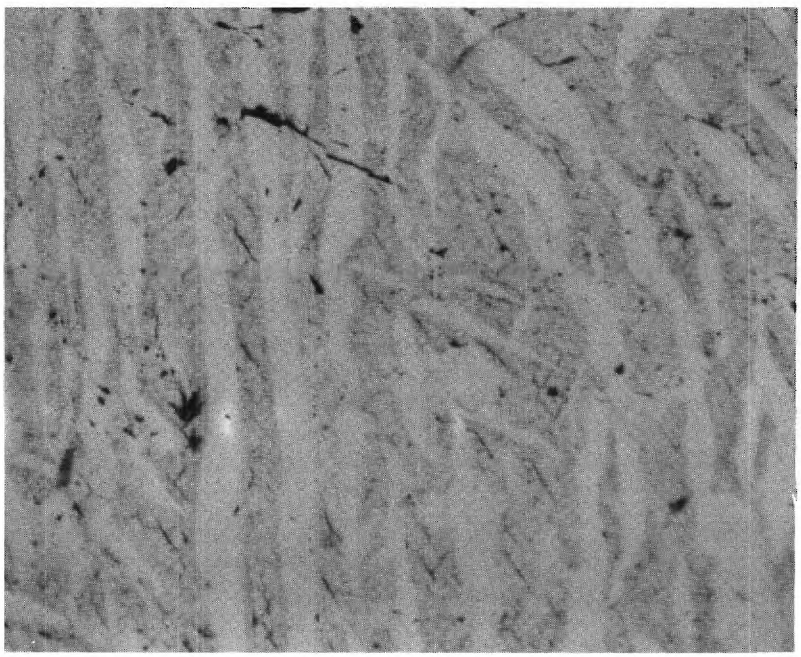

Figure 2. Photomicrograph of Melted Portion of CeO_2 Pellet Showing Two Phase Region. 200X.

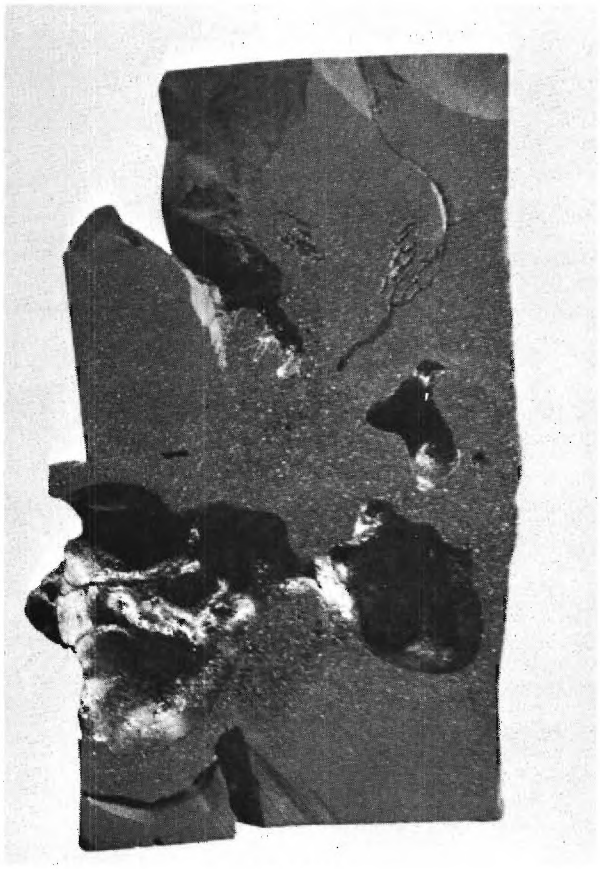

$Fe\ Ti\ O_5$

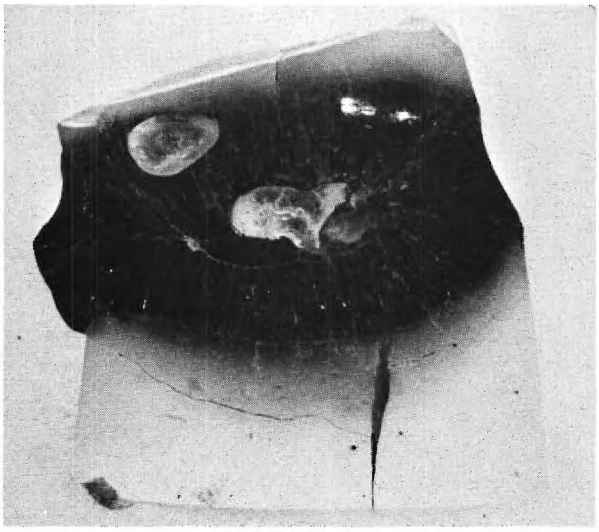

$Ni\ Ti\ O_3$

Figure 3. Polished Cross Sections of Binary Oxide Samples That Were Internally Melted by Induction Heating. ~2X.

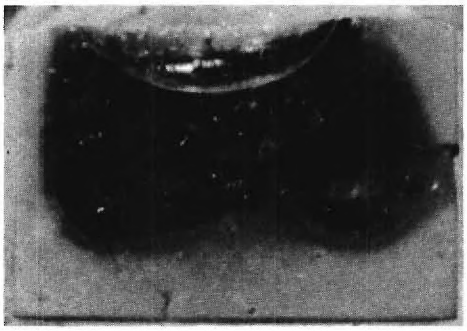

CaO Stabilized

Y_2O_3 Stabilized

Figure 4. Polished Cross Sections of Stabilized ZrO_2 Samples. ~2X.

(1) The efficiency of induction coupling was too low to provide the power necessary to achieve an internal molten zone.

(2) The surface of sample pellets did not emit enough thermal energy to remain solid and contain the molten zone.

(3) The specimens broke up due to thermal stresses.

(4) The starting materials were unstable because of sublimation or stoichiometry changes.

There are a number of approaches which may be used to improve the chances of successful induction melting oxide materials. Improved coupling efficiency can be obtained with higher rf frequencies, closer sample-coil geometries and increased rf power. Higher preheat temperatures, impurity doping and stoichiometry control can be utilized to increase the electrical conductivity of the oxides. Preliminary results indicate that in some cases hot pressing (see Al_2O_3 + 50% Cr_2O_3, Table III) and higher preheat temperatures (see $BaZrO_3$, Table II) are capable of increasing the electrical conductivity enough to allow coupling of oxide materials that originally could not be inductively heated. Although hot pressing improves the electrical conductivity, it has the adverse effect of making the samples more sensitive to thermal stress or shock failure during heating and cooling.

B. BEHAVIOR OF VARIOUS OXIDE-METAL SYSTEMS

The experiments designed to evaluate the compatability of metals other than tungsten as the metal component of the oxide-metal composites were restricted to the UO_2 and ZrO_2 systems. These tests were also utilized to determine which parameters control the ability of a system to produce a metal fiber-oxide matrix composite using unidirectional solidification techniques. A summary of the results obtained is listed below.

Pellets of UO_2 and stabilized ZrO_2 (8 mole percent Y_2O_3) containing 3.6 and 29 weight percent Mo respectively were internally melted in H_2-N_2 atmospheres containing about 30% hydrogen. The UO_2-Mo sample was preheated to 1420°C and easily coupled to a 4.8 mhz field. Power settings that produced surface temperatures between 2000°and 2200°C were used during the internal melting period. The ZrO_2-Mo specimen readily coupled to a 7.5 mhz field after being preheated to 1510°C. Skin temperatures around 1850°C were measured during this experiment. Both samples were lowered at the rate of about 4.3 cm/hr through the rf field.

Cross sections (Figure 5) revealed the presence of Mo spheres as large as 1/8 inch in diameter in both specimens. Higher magnification examination of these specimens after polishing revealed the following: the ZrO_2 specimen contained only two areas that were well melted; the UO_2 sample was extensively melted but only small areas in it contained very fine widely

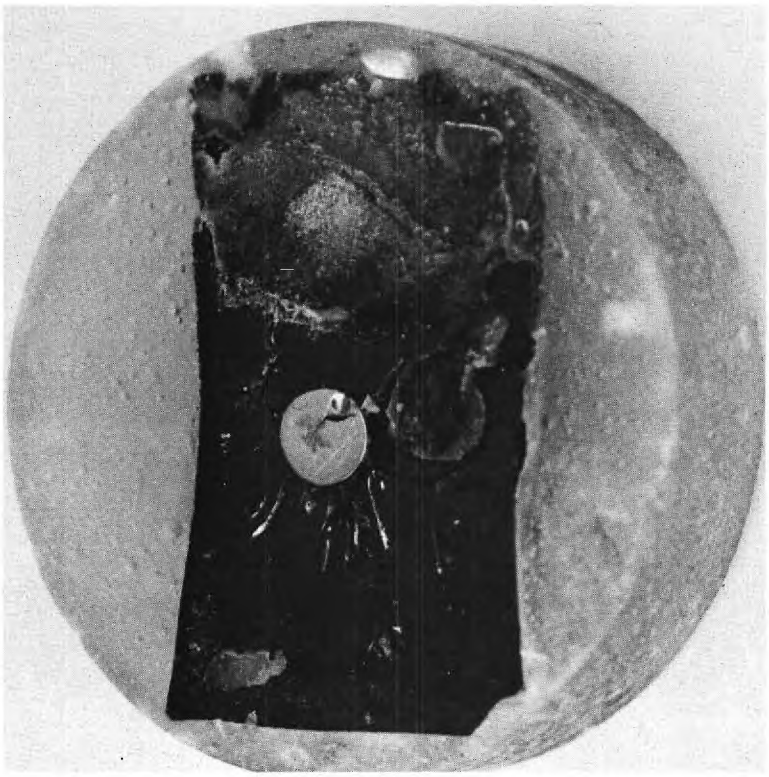

UO_2–Mo

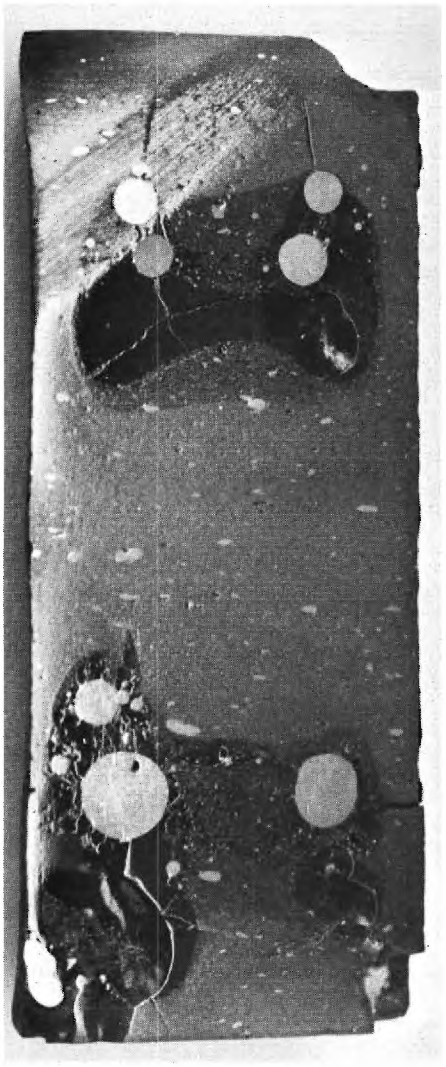

ZrO_2–Mo

Figure 5. Polished Cross Sections of UO_2-Mo and ZrO_2-Mo Samples Showing Large Mo Spheres. ~2X.

separated fibers of Mo (Figure 6). The ZrO_2 specimen contained many small Mo spheres (Figure 7) in its melted areas, whereas most of the Mo in the UO_2 specimen was observed as large spheres or fibers. From these results it appears that Mo is only very slightly soluble in molten UO_2 and nearly insoluble in molten ZrO_2.

Two other UO_2 pellets containing 2.94 and 2.91 weight percent of Ta and Nb respectively were also preheated to about 1420°C and inductively melted using a 4.8 mhz field in the H_2-N_2 atmosphere. Surface temperatures between 1800° and 2000°C were observed while the Ta pellet was lowered through the rf field at the rate of 3.3 cm/hr. Sections of this pellet revealed a porous structure with almost no metal observed. At high magnifications (Figure 8) a small area that appeared to have been molten was found to contain two nonmetallic phases and a few shiny streaks which might be metallic fibers. This may indicate that Ta is soluble in UO_2 or that a reaction between Ta and UO_2 occurred.

The surface temperatures observed for the UO_2 pellet containing Nb as it was lowered at a rate of 3.3 cm/hr were between 1600° and 1700°C. Sections of this pellet revealed a very porous structure and most likely indicates that the center of the sample did not melt. Again very little metal was observed, indicating the possibility of limited Nb solubility in UO_2.

From this data it appears that there are at least three parameters that have a major influence on the ability to achieve

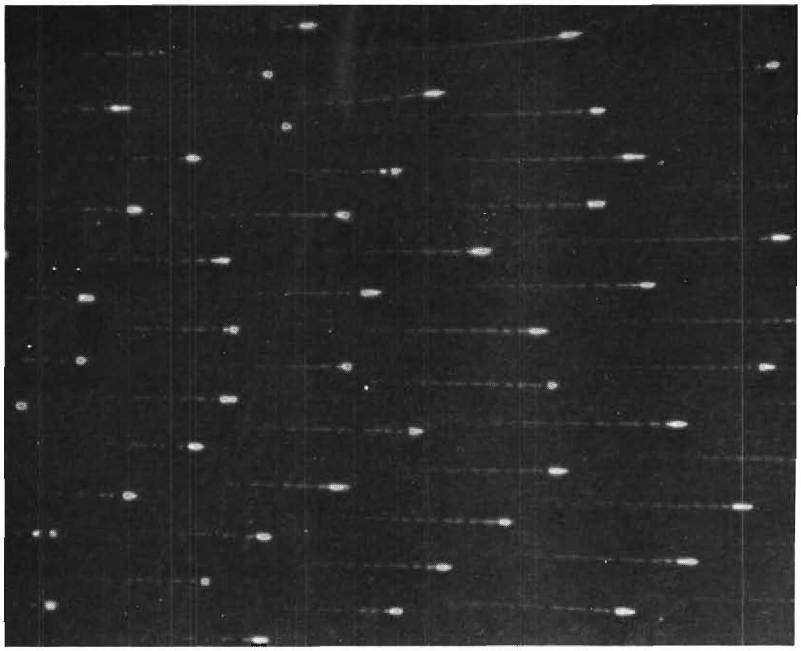

Figure 6. Photomicrograph of UO_2-Mo Sample Containing 3.6% Mo Showing Small Area Containing Mo Fibers. Dark Field, 600X.

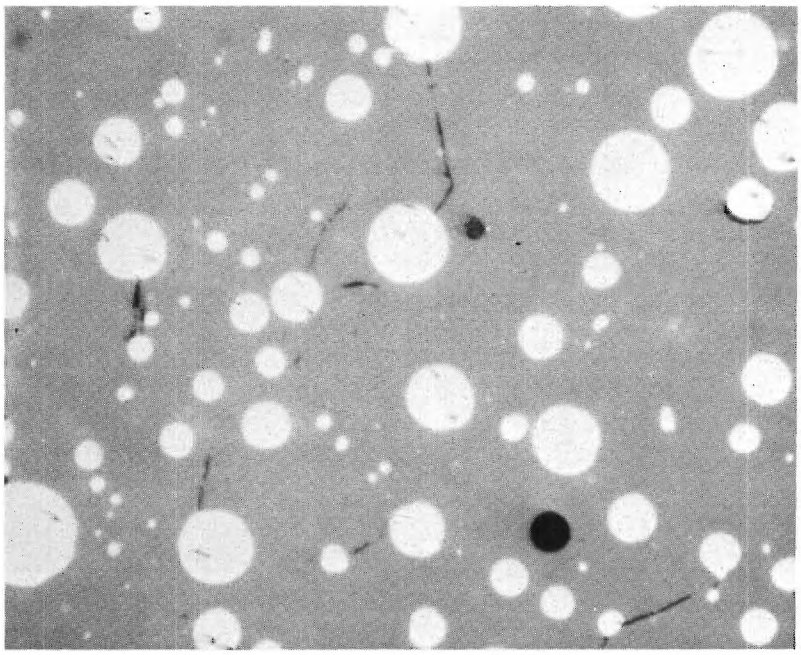

Figure 7. Photomicrograph of Stabilized ZrO_2-Mo Sample Containing 29% Mo Showing Small Spheres of Mo. 200X.

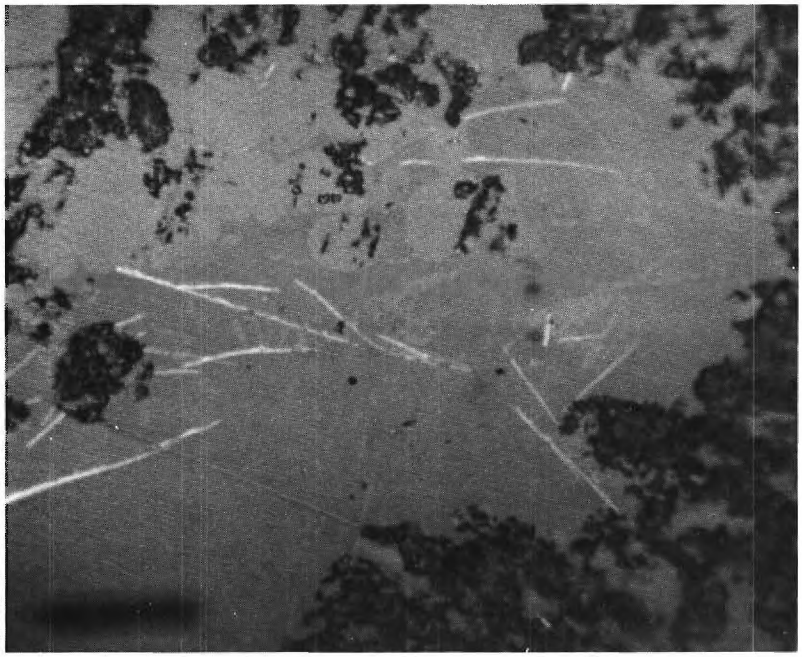

Figure 8. Photomicrograph of UO_2-Ta Sample Containing 2.94% Ta Showing Two Nonmetallic Phases and Shiny Streaks Which Might Be Metallic Fibers. 1000X.

coupled oxide-metal growth in various oxide-metal systems. These include surface energies of the oxide and metal, solubility of the metal in the oxide and any tendency of the metal and oxide to react with each other. Because of the extremely high temperatures required to melt these mixtures, the vapor pressure of the components, especially of the metal, may also play an important role in achieving a stable molten zone.

SECTION III

STRUCTURAL AND CHEMICAL CHARACTERIZATION OF OXIDE-METAL COMPOSITES

Scanning electron microscopy (SEM), non-dispersive x-ray analysis, high-voltage electron microscopy and various x-ray diffraction techniques were selected as suitable methods for the characterization of melt-grown oxide metal composites. A program was devised to ensure a comprehensive and efficient characterization of composite specimens using these techniques.

The characterization program included an evaluation of backscattered and secondary emission modes of operation in the SEM, an analysis of the microstructural information available from scanning electron micrographs and stereomicrographs, an SEM study of tungsten metal fiber growth and etch forms in selected UO_2 samples and the major orientational relationships between the tungsten fibers and uranium dioxide matrix were determined using various x-ray diffraction techniques.

In addition various pieces of equipment, notably a new oscilloscope camera for the SEM and a doubly bent graphite monochromator for the x-ray diffractometer, were installed. The new camera produces higher resolution micrographs and reduces the cost of SEM prints. The advantages of the monochromator include

a high incident x-ray beam intensity, a high signal-to-noise ratio and the ease of handling large or small samples with the same instrumental set-up without major instrument modifications.

A. COMPOSITE STRUCTURES

During the examination of the UO_2-W samples, two basically different types of oxide-metal structures have been observed. The first type is shown in Figure 9 and is characterized by the growth of W fibers essentially uniformly distributed across the melted zone. This growth pattern is interrupted by grain (cell or colony) boundaries where major changes in oxide and metal orientation occur. The second growth type is shown in Figure 10 and has circular areas of the oxide bounded by the composite (oxide-metal eutectic) structure. The large grain or cell structure shown in the previous figure is also present in this type of sample.

The shapes of the grains are highly irregular, and the diameters vary from a few microns to a few millimeters. In the structures containing the circular oxide areas, (Figure 10) the location of the grain (cell) boundaries appears to be random, although they generally pass through the two phase regions of the sample. Explanations for these types of structures are discussed in Section V, B of the Semi-Annual Technical Report[1].

Figure 11 also shows a UO_2-W sample displaying the latter geometry, as well as a portion of the unmelted skin of the sample. The general surface characteristics stand out very clearly and

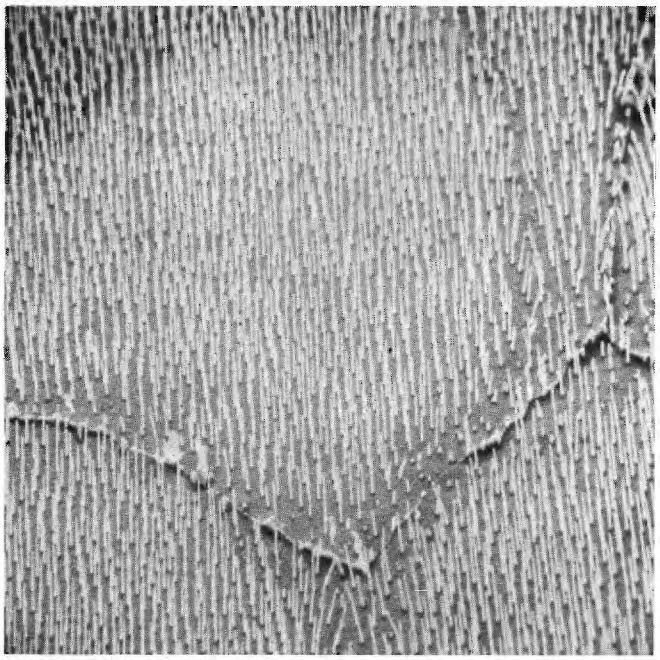

Figure 9. Scanning Electron Micrograph of UO_2-W Composite Displaying Uniform W Fiber Distribution, Emissive Mode of SEM. 630X.

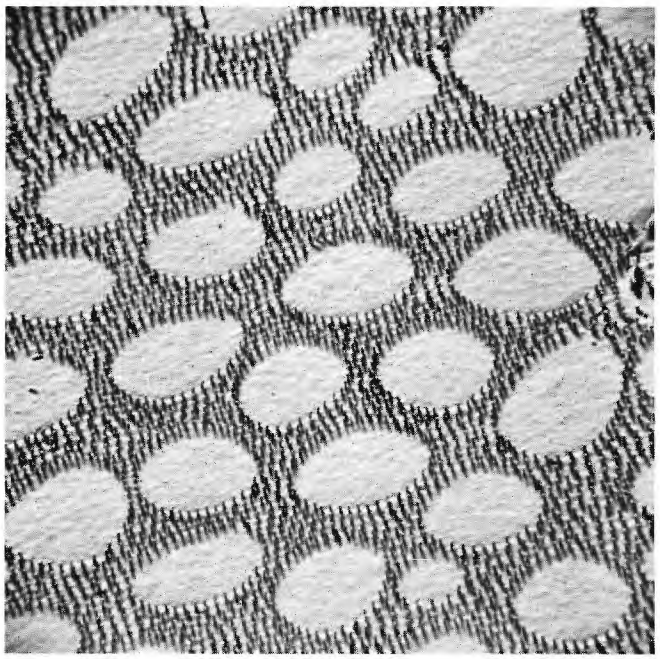

Figure 10. Scanning Electron Micrograph of UO_2-W Composite Displaying Circular Primary Phase Areas of UO_2 Plus Eutectic Growth, Reflective Mode of SEM. 500X.

Figure 11. Scanning Electron Micrograph of UO_2-W Composite Showing Contrast Obtained at Low Magnification When Backscattered Electron Mode Is Utilized. 20X.

illustrate the resolution that can be achieved at very low magnifications using the backscattered mode of the SEM. (It is not generally appreciated that under certain conditions the backscattered mode in the SEM gives more information than the usually utilized secondary emission mode.)

B. TUNGSTEN FIBER FORMS

The observed tungsten fiber shapes depend upon specimen orientation, composite growth conditions and the chemical etching technique used to remove a layer of the oxide to expose the fibers for SEM analysis. A variety of cross sections including round, hexagonal, square and rectangular have been observed. During etching, the fibers were occasionally altered in such a way that no characteristic crystallographic form was discernible. An example of this behavior is shown in Figure 12, where etching was used to intentionally alter the fiber shape to a geometry desirable for electron emitter applications.

Under ideal conditions growth forms develop which contain those crystallographic faces which have a minimum free surface energy. Crystal faces other than those expected can become dominant due to the presence of impurities (an example of which is octahedra crystals of NaCl, which normally has a cubic habit, grown from a water solution containing 10% urea), variations in the supply of solute and directional solidification. In the case

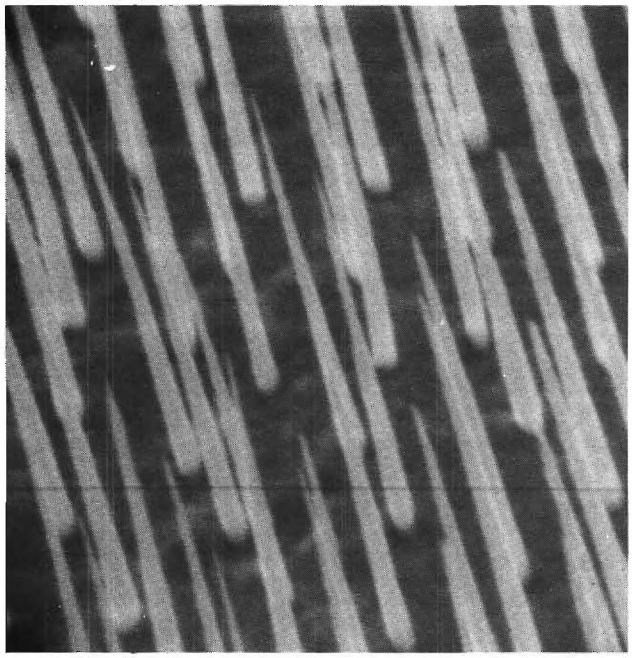

Figure 12. Scanning Electron Micrograph of Sharpened Tungsten Fiber Tips After Chemical Etching, Emissive Mode of SEM. 8500X.

of a body-centered cubic material (BCC) such as tungsten, the low energy (high atom density) faces are the (111), (110), (100) and (112).

Some of the crystallographic habits and fiber growth forms which are possible for tungsten are shown in Figures 13 - 22. The major difference between the octahedral (Figures 13 - 15), cubic (Figures 16 and 17) and rhombohedral (Figures 18 - 22) growth forms is the dominance of (111), (100) and (110) faces respectively.

Several of these fiber geometries have been observed either as growth habits or etch forms in UO_2-W composites. The octahedral form shown in Figures 14 and 15 is considered a possible explanation for the apparently round growth and etch forms often observed after etching the UO_2-W composite. For example, Figure 23 shows W fibers where multi-faceted faces on the fiber shaft may exist but are not well enough defined to be resolved in the SEM and the fibers appear circular. The tungsten fibers shown in Figure 24 appear to be square shaped with crystal faces on the tips which match the angular relationship of the cubic tip facets in Figure 16. This is most likely the combined result of a cubic growth form with the (111) facets being produced during the etching process employed to remove the UO_2 matrix and expose the fibers. This is surprising since growth forms[6] derived from the cubeoctahedron are normally found only for face-centered-cubic (FCC) metals.

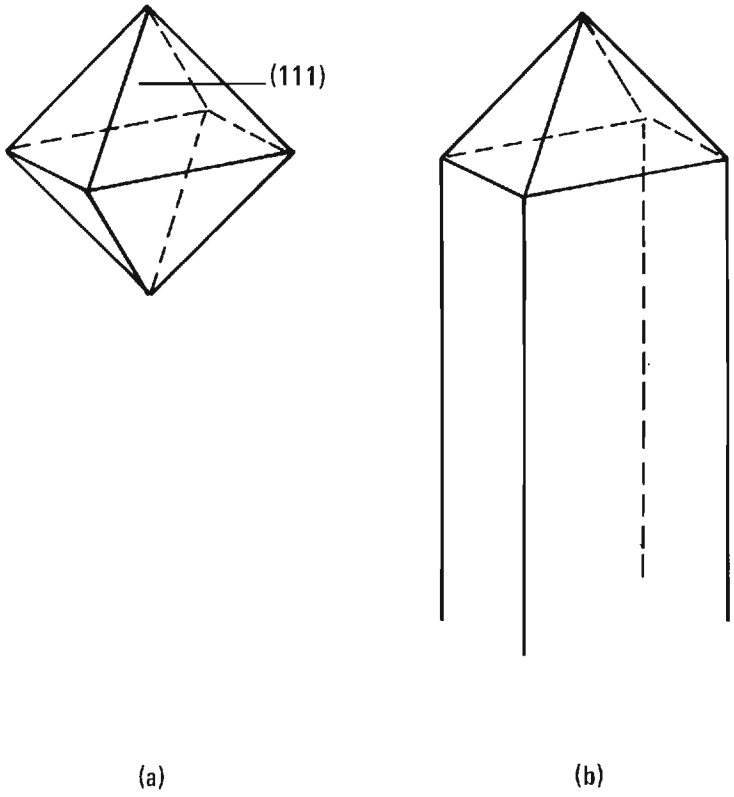

Figure 13. Octahedral Growth Forms; (a) Equilibrium Form, (b) Distortion Due to Fiber Formation.

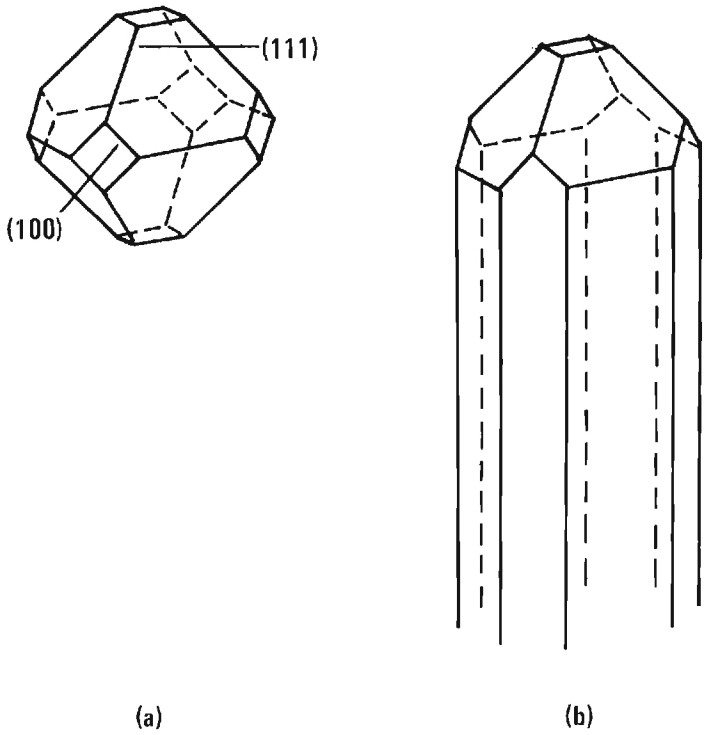

Figure 14. Octahedral Growth Forms, Cubeoctahedron; (a) Equilibrium Form, (b) Distortion Due to Fiber Formation.

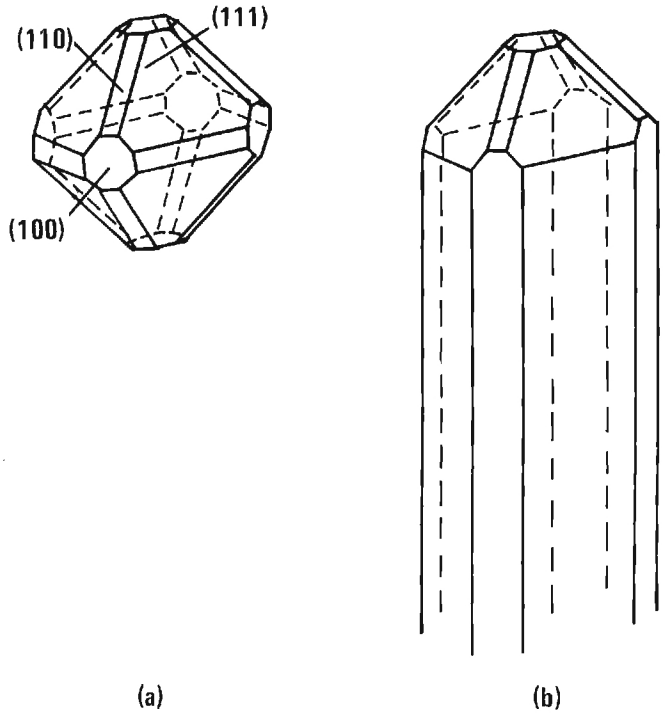

Figure 15. Octahedral Growth Forms Consisting of {100}, {111} and {110} Faces; (a) Equilibrium Form, (b) Distortion Due to Fiber Formation.

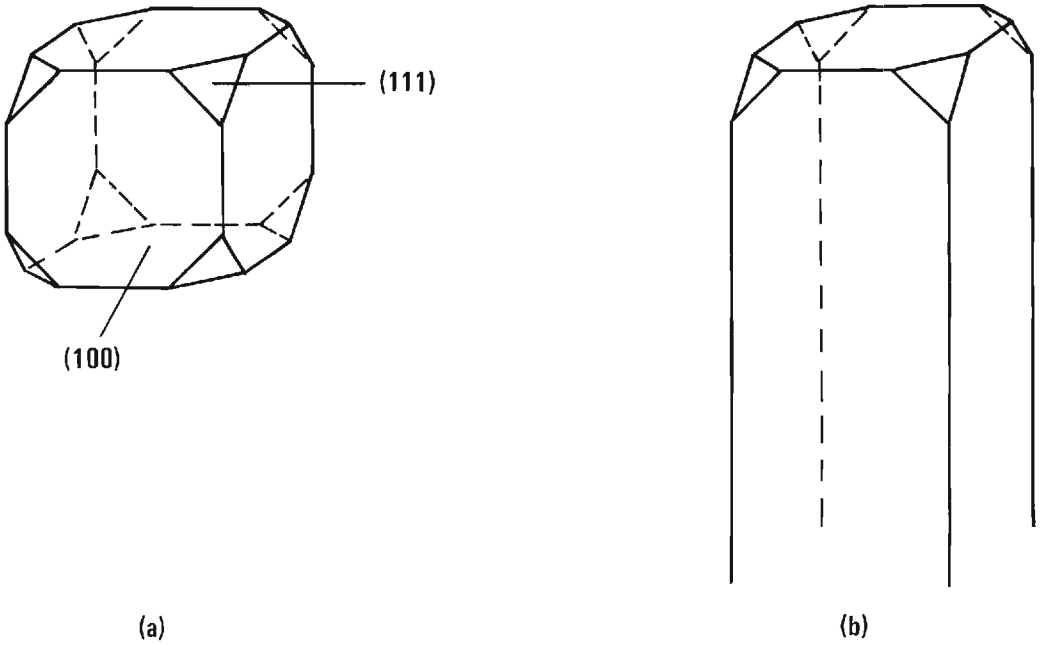

Figure 16. Cubic Growth Forms of Cubeoctahedron; (a) Equilibrium Form, (b) Possible Fiber Growth Form.

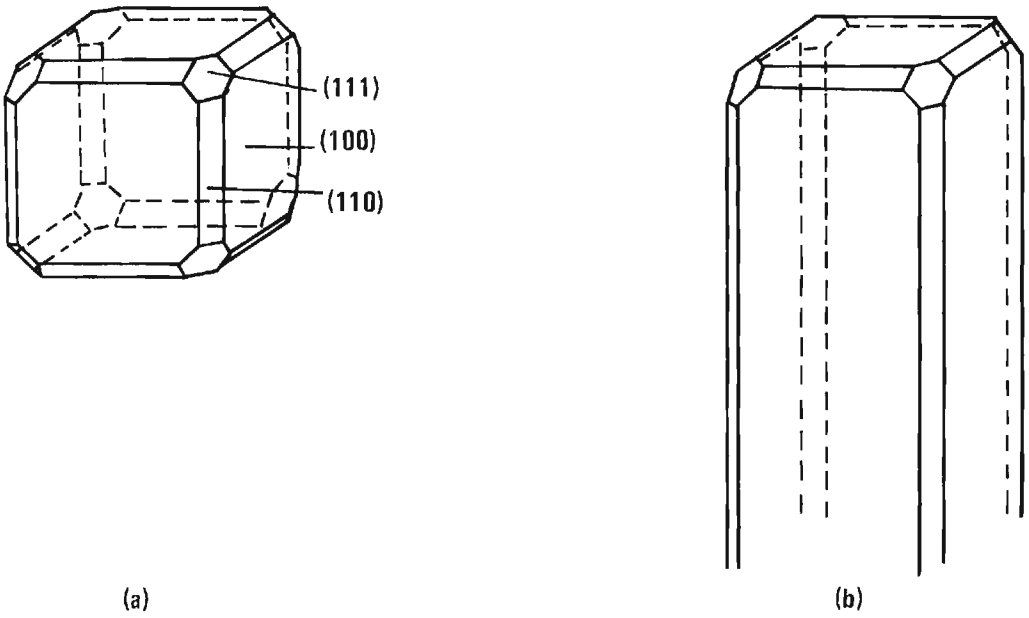

Figure 17. Cubic Growth Forms of Cubeoctahedron; Consisting of {100}, {111} and {110} Faces; (a) Equilibrium Form, (b) Possible Fiber Growth Forms.

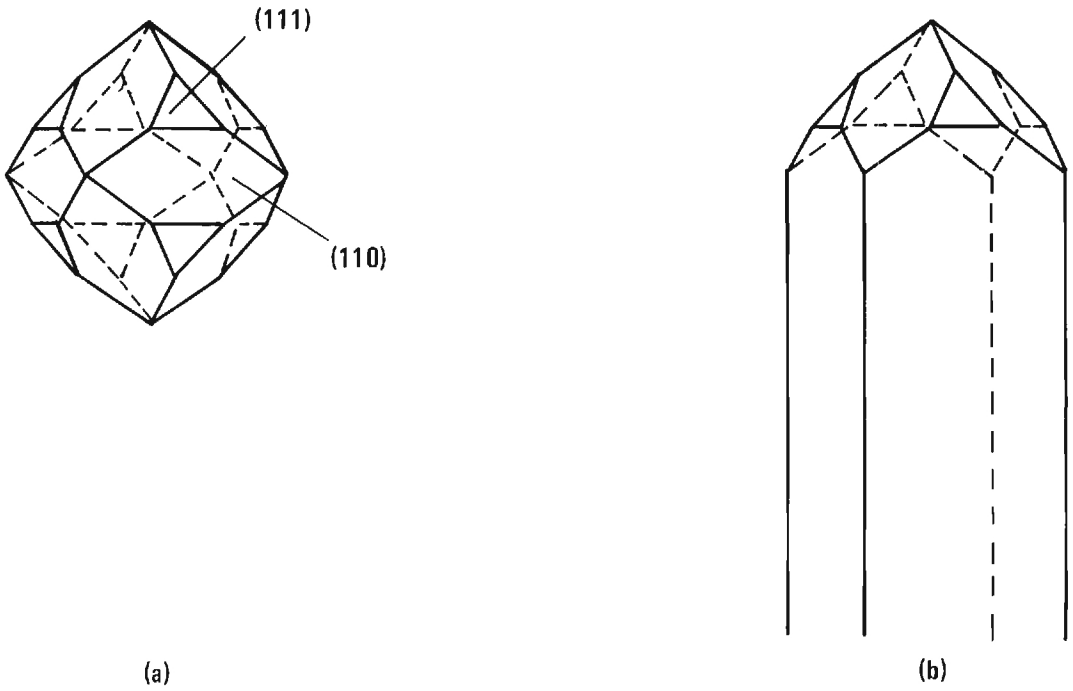

Figure 18. Rhombohedral Growth Forms of Cube-octahedron; (a) Equilibrium Form, (b) Possible Fiber Growth Form.

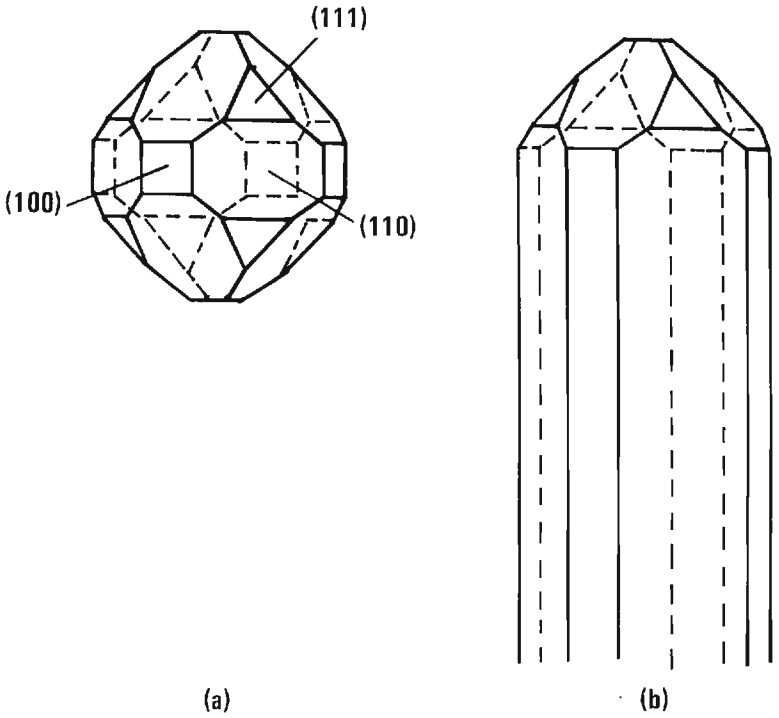

Figure 19. Rhombohedral Growth Forms of Cube-octahedron Consisting of {100}, {111} and {110} Faces; (a) Equilibrium Form, (b) Possible Fiber Form.

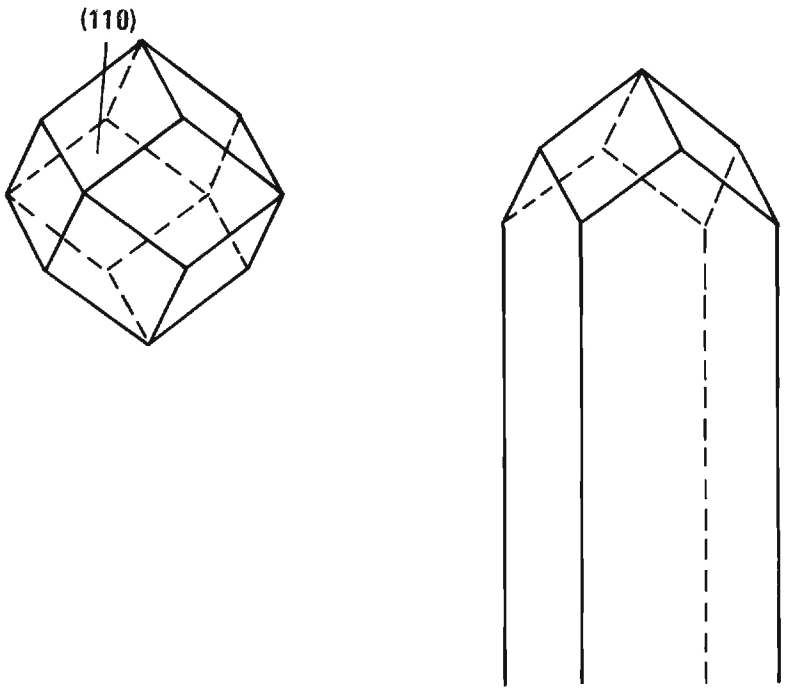

Figure 20. Rhombododecahedron Growth Forms; (a) Equilibrium Form, (b) Possible Fiber Growth Form.

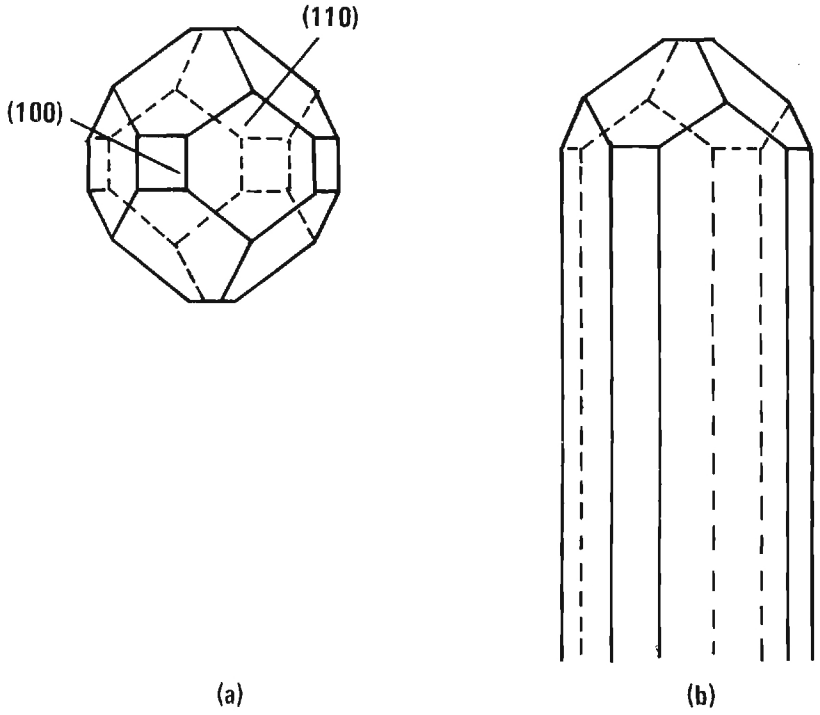

Figure 21. Rhombododecahedron Growth Form With {100} Facets; (a) Equilibrium Form, (b) Possible Fiber Growth Forms.

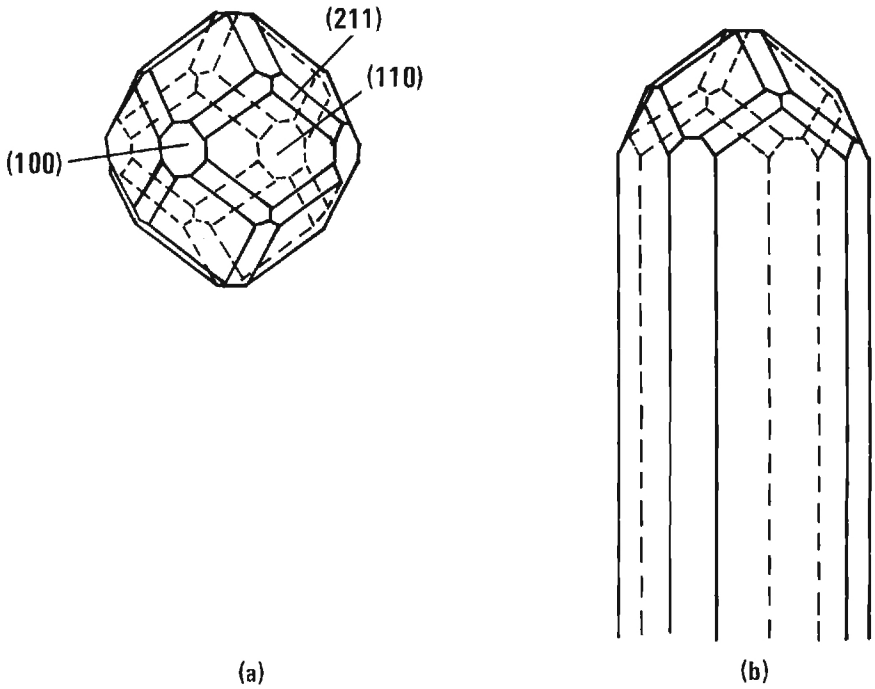

Figure 22. Rhombododecahedron Growth Form With {100} and {211} Facets; (a) Equilibrium Form, (b) Possible Fiber Form.

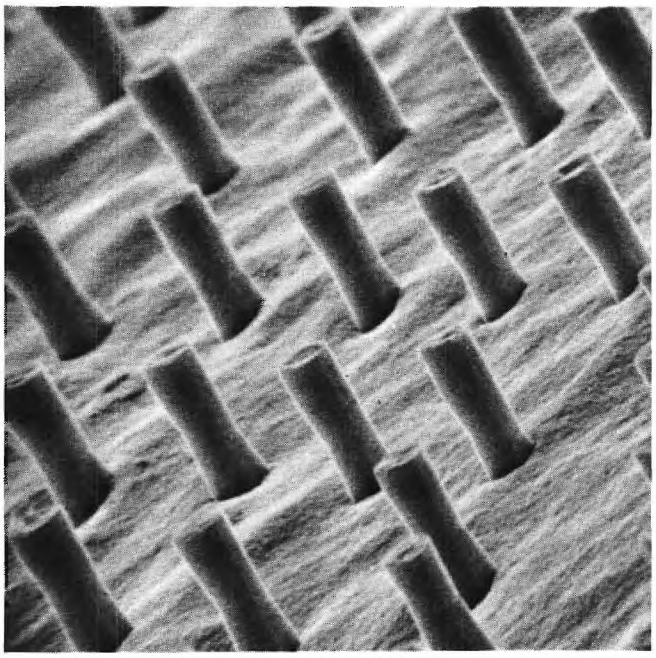

Figure 23. Scanning Electron Micrograph of UO_2-W Composite Displaying Apparently Circular W Fibers With Some Indication of Faceting on the Fiber Shafts. 6200X.

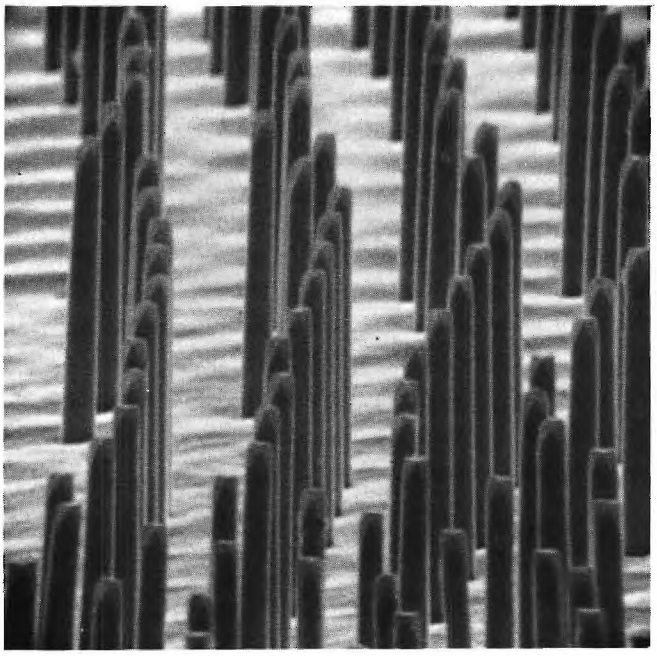

Figure 24. Scanning Electron Micrograph of UO_2-W Composite Showing Tungsten Fibers With Facets on Tips. 5000X.

The equilibrium growth form[6] of a BCC metal is the rhombododecahedron (see Figure 20a). When this crystal habit, which is composed only of {110} planes, is cut into two equal halves parallel to any of the opposing pairs of {110} planes, a hexagonal cross section is obtained with four equal length edges. The remaining two opposite edges may be longer or shorter than the four equal edges (depending on the particular growth form which has developed). Figure 25 is a transmission electron micrograph* of a UO_2-W composite showing the cross section of several W fibers that comply with the preceeding analysis. When this crystal form (Figure 20a) is rotated through 45° about the potential fiber axis (Figure 26a) and then developed into a fiber form (Figure 26b), the hexagonal fiber cross section can easily be visualized.

Rhombododecahedron growth forms of the types shown in Figures 19, 21 and 22 would produce fibers with octagonal cross sections. Figure 27 is an SEM micrograph of a tungsten fiber whose base clearly displays an octagonal shape. During etching the fiber morphology was changed by the different etching rates in different crystallographic directions to produce an almost square section at the fiber tip.

Equilibrium growth forms which have been observed in a number of metals can be utilized to interpret growth forms of tungsten fibers in UO_2. Cubic growth forms which have been derived

*This micrograph was taken by C. S. Yust of the Metals and Ceramics Division, Oak Ridge National Laboratory, Oak Ridge, Tennessee.

Figure 25. Transmission Electron Micrograph of UO_2-W Composite Showing Hexagonal Cross Section of Several W Fibers. About 25,000X.

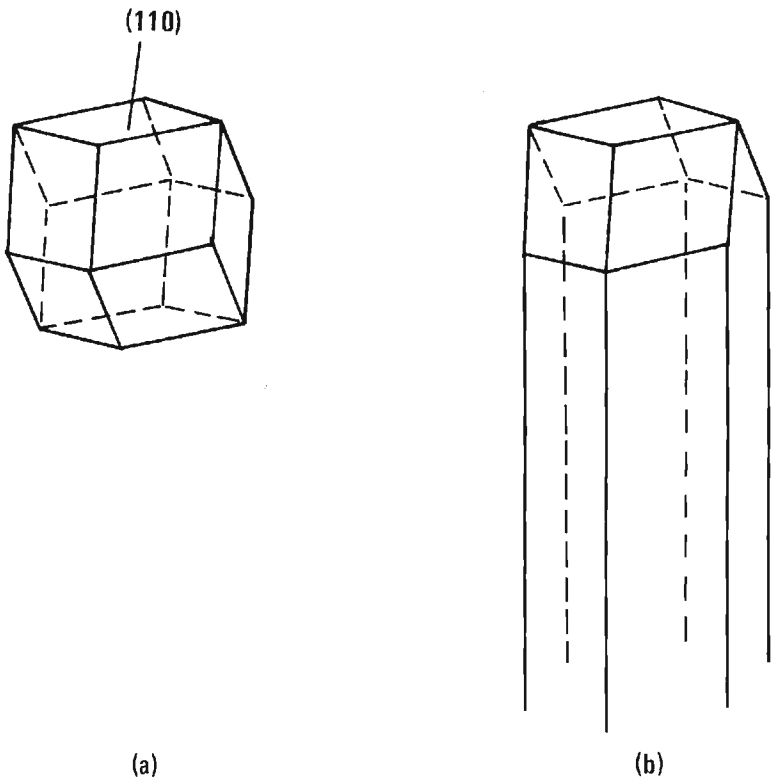

Figure 26. Rhombododecahedron Rotated About Axis (See Figure 20); (a) Equilibrium Form, (b) Fiber Growth Form.

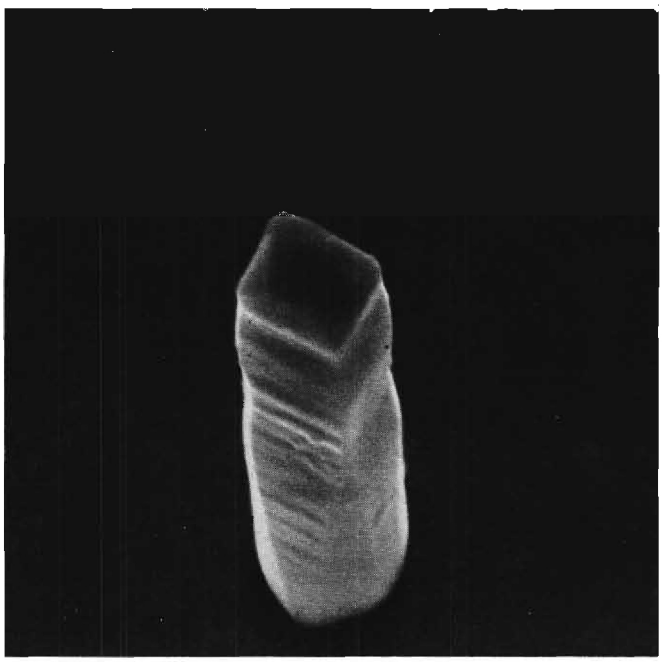

Figure 27. Scanning Electron Micrograph (Emissive Mode) of a Tungsten Fiber With Hexagonal Cross Section After Etching. 21,800X.

from the rhombododecahedron appear to be good models for observed tungsten fibers.

C. HIGH VOLTAGE ELECTRON MICROSCOPY (HVEM)

A UO_2-W sample was ion-etched for 154 hours to thin the material for examination in the HVEM.* The tungsten fiber was viewed at approximately 45° off the fiber axis (Figure 28). The fibers were surrounded, as was anticipated, by a pile-up of dislocations. In some cases these dislocations seemed to originate in the fiber and then continue into the oxide matrix. It is noteworthy that no cracks are visible at the fiber-matrix interface, suggesting excellent bonding.

D. UO_2-W ORIENTATION RELATIONSHIPS

Mutual oxide-metal orientation relationships were determined using four separate UO_2-W samples. A single crystal orienter (goniostat) possessing several mutually perpendicular and movable rotation axes and conventional x-ray diffraction techniques were used in this work. The oxide-metal samples possessed both the uniform W pin geometry and the circular primary phase areas of UO_2 surrounded by the uniform (eutectic) structure shown in Figures 9 and 10. In both of these structures small cell or grain boundaries (a few hundred microns to a few millimeters in size) were present;

*This work was done at the 1 Mev HVEM facility at U. S. Steel Corporation in Monroeville, Pa. The authors wish to acknowledge the generous help given them by Dr. R. M. Fisher and his staff.

Figure 28. High Voltage Transmission Electron Micrograph of Tungsten Fiber in UO_2 Matrix After Sample Thinning by Ion Etching. Fiber Is Viewed at Approximately 45° Off Fiber Axis. 50,000X.

across these boundaries major changes in orientation existed. Consequently during x-ray analysis, diffraction occurred from several differently oriented regions. The UO_2-W sample was manually adjusted so that the major crystallographic orientation could be obtained from the overall sample as well as in small (2mm by 2mm) areas. Tables IV through VII present this information.

All of the UO_2-W samples were transverse sections cut approximately perpendicular to the growth direction. Thus the planes of UO_2 and W shown as being parallel in the second column of the Tables IV through VII are also the dominant growth directions of the oxide matrix and metal fibers. Sketches depicting these dominant relationships are included with each table.

Examination of the orientation data readily shows that the most often occurring growth direction of the oxide matrix is $[\bar{1}11]$, whereas the tungsten growth direction was divided between $[\bar{1}10]$ and $[\bar{1}00]$. Future work is planned utilizing the electron diffraction capability of the SEM for correlating fiber growth forms with crystallographic orientation within an individual cell or grain.

TABLE IV

MUTUAL ORIENTATION RELATIONS EXISTING IN UO_2-W SAMPLE 6-42 CONTAINING UNIFORM W FIBER GROWTH

Area Examined	Planes Parallel	Directions Parallel
1 - Overall	$(100)_W$ // $(111)_{UO_2}$	$[1\bar{1}0]_W$ // $[1\bar{1}0]_{UO_2}$
2 - "	$(110)_W$ // $(111)_{UO_2}$	$[001]_W$ // $[1\bar{1}\bar{2}]_{UO_2}$
3 - 2x2 mm^2	$(110)_W$ // $(111)_{UO_2}$	$[00\bar{1}]_W$ // $[11\bar{2}]_{UO_2}$
4 - "	$(110)_W$ // $(111)_{UO_2}$	$[001]_W$ // $[11\bar{2}]_{UO_2}$
5 - "	$(100)_W$ // $(111)_{UO_2}$	$[1\bar{1}0]_W$ // $[1\bar{1}0]_{UO_2}$
6 - "	$(100)_W$ // $(111)_{UO_2}$	$[1\bar{1}0]_W$ // $[1\bar{1}0]_{UO_2}$

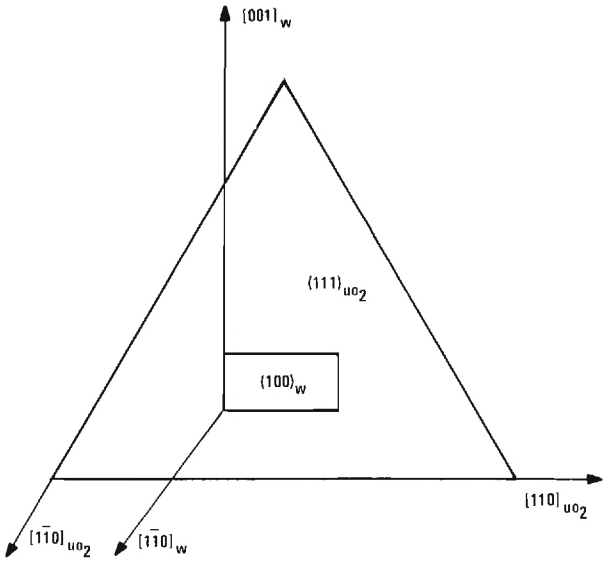

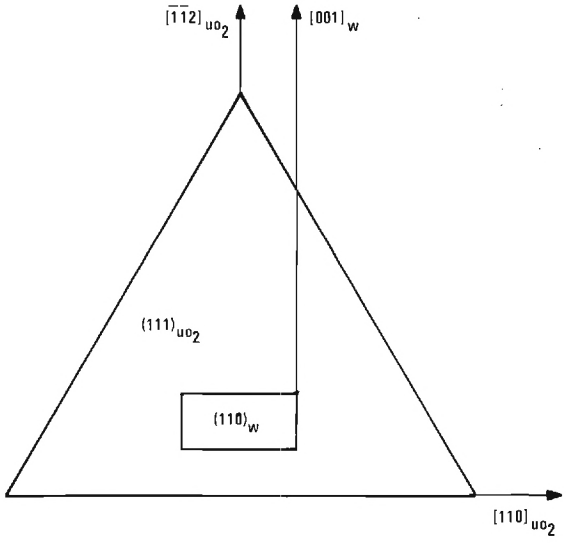

TABLE V

MUTUAL ORIENTATION RELATIONSHIPS IN UO_2-W SAMPLE 117 CONTAINING THE UNIFORM W FIBER GEOMETRY

Area Examined	Planes Parallel	Directions Parallel
1 - Overall	$(110)_W$ // $(111)_{UO_2}$	$[00\bar{1}]_W$ // $[11\bar{2}]_{UO_2}$
2 - 2x2 mm^2	$(110)_W$ // $(111)_{UO_2}$	$[00\bar{1}]_W$ // $[11\bar{2}]_{UO_2}$
3 - "	$(110)_W$ // $(100)_{UO_2}$	$[001]_W$ // $[\bar{1}\bar{1}0]_{UO_2}$
4 - "	$(110)_W$ // $(111)_{UO_2}$	$[1\bar{1}0]_W$ // $[1\bar{1}0]_{UO_2}$
5 - "	$(110)_W$ // $(100)_{UO_2}$	$[11\bar{2}]_W$ // $[110]_{UO_2}$

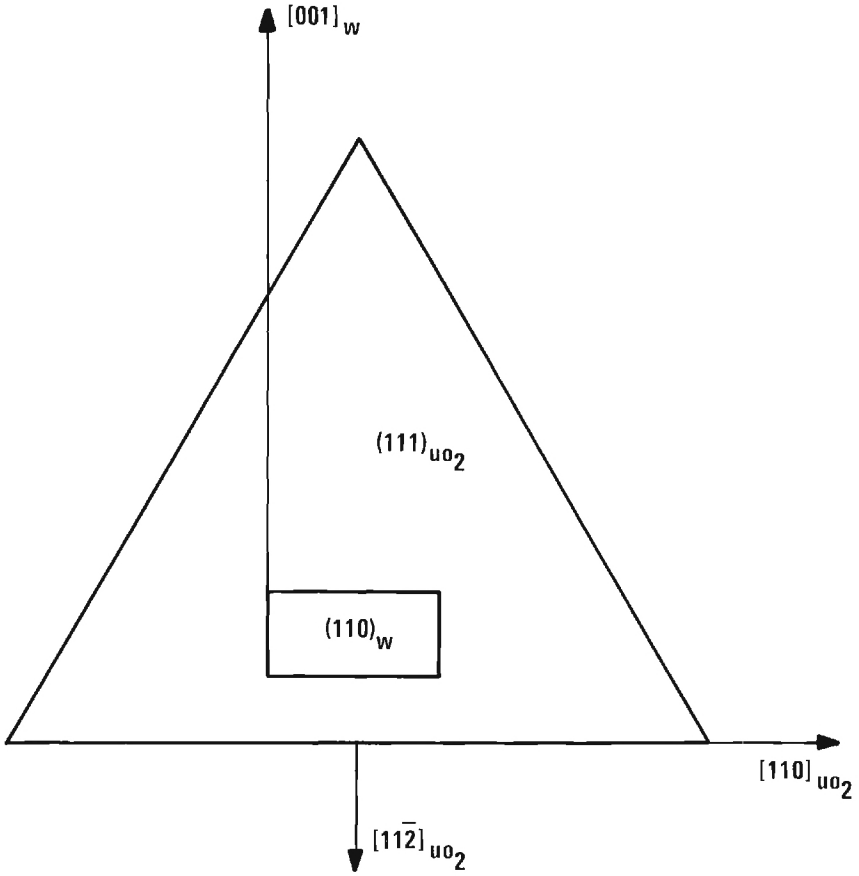

TABLE VI

MUTUAL ORIENTATION RELATIONSHIPS IN UO_2-W SAMPLE 136 CONTAINING THE CIRCULAR AREAS OF PRIMARY UO_2

Area Examined	Planes Parallel	Directions Parallel
1 - Overall	$(110)_W$ // $(111)_{UO_2}$	$[001]_W$ // $[\bar{1}10]_{UO_2}$
2 - 2x2 mm^2	$(100)_W$ // $(111)_{UO_2}$	$[001]_W$ // $[110]_{UO_2}$
3 - "	$(110)_W$ // $(111)_{UO_2}$	$[001]_W$ // $[\bar{1}\bar{1}2]_{UO_2}$
4 - "	$(110)_W$ // $(111)_{UO_2}$	$[00\bar{1}]_W$ // $[\bar{1}\bar{1}0]_{UO_2}$
5 - "	$(001)_W$ // $(111)_{UO_2}$	$[100]_W$ // $[11\bar{2}]_{UO_2}$
6 - "	$(110)_W$ // $(111)_{UO_2}$	$[00\bar{1}]_W$ // $[11\bar{2}]_{UO_2}$

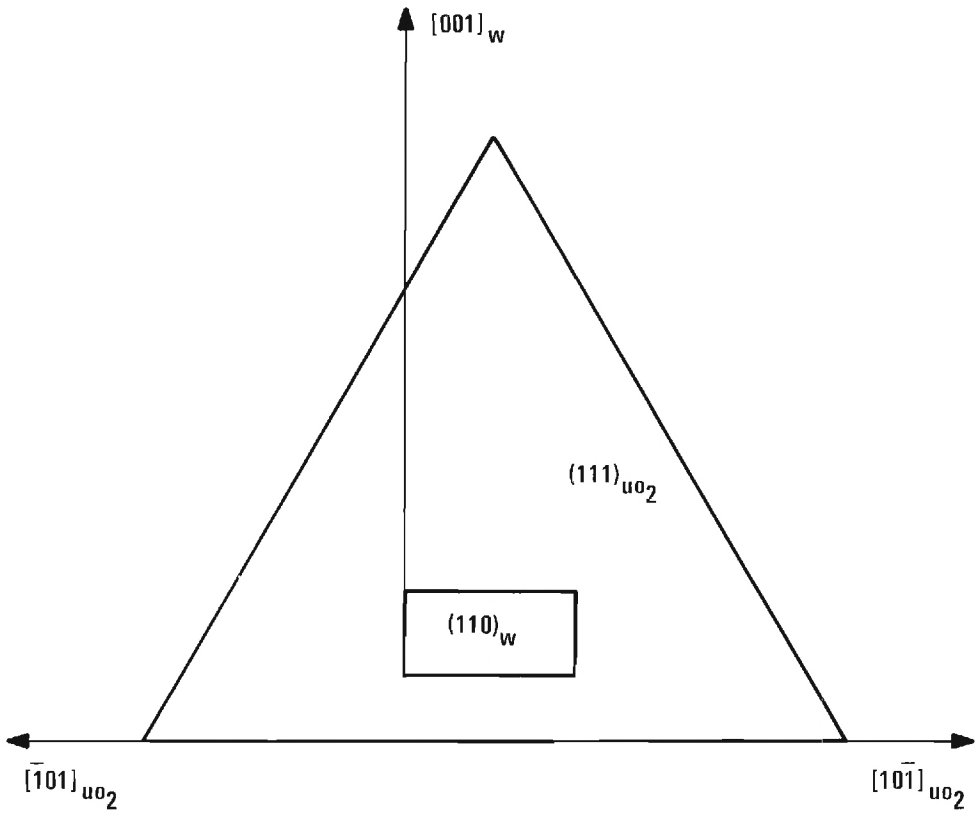

TABLE VII

MUTUAL ORIENTATION RELATIONSHIPS IN UO_2-W SAMPLE 199 CONTAINING THE CIRCULAR AREAS OF PRIMARY UO_2

Area Examined	Planes Parallel	Directions Parallel
1 - Overall	$(100)_W$ // $(111)_{UO_2}$	$[1\bar{1}0]_W$ // $[1\bar{1}0]_{UO_2}$
2 - "	$(110)_W$ // $(111)_{UO_2}$	$[00\bar{1}]_W$ // $[11\bar{2}]_{UO_2}$
3 - 2x2 mm^2	$(110)_W$ // $(100)_{UO_2}$	$[001]_W$ // $[\bar{1}\bar{1}0]_{UO_2}$
4 - "	$(110)_W$ // $(111)_{UO_2}$	$[00\bar{1}]_W$ // $[11\bar{2}]_{UO_2}$
5 - "	$(110)_W$ // $(111)_{UO_2}$	$[00\bar{1}]_W$ // $[11\bar{2}]_{UO_2}$
6 - "	$(110)_W$ // $(111)_{UO_2}$	$[1\bar{1}2]_W$ // $[\bar{1}\bar{1}2]_{UO_2}$

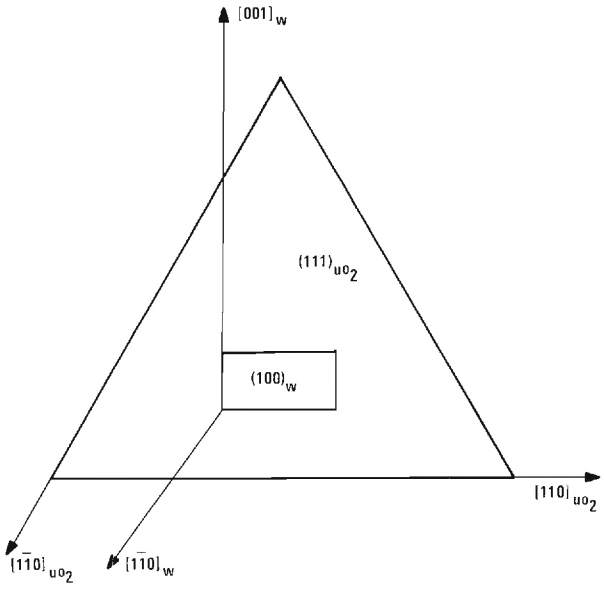

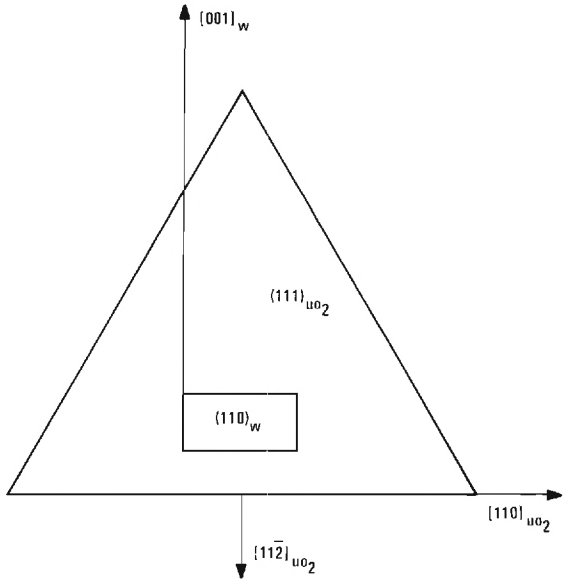

SECTION IV

COMPOSITE GROWTH IN OXIDE-METAL SYSTEMS AND THE FORMATION OF OPTIMUM EMITTING ARRAYS

The major objective of this portion of the project is to study growth in a model oxide-metal system, i.e. UO_2-W, and to establish the role controllable growth parameters exert on the composite microstructures. Emphasis will be placed on those variables which produce oxide-metal structures that have potential application as electronic devices. Geometries that will yield optimum electron field emission performance are of principle concern at present. The facility used to grow the oxide-metal composites is described.

Oxide-metal microstructures observed in the UO_2-W system were previously analyzed[1] on the basis of oxide-metal ratios, a proposed phase diagram and variable growth rates to gain understanding about the growth processes in oxide-metal systems. A brief review of this analysis is included in this Report. Additional information on solidifying non-eutectic oxide-metal mixtures with and without mechanical mixing of the liquid is also presented. The initial systematic experiments designed to determine the relationship between fiber density and diameter versus growth conditions in the system UO_2-W have been performed.

The development of composite growth in the stabilized ZrO_2-W system has progressed rapidly, and the structures developed in this system are shown. Based on the results obtained from the UO_2-W and ZrO_2-W systems, the parameters influencing and controlling successful composite growth are outlined. Lastly, the chemical etching work designed both to expose and shape the W fibers for enhanced emission is described.

A. COMPOSITE GROWTH EQUIPMENT

In a previous report[1] the facility used for composite growth was described. Only recent equipment modifications and new equipment are discussed here. Presently two rf generators are operative: the new Lepel dual frequency (2-8 mhz and 15-35 mhz) 10 KW generator and an older Westinghouse 10 KW unit modified to operate at approximately 4.0 mhz. Figure 29 shows the dual frequency generator, table with vertical movement and associated controls used for the oxide and oxide-metal growth experiments.

Figure 30 is a schematic diagram of the growth system employed to melt the oxide-metal samples. In the last report[1] the top molybdenum heater was not shown, as various designs for its support were being considered. The simple one-hole rubber stopper shown in Figure 30 proved to be the simplest trouble-free solution. A second growth station is also operative, very similar to that shown in Figure 30 except that a very flexible metal

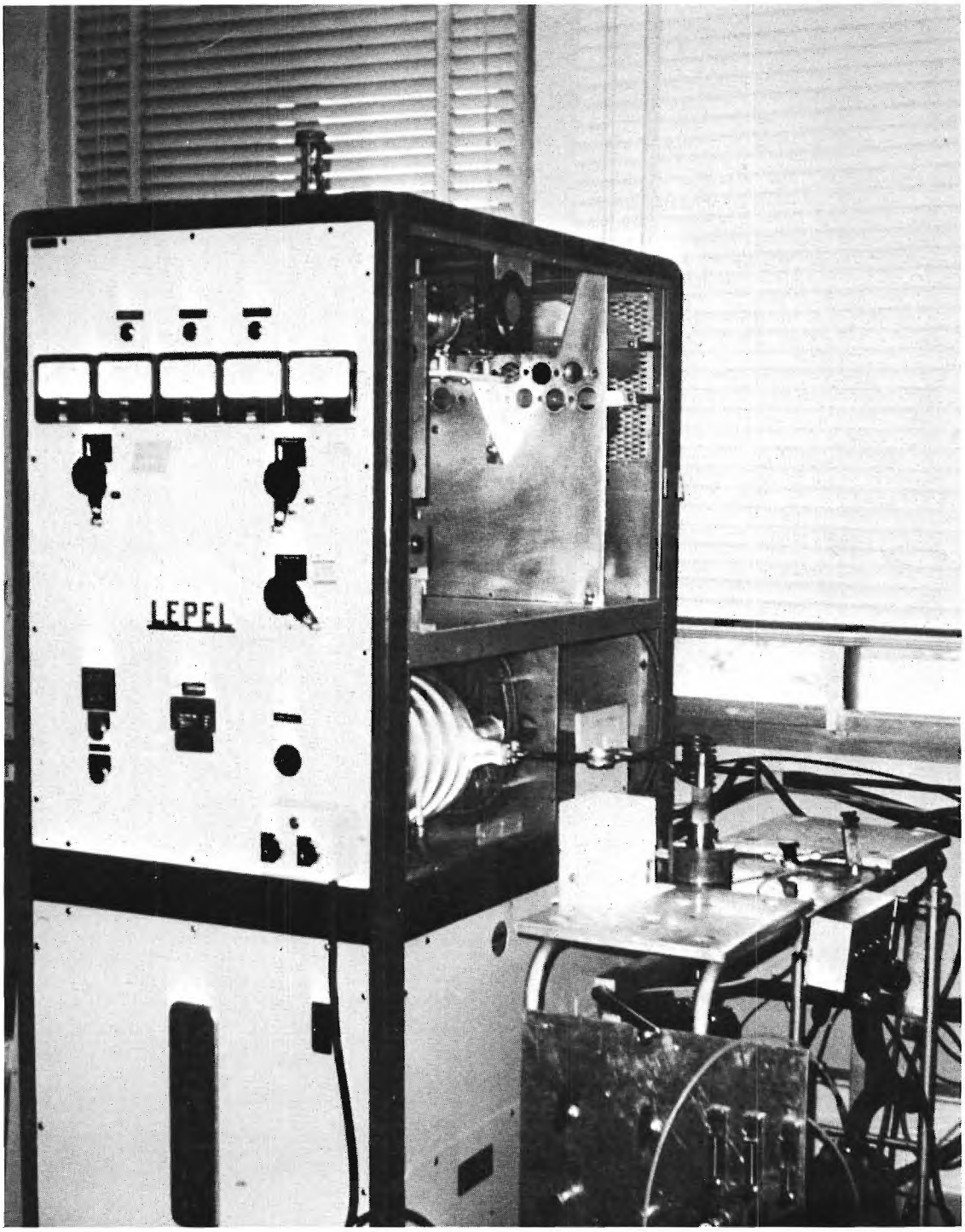

Figure 29. Overall View of the Dual Frequency rf Generator and Composite Growth Equipment.

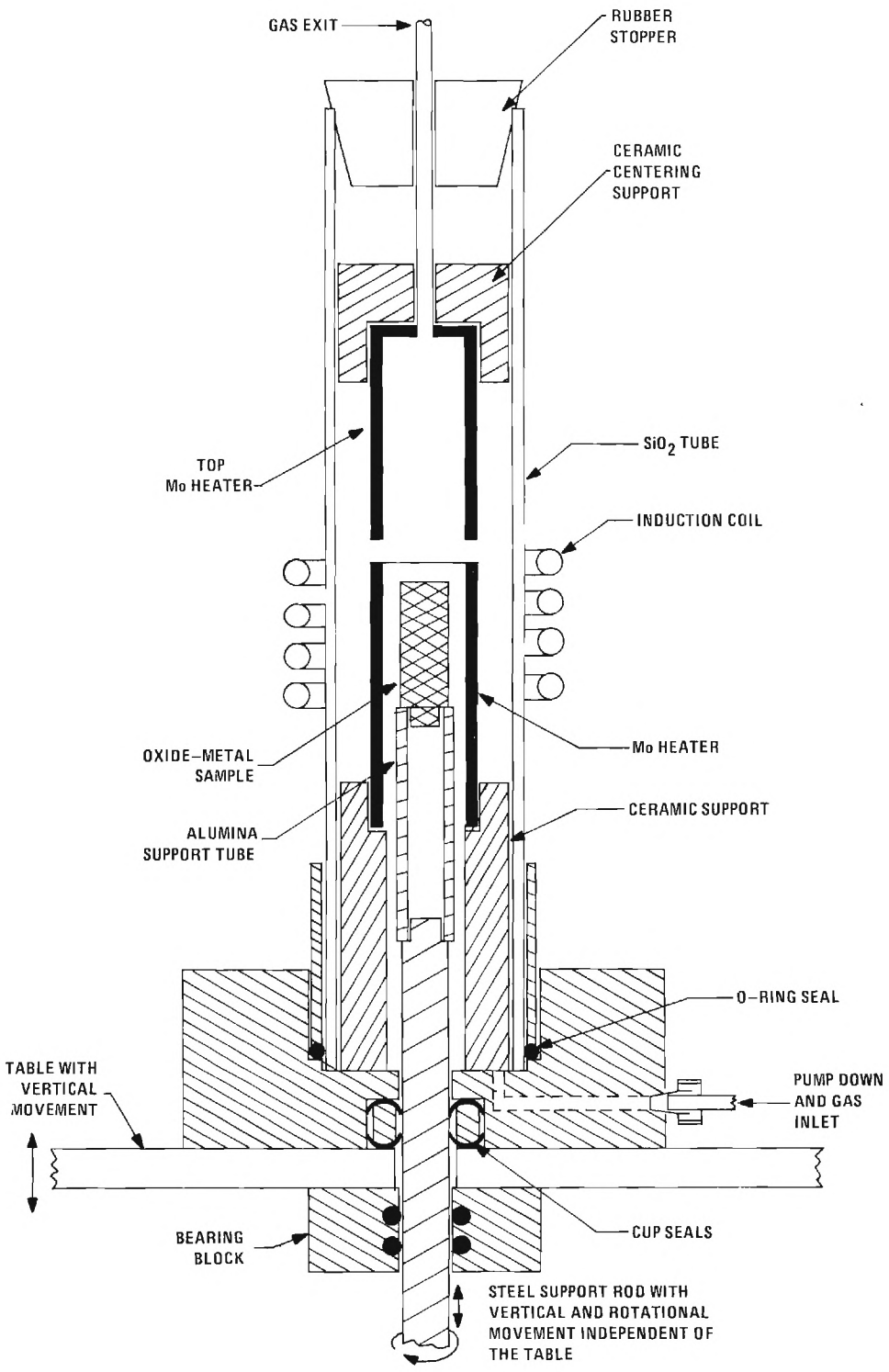

Figure 30. Schematic Diagram of the Facility for the Growth of Oxide-Metal Composites.

bellows is used to provide the seal between the support rod and growth chamber, instead of the cup seals shown in the schematic diagram.

Several attempts have been made to substitute pyrex tubes for the more expensive and variable size fused silica tubes currently used in the growth system. However, the extremely high temperatures and rf frequencies required for composite growth caused excessive arcing when pyrex tubes were used.

B. ANALYSIS OF OXIDE-METAL SOLIDIFICATION

In the previous report[1] the factors controlling oxide-metal composite growth in the system UO_2-W were interpreted using the oxide-metal ratios, growth rates, degree of undercooling and a tentative phase diagram. Two basically different types of structures were observed: composites consisting of a uniform distribution of W fibers (see Figure 9, Section III) when solidifying near eutectic compositions and structures consisting of circular primary phase regions of UO_2 surrounded by oxide-metal eutectic areas (see Figure 10, Section III) obtained during the solidification of non-eutectic oxide-rich mixtures. A solidification scheme for these and similar structures was proposed. Primary phase (UO_2) solidification was responsible for the circular UO_2 areas shown in Figure 10. Calculation of the eutectic composition in the eutectic regions of the oxide-rich UO_2-W samples indicated the composition of the liquid followed the metastable

extension of the liquidus line on the phase diagram and produced eutectic areas rich in tungsten (8 to 12 weight precent W in contrast to the proposed eutectic composition of 4 to 5 weight percent tungsten). Details of this analysis are scheduled for publication in the Journal of Crystal Growth (late 1971) and were discussed in the Semi-Annual Report[1] in January 1971.

Recent work involving the solidification of a number of oxide-rich samples (starting composition containing 5 weight percent tungsten) indicated the structure obtained with this oxide-metal ratio is strongly influenced by mechanical mixing occurring in the liquid. The composite structure shown in Figure 31 is typical of UO_2-W structures obtained during the solidification of oxide-rich mixtures in which the sample is rotated at several hundred rpm. Similar compositions, solidified without rotation, yield vertically banded structures consisting of alternate layers of pure oxide and oxide-metal eutectic growth as shown in Figure 32.

Comparison of the structures shown in Figures 31 and 32 leads to the interesting hypothesis that the mechanical mixing achieved by rotating the molten zone effectively alters the growth geometry, at least with non-eutectic oxide-rich mixtures. With rotation vertical regions of primary UO_2 form; during stagnant growth without rotation, the excess primary UO_2 forms horizontal layers. The mechanism leading to the banded samples may be interpreted as a cyclic process. As growth was initiated in the stagnant oxide-rich molten zone the primary oxide phase initially

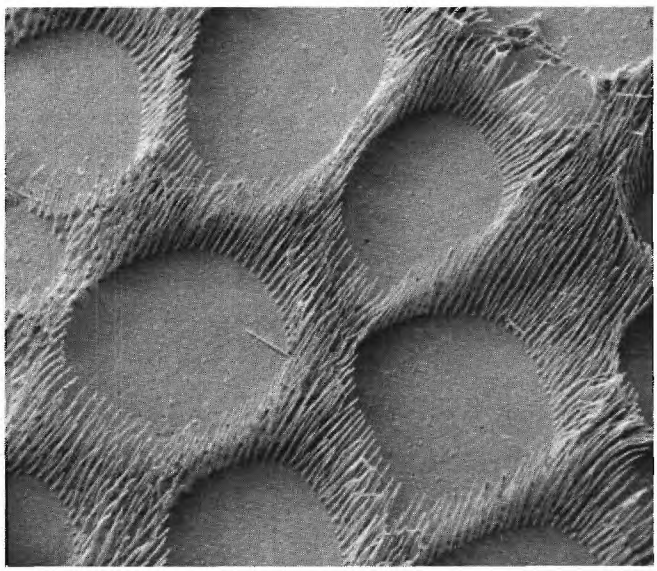

Figure 31. Transverse Section of UO_2-W Composite, Containing 5 Weight Percent W, Displaying Circular Regions of Primary UO_2 Surrounded by Eutectic Composite Regions. Sample Rotated at About 400RPM During Growth. Scanning Electron Micrograph, 650X.

Figure 32. Longitudinal Section of UO_2-W Composite, Containing 5 Weight Percent W, Exhibiting "Banding". Sample Was Grown Without Rotation With the Growth Direction From the Bottom to the Top of the Figure. Dark Field, 600X.

precipitated along the solidification front. Further growth depleted the UO_2 content of the liquid and the liquid composition adjacent to the solid approached the eutectic composition. At some point the simultaneous growth of the oxide-and-metal eutectic was initiated and coupled growth proceeded until the liquid was again oxide-rich relative to the eutectic composition. Then the eutectic growth terminated in favor of pure oxide solidification. Undoubtedly such a cyclic process would produce major temperature and growth rate fluctuations during solidification.

Comparison of the microstructures of UO_2-W samples of near eutectic composition, displaying uniform composite structures, grown at similar rates with and without rotation, suggests that the rotated samples contain larger diameter fibers with corresponding lower fiber densities than the samples grown without rotation. Further work is required to substantiate this observation.

C. EFFECT OF COMPOSITION AND GROWTH RATE ON FIBER DENSITY AND DIAMETER IN THE UO_2-W SYSTEM

A series of oxide-metal growth experiments were performed in the model system UO_2-W to determine the effects of composition and growth rate on fiber density and diameter. Samples were prepared by dry blending the correct weight percent W powder (-325 mesh) into the UO_2 (-325 mesh) powder, after which it was pressed into 3/4 inch diameter cylinders between one and two inches long

under a pressure of about 2300 psi. The preheating, melting and subsequent solidification of the UO_2-W samples was accomplished using a 4 mhz rf field. The sample was preheated to 1300° - 1400° C and held for half an hour for densification in the system shown in Figure 30. At this temperature the conductivity of the oxide-metal mixture was high enough to allow eddy current heating when exposed to the rf field.

Table VIII presents the results of solidifying UO_2 plus 10 weight percent W samples at rates between approximately 15 and 90 mm per hour. Figures 33 and 34 graphically show the effect of growth rate on fiber density and diameter. These Figures readily show that as the growth rate increases, fiber density increases. As fiber density increases, the fiber size decreases and varies from about 0.28 microns for the fastest grown sample to about 0.49 microns for the slowest grown sample. Typical oxide-metal structures are shown in Figures 35 and 36. The low density fiber structure (Figure 35) has significantly longer fiber lengths exposed than does the high density fiber structure (Figure 36). Figures 37 and 38 are SEM micrographs of a UO_2-W sample where the sectioning was almost parallel to the growth direction. During etching extended lengths of the fibers were exposed. These pictures readily show that when the composite growth is under adequate control, very long continuous fibers are obtainable.

In addition to the samples containing 10 weight percent W, a series of UO_2-W specimens containing 5 weight percent W were

TABLE VIII

INFLUENCE OF GROWTH RATE ON TUNGSTEN FIBER DENSITY AND DIAMETER DURING THE UNIDIRECTIONAL SOLIDIFICATION (WITHOUT ROTATION) OF UO_2 PLUS 10 WEIGHT PERCENT W MIXTURES

Sample Designation	Growth Rate cm/hr.	Fiber Density per $cm^2 x 10^{-6}$	Fiber Diameter Microns
3-14	1.6	14.8	0.49
3-11a	1.9	19.5	0.45
3-11	3.0	17.3	0.45
3-13a	3.2	22.4	0.34
3-1	5.0	25.0	0.33
3-9a	9.0	42.0	0.28

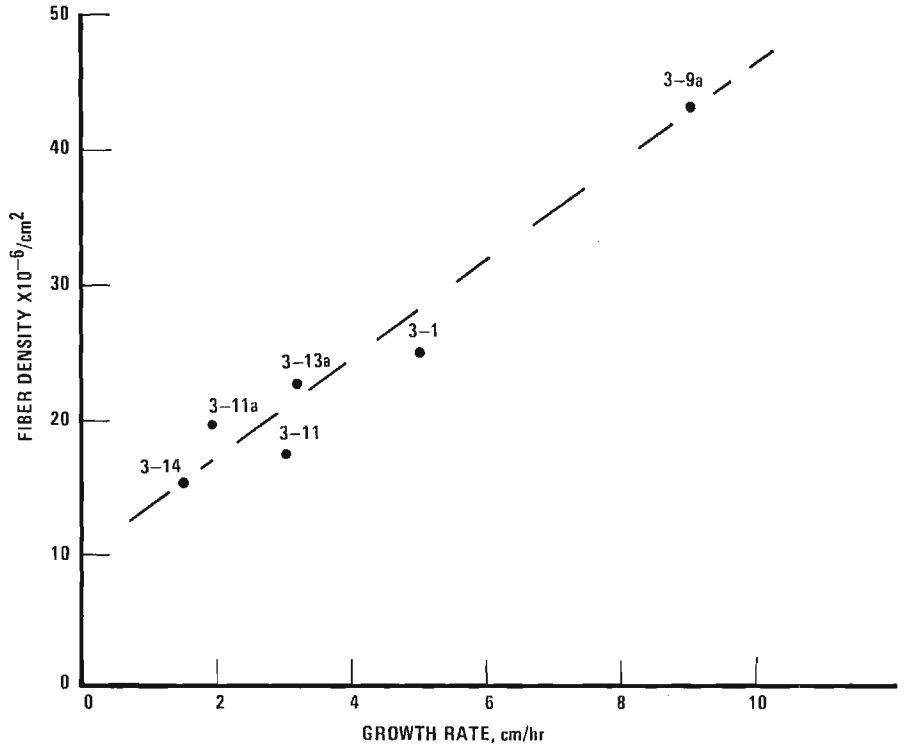

Figure 33. Affect of Growth Rate on Tungsten Fiber Density for UO_2-W Composites.

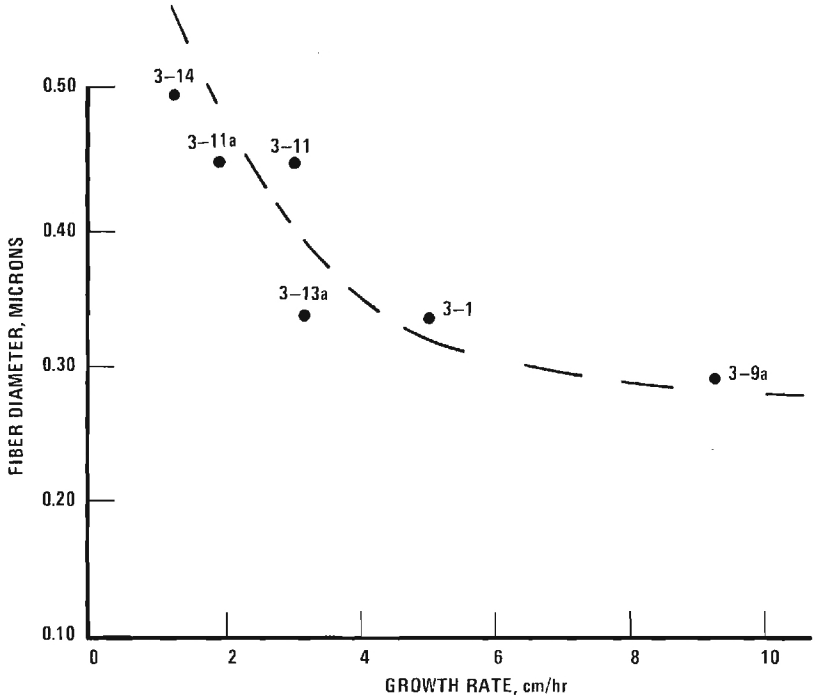

Figure 34. Affect of Growth Rate on Tungsten Fiber Diameter for UO_2-W Composites.

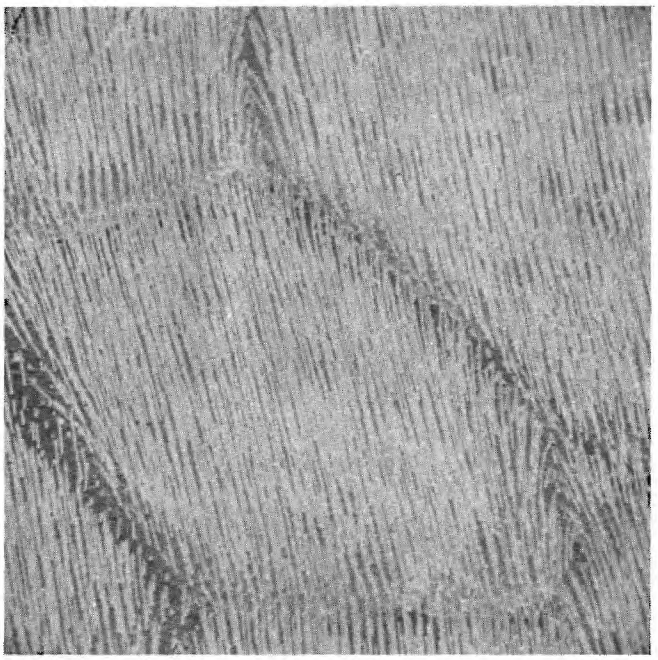

Figure 35. Scanning Electron Micrograph of UO_2-W Composite Containing Approximately 14.8 Million 0.49 Micron Diameter W Fibers Per Cm^2. 570X.

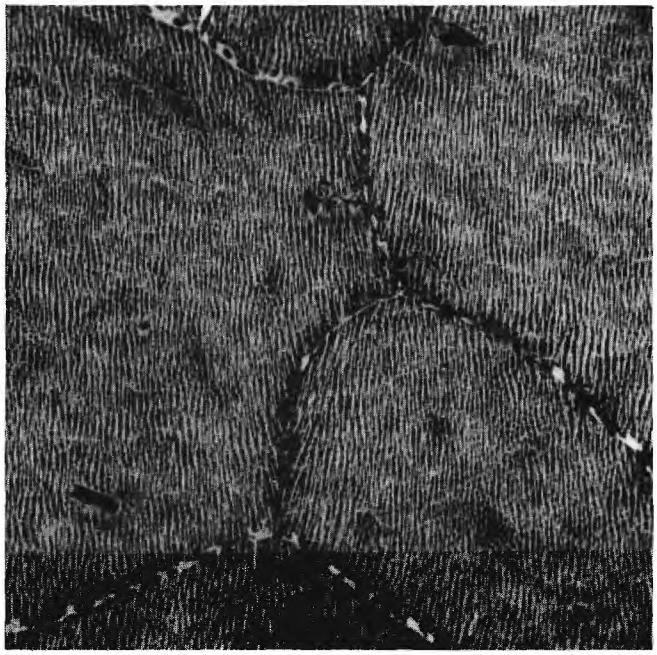

Figure 36. Scanning Electron Micrograph of UO_2-W Composite Containing Approximately 42 Million 0.28 Micron Diameter W Fibers Per Cm^2. 540X.

Figure 37. Scanning Electron Micrograph of Longitudinal Section of a UO_2-W Composite Showing W Fiber Continuity. 550X.

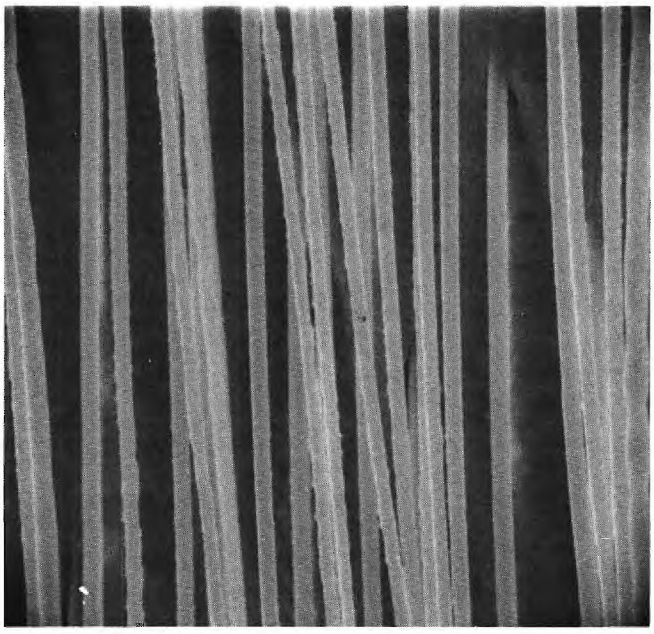

Figure 38. Scanning Electron Micrograph of Longitudinal Section of UO_2-W Composite Showing Uniformity of W Fiber Diameters. 5500X.

solidified. In all of these samples, regardless of growth rate, considerable "banding" (alternate layers of pure oxide and eutectic growth) was present. A proposed explanation for this behavior was given in Part B of this Section, "Analysis of Oxide-Metal Solidification".

D. COMPOSITE GROWTH IN THE STABILIZED ZrO_2-W SYSTEM

Eutectic solidification has been achieved in the stabilized ZrO_2-W system producing W fibers in the oxide matrix. The fibers were unidirectional, less than one micron in diameter and uniformly distributed with over ten million per square centimeter.

Sample preparation and preheating of the ZrO_2-W specimens was accomplished in a manner very similar to that described for the UO_2-W samples in the previous section, except for the addition of a stabilizing oxide. ZrO_2 requires stabilization to prevent a 9% volume increase caused by a phase transformation from monoclinic to tetragonal at about 1000°C. Additions of certain oxides induce a cubic structure by forming a solid solution with the ZrO_2 which is stable up to the melting point. The stabilizers used in this work were additions of 10.5 mole percent (5 weight percent) CaO, or 8.0 mole percent (14 weight percent) Y_2O_3. These powders were wet mixed, then calcined to remove all water before being mixed with the W metal powder. The CaO stabilized ZrO_2 apparently has a higher electrical conductivity, for it was easier to couple to than the Y_2O_3 stabilized material. However, Y_2O_3 has been used

as the stabilizer except in the preliminary experiments because the compound, $CaWO_4$, was formed during the melting of the CaO-ZrO_2-W mixtures. The inherent higher electrical resistivity of the ZrO_2 required the use of higher preheat temperatures (1500°-1600°C) and higher rf frequencies (7.5 or 16 mhz) than were necessary for the more conductive UO_2 (4 mhz).

Skin temperatures in the range of 1750°- 1850° C were maintained using the 16 mhz rf frequency to achieve good solidification. Lower temperatures resulted in a poorly melted sample containing many fine voids. Higher skin temperatures resulted in melting through the skin of the sample and the spilling of the internal molten material. Difficulty was encountered in holding the skin temperature in this range because the power input to the sample changed during composite growth. The surface temperatures were also difficult to determine due to vapor deposits forming on the silica tube which impeded the taking of accurate optical pyrometer readings. Improved containment of the molten interior was achieved by melting the ZrO_2-W mixtures using a 7.5 mhz rf field. At the lower frequency there was more rf penetration into the sample which resulted in a greater unmelted skin thickness and, consequently, higher internal temperatures could be achieved without spilling the molten liquid.

A number of oxide-metal growth geometries have been observed during the solidification of stabilized ZrO_2-W mixtures. Figures 39 and 40 are typical of the uniform eutectic growth.

Figure 39. Transverse Section of a Stabilized ZrO_2-W Composite. Dark Field, 200X.

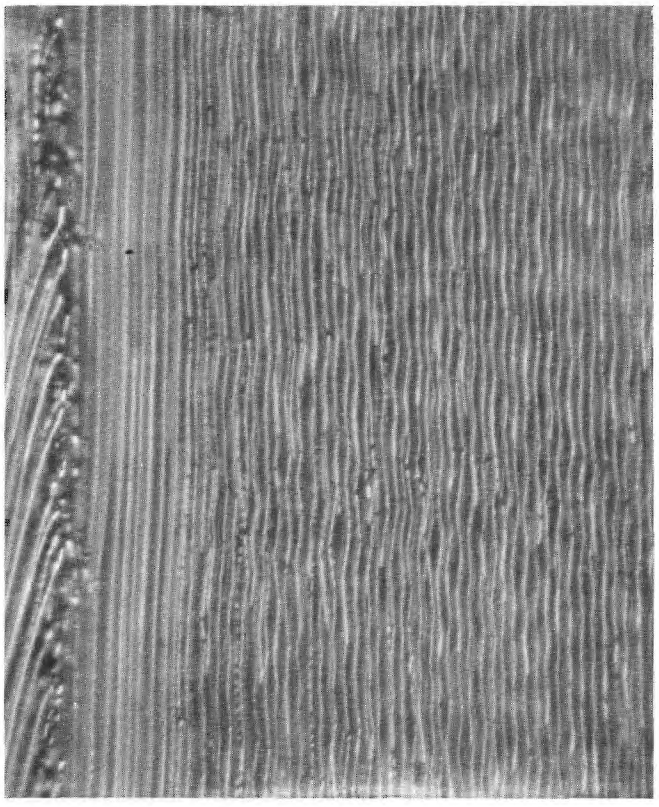

Figure 40. Longitudinal Section of the Stabilized ZrO_2-W Composite. Dark Field, 600X.

Several forms of non-uniform growth have also been observed. "Banded" structures have been observed in which a sudden discontinuity stops the W fiber growth for a distance of a few hundred microns before it starts again. Areas containing circular regions of primary ZrO_2 without fibers have also been observed. The eutectic region surrounding the pure oxide contained fibers that were not continuous. Dendrites of tungsten mixed with the fibers were also seen in some areas.

Some preliminary chemical etching of ZrO_2-W samples was performed to gain fiber geometry information as well as to investigate the potential of achieving suitable pin geometries for electron emission testing. Etching the ZrO_2-W composites in 48% HF for 25 minutes exposed the W fibers only slightly. However, this etch gave enough topographical relief to the sample for SEM examination as shown in Figure 41. Etching the composite in a mixture of 5g NaOH, 15g $K_3Fe(CN)_6$ and 100ml H_2O at 35°C for 15 minutes dissolved the W fibers leaving fine holes in the oxide matrix, Figure 42.

Calculations made using a scanning electron micrograph of a ZrO_2 sample containing 8 mole percent Y_2O_3 and 15 weight percent W showed the W fibers to be 0.6 microns in diameter with a density of 13.2×10^6 fibers per square centimeter. The calculated oxide-metal composition in the area of uniform eutectic growth was 11.6 weight percent tungsten and 88.4 weight percent stabilized ZrO_2.

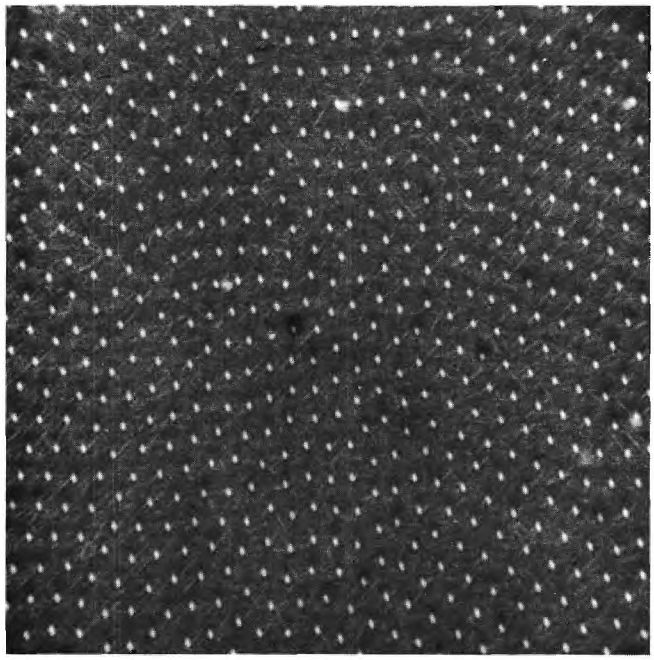

Figure 41. Scanning Electron Micrograph of Stabilized ZrO_2-W Composite Showing Slightly Exposed W Fibers After HF Etch. 1300X.

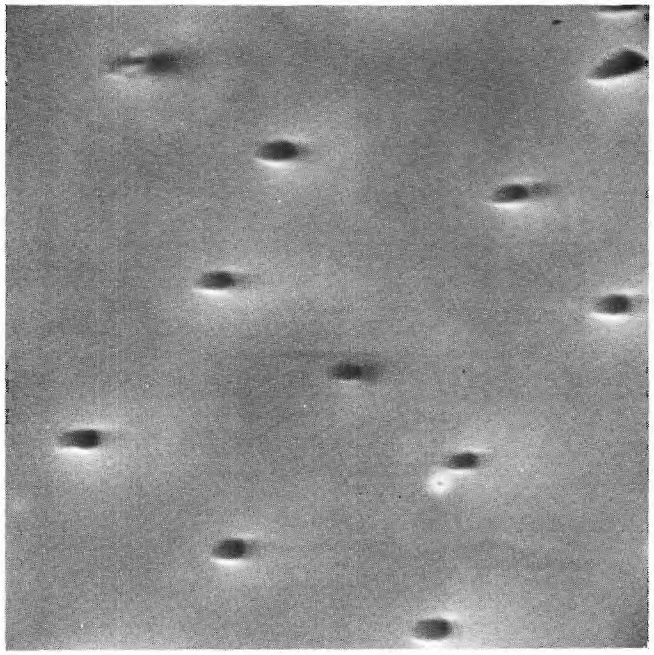

Figure 42. Scanning Electron Micrograph of Stabilized ZrO_2-W Composite After Chemical Etching to Remove the W Fibers. 6300X.

E. PARAMETERS AFFECTING SUCCESSFUL REFRACTORY OXIDE-METAL COMPOSITE GROWTH

One of the major project objectives was to delineate the parameters leading to successful eutectic growth in refractory oxide-metal systems. As anticipated this task turns out to be a complex problem with the interaction of many chemical, mechanical and physical variables. The experience gained melting numerous UO_2-W and ZrO_2-W mixtures and pure oxides under a variety of conditions was used to formulate the following list (shown in Table IX) of parameters influencing successful growth.

This list also includes many of the parameters, listed in Section II of this Report, believed to influence the rf melting behavior of pure oxides, oxide mixtures and metal-oxide systems containing refractory metals other than tungsten. Although most of these parameters are interrelated and it is impossible to conclusively document the effect of each at present, some insight into the influence of the variables such as oxide-metal ratio, growth rate, rf frequency, melting temperature, mechanical mixing etc., has been presented throughout this Report.

F. CHEMICAL ETCHING OF UO_2-W COMPOSITES

Chemically etched UO_2-W composites were used for emission testing and to analyze the influence of growth parameters on oxide-metal geometries through the use of scanning electron micrographs.

TABLE IX

PARAMETERS INFLUENCING COMPOSITE GROWTH IN REFRACTORY OXIDE-METAL SYSTEMS

1. Oxide-metal ratio
2. Growth rate
3. Metal powder characteristics
4. High-temperature electrical conductivity
5. Rf frequency
6. Mixing of the liquid (sample rotation)
7. Melting (eutectic) temperature
8. Preheat temperature
9. Sample density
10. Sample rf-coil geometry
11. Quantity of liquid and void size
12. Oxygen partial pressure
13. Pre- and post-heater separation
14. Vapor pressure
15. Variable oxide stoichiometry

The technique used to selectively remove the oxide layer and expose the tungsten fibers was described previously[1] and is briefly reviewed. Additional etching studies have been initiated into ways to produce pointed tungsten fibers for enhanced field emission and also ways to chemically remove the tungsten pins and leave the oxide matrix unaffected.

The etchant routinely employed to expose the W fibers in UO_2-W composites consisted of:

(1) 20 ml saturated chromic acid

(2) 10 ml glacial acetic acid

(3) 7 ml concentrated nitric acid

(4) 5 ml 48% hydrofluoric acid

During the etching process to expose the W fibers, wafer shaped UO_2-W samples were rotated in this solution at 20-30rpm for a predetermined amount of time, then rinsed by rotation in a water bath and ultrasonically cleaned in water. The etching time was varied from one to sixty minutes depending upon the length of fiber to be exposed. In a study of exposed fiber length versus etching time a linear relationship between these variables was found. A UO_2-W sample (3-1) was etched for successive periods of 20, 40, and 60 minutes; the exposed fiber lengths were 2.98, 5.61, and 8.24 microns respectively. These lengths were determined from SEM micrographs using the following formula:

$$F = \frac{P}{\cos\alpha M} \qquad \text{(Eq. 1)}$$

where: F = actual fiber length

P = projected fiber length as measured from SEM micrograph

$\cos \alpha$ = tilt angle (SEM viewing angle)

M = magnification

Results of these measurements are shown in Figure 43.

In the formation of optimum emitting arrays, it would be advantageous for enhanced field emission to alter the shape of the W pins such that they are pointed instead of rod-shaped fibers. Initially, it was thought that chemical and electrolytic etching techniques used to shape emitter tips for the field ion microscope could be used to thin the metal pins of the composite. Various alkali hydroxide solutions and double layer solutions were tried but were unsuccessful, as the hydroxide solutions severely attacked both fibers and matrix. Some promising results were obtained using a dilute Na_2CO_3 electrolytic etching solution with the UO_2-W composites.

During routine etching of UO_2-W composites to expose the W fibers using the standard chromic acid etch, it was noted that random fibers and occasionally large areas of fibers became pointed after about 30 minutes of treatment. Intentional variations of the composition of the standard etch were made to assess its influence on the shape of the W fiber tips. Preliminary results indicated that a slight increase in the HF concentration (from 5 to 6 ml) and an increase in etch temperature from 25°C to 40°C

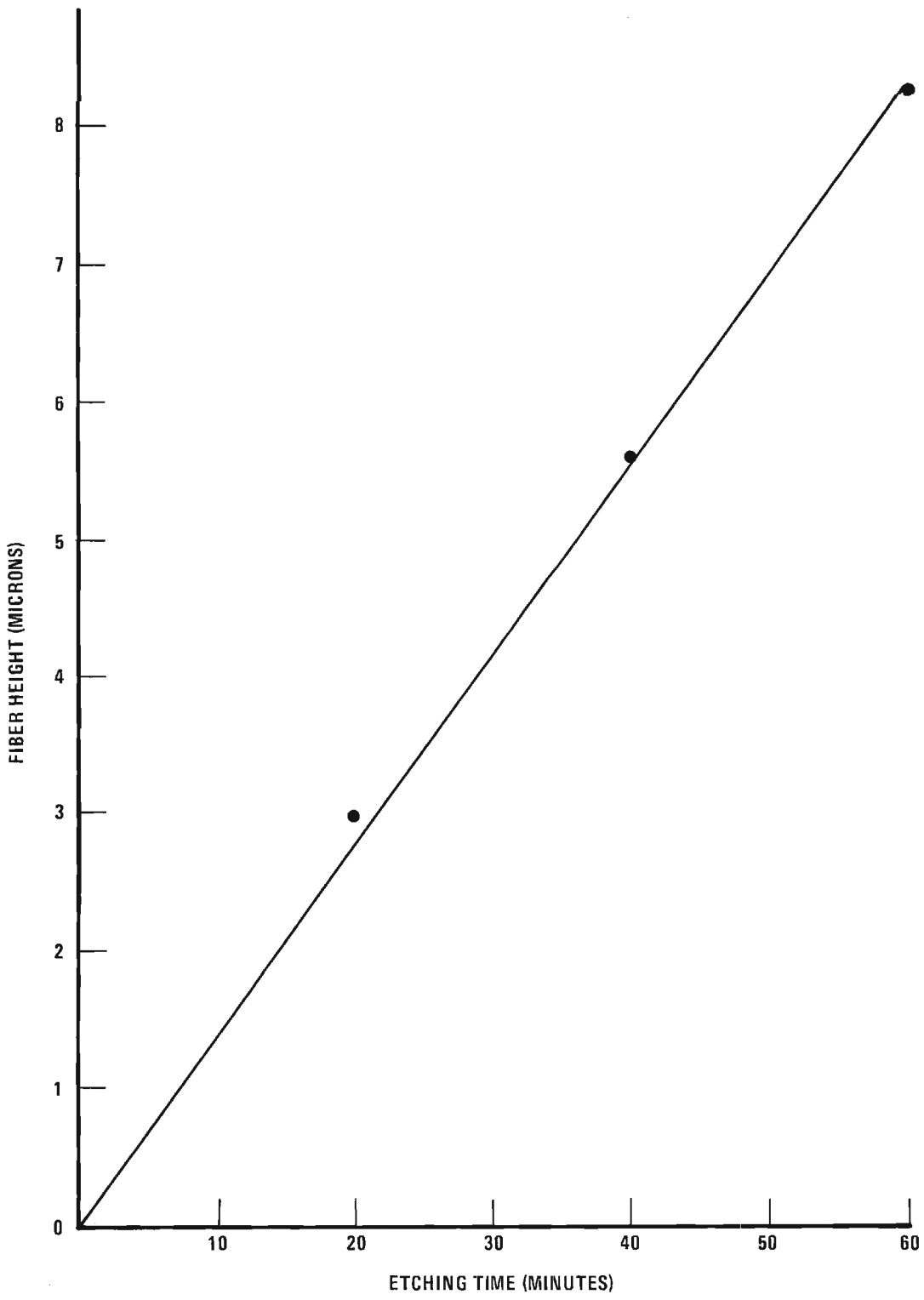

Figure 43. Etching Time Versus Exposed Fiber Heights for Chemically Etched UO_2-W Sample No. 3-1.

produced well-pointed W fibers using the standard etching procedure. Figure 44 shows a typical UO_2-W composite after etching with the solution containing the higher concentration of HF at 40°C. The increased attack on the W fibers may be due to an interaction between W, HNO_3 and HF[7] at slightly elevated temperatures.

Techniques to selectively dissolve the tungsten fibers without affecting the UO_2 matrix are also under investigation. In field emission such structures could be used to incorporate a resistance (the inherent resistance of the oxide) in series with each emitting pin. Such a resistance should effectively reduce the voltage seen by the pins drawing an excessive share of the current and, hopefully, equalize the current per pin. Toward this end several chemical etchants were tried. An acid mixture of HF and HNO_3 was studied and discarded because of damage to the UO_2 matrix. A molten salt bath of NaOH was also studied; handling difficulty discouraged further use of this method. Encouraging results were obtained using an etchant composed of a 1:1 volume ratio of 10% NaOH and 30% $K_3Fe(CN)_6$. The etching procedure consisted of rotating the UO_2-W sample in the etchant solution (35°C) at 20 rpm for 15 minutes. SEM analysis, Figure 45, showed many uniformly spaced holes in place of the W fibers. Some attack on the UO_2 was noted; slight concentration changes or shorter etching time may reduce the attack on the oxide matrix. A method of measuring hole depth based on changes in electrical resistance is also being developed.

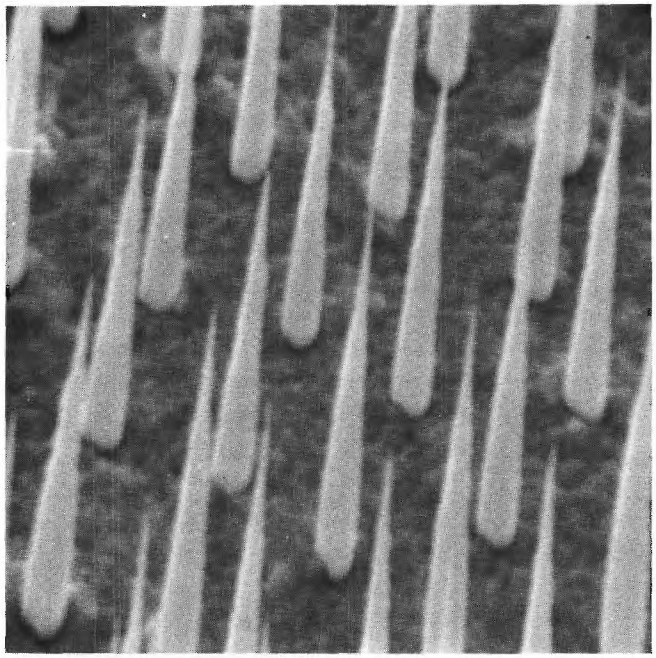

Figure 44. Scanning Electron Micrograph of UO_2-W Composite Displaying Pointed W Fibers After Treatment With Etchant Containing Increased HF Concentration. 8700X.

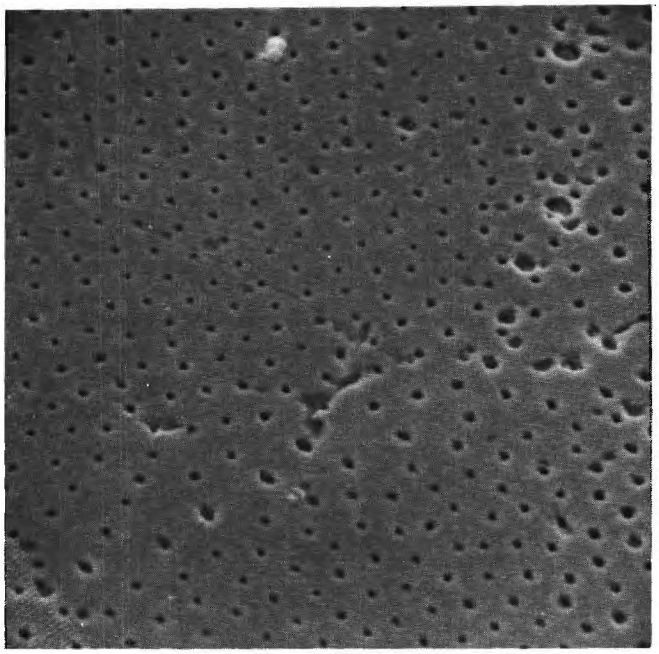

Figure 45. Scanning Electron Micrograph of UO_2-W Composite After Chemical Etching to Remove the W Fibers. 2200X.

SECTION V

FIELD EMISSION THEORY AND EXPERIMENTAL MEASUREMENTS

This chapter presents a detailed summary of the status of the present research on the high field electron emission from UO_2-W oxide-metal composites. A brief discussion of the basic field emission theory is first given, followed by a description of the experimental apparatus and the presentation of typical experimental results. These experimental results are discussed in detail and critically evaluated with the aid, whenever possible, of the previously developed theory.

A. FIELD EMISSION THEORY

This section presents a brief summary of field emission theory as it applies to single pins, a recapitulation of the simplified multiple pin array theory as analyzed by Levine[8] and finally some numerical calculations applicable to the present research.

Field emission (or high field emission) is a quantum mechanical phenomenon dependent upon the electrons tunneling through the surface barrier potential that normally contains them within the material. By the use of reasonable approximations,

the microscopic current density for pure field emission* (T=0°K) can be shown to have the form[9]

$$J = \frac{1.54 \times 10^{-6} F^2}{\phi} \exp\left[-\frac{-6.83 \times 10^{7} \phi^{3/2} f(y)}{F}\right] A/cm^2 \qquad \text{(Eq. 2)}$$

where ϕ is the work function in eV, F is the electric field in V/cm and f(y) is Nordheim's elliptic function that includes the effect of the image force. The function f(y) where

$$y = \frac{3.79 \times 10^{-4} F^{\frac{1}{2}}}{\phi} \qquad \text{(Eq. 3)}$$

is tabulated for various values of F. However, f(y) varies slowly with y and may be taken as 1.0 unless great accuracy is required.

1. Single Pin Emission Theory

In the usual situation where it is desired to calculate the field emission current density, the microscopic electric field intensity F is not directly known, but must be calculated from a knowledge of macroscopic applied voltages and geometrical factors. For a simple case such as two parallel plates separated by a distance d this presents no problem since

$$F = \frac{V}{d} \qquad \text{(Eq. 4)}$$

*For temperatures below which there is no appreciable thermionic emission this is a good approximation. At higher temperatures where both thermionic and field emission are present (T-F emission), the emission equation does not have a closed form solution. T-F emission is greatly increased over pure field emission at the lower field strengths, but is only increased slightly at the higher field strengths.

where V is the applied voltage. However, for a complex geometry such as a field emission microscope pin tip, the determination of the microscopic electric field as a function of the applied V is quite difficult. Once the microscopic field intensity has been obtained, the average macroscopic current density can be found by integrating over the emitter area and dividing by the total area of the emitter. The parameter β that relates the applied V to the microscopic electric field intensity F at each point on an emitter through

$$F = \beta V \qquad \text{(Eq. 5)}$$

has been approximated for a few single pin geometries. As one example, the field intensity at the vertex of a hyperbolic pin is given by[9]

$$F = \frac{2V}{r} \log \frac{2R}{r} \qquad \text{(Eq. 6)}$$

and thus

$$\beta = \frac{2}{r} \log \frac{2R}{r} \qquad \text{(Eq. 7)}$$

where r is the pin radius at the tip and R is the distance to the anode. If β cannot be calculated the relationship

$$J = C V^2 \exp - \frac{D}{V} \qquad \text{(Eq. 8)}$$

is still valid qualitatively, where the empirical constants C and D implicitly contain β .

The constants C and D are often obtained from what is called a Fowler-Nordheim plot. This plot is also used as a first order

check on the applicability of the Fowler-Nordheim field emission theory to a particular situation. If Equation (8) is divided by V^2 and the logarithm of both sides taken, one obtains

$$\log \frac{J}{V^2} = \log C - \frac{D}{V}. \qquad \text{(Eq. 9)}$$

Equation (9) is a straight line when $\log \frac{J}{V^2}$ is plotted as a function of 1/V with slope equal to -D and intercept equal to log C. Thus the values of C and D can be obtained from a given set of experimental data. If additional information is available, C and D can be broken into their various factors containing β, ϕ etc.

2. Multiple Pin Arrays

The total current obtainable with a single field emitter pin is obviously limited by the onset of thermal damage to the pin. This damage threshold can be increased with a consequent increase in maximum current by the use of a larger radius pin. However, this in turn requires a larger applied potential in order to compensate for the decreased microscopic electric field of the larger pin. A better approach would be to increase the total number of pins and thus realize the increased current with no penalty in voltage. The emitter geometry developed in the present research offers considerable promise in the accomplishment of this heretofore unattainable objective. Unfortunately, when a large number of pins are grouped together to form a two dimensional array, the emission capability is increased, but not as a simple summation

over the total number of pins. This fact is obvious when one considers the two extreme cases. First assume that the array consists of only a very few pins placed far apart. The electric field at the tips of these isolated pins is unaffected by the other pins and the total current is the sum of the individual pin currents. However, the macroscopic current density is small and a large emitter is required to achieve a useful total current. In the other extreme case, where the pins are so close together that they almost touch, the electric field at the tips of the pins is small since the array of pin tips now approximates a plane surface. In this case the pin density is high, but the current per pin is again low resulting in a small macroscopic current density. Thus there must exist some optimum pin spacing for which the maximum macroscopic current density occurs.

A simple model that predicts the emission from a dense two dimensional array of tungsten pins was presented in the Semi-Annual Report[1] and is repeated here in a somewhat different form for completeness. The relevant equation relating the macroscopic field emission current density J to the actual electric field at an emitter tip of radius r for a square array of side "a" is given by

$$J = f \frac{\pi r^2}{a^2} B F^2 \exp - \frac{F_r}{F} \qquad \text{(Eq. 10)}$$

where B and F_r each contain several factors that are written individually in Equation (2). This equation is simply derived from Equation (2) by first assuming that the effective emitting area per

pin is πr^2 and that the density of pins per square centimeter is a^{-2}. The correction factor f, where f is given by

$$f = f_{area} \times f_{polar} \times f_{dist} \qquad \text{(Eq. 11)}$$

is used to include corrections for possible nonuniform emission over a pin tip, f_{area}; the effects of polarization due to adsorbates, f_{polar}; and the effects of nonuniform pin tip radii, f_{dist}. In all cases f must be less than or equal to one. The presence of a very dense array causes the electric field F at each emitter tip to be reduced according to the law

$$F = \frac{V}{kr} \qquad \text{(Eq. 12)}$$

where V is the applied voltage, r is the pin tip radius, and k is given by

$$k = \left(1 + \frac{4\pi Lr}{a^2}\right) . \qquad \text{(Eq. 13)}$$

The dependence of k on L (the interelectrode spacing), r and "a" was derived by superposing a one-dimensional potential and a square array of coulomb potentials and by matching the boundary conditions at each pin tip. The effect of pin height was not considered, so the value of k given in Equation (13) is probably a lower limit. Clearly one would desire k to be as small as possible so that excessive voltages need not be applied. If the pin radius, electrode spacing and anode voltage is known, the value of pin spacing that will result in the maximum macroscopic current density J can be calculated from

$$a_{optimum} = 2\pi rL \left[(1 + x) + (1 + 6x + x^2)^{1/2} \right]^{1/2} \quad \text{(Eq. 14)}$$

where $$x = r \frac{F_r}{V} \quad \text{(Eq. 15)}$$

Note that this value of "a" is that for the maximum macroscopic current density and not for the maximum ratio of the macroscopic current density to the current density per isolated pin as was presented in the Semi-Annual Report.[1]

3. Effects of Nonuniform Emission Over a Pin Tip

If a tip has appreciable emission from only certain facets then the fractional emitting area is less than unity and f_{area} is less than one. If there is a monolayer of adsorbate, then polarization effects cause the barrier height to increase, and theoretical calculations have been made[10,11] which show that

$$f_{polar} = \exp(-GN), \quad \text{(Eq. 16)}$$

where G depends on the polarizability and the effective dielectric constant of the monolayer with N being the number of adsorbed molecules/cm^2. Experimental results[12] show that one may expect $f_{polar} = 0.05$ for a full monolayer of O_2 on W, $f_{polar} = 0.006$ for a full monolayer of CO on W and f_{polar} as low as 0.5×10^{-4} for a fractional monolayer of H_2 on W. Clearly, there is a large penalty to pay for having a monolayer of adsorbate present on the surface of a field emitter tip.

4. Effects of a Distribution of Pin Radii

It would indeed be a fortuitous situation if an emitter array with all identical pins could be fabricated. However, such is not likely to be the case and the best that one can reasonably hope to achieve is a known distribution of pin radii, hopefully quite narrow. This section examines theoretically the effects of a pin radius distribution on the observed emission. Later in the present section, numerical examples are presented that vividly illustrate the importance of a uniform pin radius.

Suppose that all (10^6 pins per cm^2) of the pins have the same radius except for a select few which have a significantly smaller radius. Then the total J-V characteristic would show an easily observable summation of the several characteristics. But suppose that observation showed on a certain sample that the Fowler-Nordheim plot was a straight line over many orders of magnitude. Is this proof that the emission is uniform? The answer is no, and the reason can be traced to the possibility of certain distributions of pin tip radii. For example, consider an exponential distribution defined by

$$f(r) = \begin{cases} \exp(+gr) & r_1 \leq r \leq r_2 \\ 0 & \text{otherwise} \end{cases} \qquad \text{(Eq. 17)}$$

where g is a measure of the "steepness" of the distribution. The upper radius r_2 cannot be larger than half of the cylindrical pin diameter. The width of the radius distribution will be called w

where

$$w = r_2 - r_1. \qquad \text{(Eq. 18)}$$

From the definition of the average current density $\bar{J}$, one has

$$\bar{J} = \frac{\int_{r_1}^{r_2} J(r)\, f(r)\, dr}{\int_{r_1}^{r_2} f(r)\, dr}. \qquad \text{(Eq. 19)}$$

By using a simplified form of Equation (10)

$$J(r) = C_1 \exp\left(-\frac{F_r\, k\, r}{V}\right) \qquad \text{(Eq. 20)}$$

the integrals can be performed easily and the general result is

$$\bar{J} = \frac{g\, C_1 \left\{ \exp\left[-\left(\frac{F_r\, k}{V} - g\right) r_1\right] - \exp\left[-\left(\frac{F_r\, k}{V} - g\right) r_2\right] \right\}}{\left(\frac{F_r\, k}{V} - g\right) \left[\exp(g\, r_2) - \exp(g\, r_1) \right]} \qquad \text{(Eq. 21)}$$

For V sufficiently small so that $\frac{F_r\, k}{V\, g}$ is greater than one, it can be shown that

$$\bar{J} \longrightarrow f_{dist}\ C_1\ \exp\left(-\frac{F_r\, k\, r_1}{V}\right), \qquad \text{(Eq. 22)}$$

where

$$f_{dist} = \frac{g\, V}{F_r\, k} \exp(-gw). \qquad \text{(Eq. 23)}$$

Suppose that w is 0.3×10^{-4}cm, F_r is 6.5×10^{8}V/cm, k is 2.0, V is 6.5 kV and g is 2×10^{5}cm^{-1}. Then gw is 6.0 and f_{dist} is approximately 0.0025. For V sufficiently large so that $\frac{F_r\ k}{V\ g}$ is less than one, it can be shown that

$$\overline{J} \longrightarrow C_1 \exp\left(-\frac{F_r\ k\ r_2}{V}\right), \qquad \text{(Eq. 24)}$$

or f_{dist} is unity for this high voltage regime. A crossover between the two regions, each having a V^{-1} dependence in the exponential, occurs at

$$V_c = \frac{F_r\ k}{g} \qquad \text{(Eq. 25)}$$

and the width of the transition region is

$$\Delta V = \frac{V_c}{g\ w}\ . \qquad \text{(Eq. 26)}$$

For the above example, one computes that V_c is 6.5 kV and V is 1.1 kV. This means that if measurements are made in the extensive range of from zero to 6.0 kV, a plot of log J as a function of V^{-1} (or a plot of $\frac{J}{V^2}$ as a function of V^{-1}) will be nearly a straight line and that one may not be aware of a distribution of radii. The penalty for having a distribution of radii is that f_{dist} is small. In the example given, only one pin in 400 is operating with a substantial current. Other distributions were also

considered, besides the exponential distribution given in Equation (17). For example a uniform distribution given by

$$f(r) = \begin{cases} 1 & \text{for } r_1 \leq r \leq r_2 \\ 0 & \text{otherwise} \end{cases} \qquad \text{(Eq. 27)}$$

similar considerations were drawn. For a Gaussian distribution

$$f(r) = \exp\left[-\rho (r - r_m)^2 \right] \qquad \text{(Eq. 28)}$$

where ρ is related to the variance of the distribution and r_m is the mean radius, it was found that a plot of log J as a function of $(V + V_0)$ gives a straight line. The constant V_0 is given by

$$V_0 = \frac{F_r \, k}{4 \, r_m} \, . \qquad \text{(Eq. 29)}$$

The present theory, although primitive, provides some interesting insight into the observed experimental behavior. Equations (10) and (13) can be combined, with (in the absence of any specific information) f taken as unity, to give

$$J = \frac{r^2}{a^2} \, B \, V^2 \left(1 + \frac{4 \, L \, r}{a^2}\right)^{-2} \exp\left[\frac{F_r \, r \left(1 + \frac{4 \, L \, r}{a^2}\right)}{V} \right] . \qquad \text{(Eq. 30)}$$

This equation, with the pin radius r as the parameter is plotted as a function of V in Figure 46. Growth parameters typical of routinely grown UO_2-W structures were used in the equation. Since

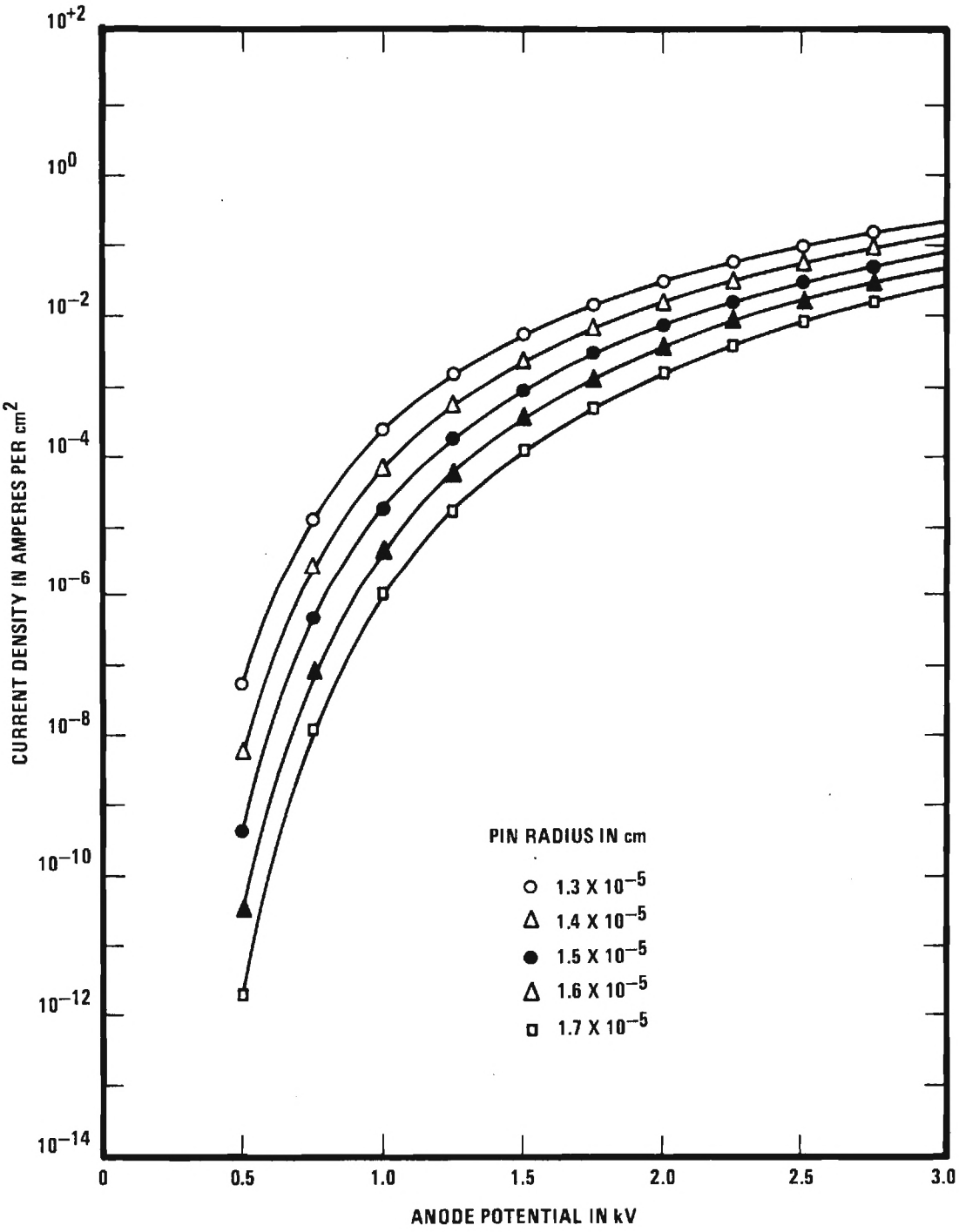

Figure 46. Theoretical Variation of Current Density as a Function of Anode Potential for Various Values of Pin Radius. The Inter-electrode Spacing and Pin Spacing Were Fixed at 0.010 Inches and 4.0×10^{-4} Cm Respectively.

only a qualitative analysis was desired, the constants F_r and B were obtained by roughly fitting Equation (30) to typical experimental data. The values of the parameter r are chosen to give approximately a ten percent variation of r between members of the family. The strong dependence of the current density upon the pin radius is obvious from Figure 46.

The dramatic effect of pin spacing upon the total macroscopic current density is illustrated in Figure 47. This curve clearly shows that for a given pin radius, anode voltage and interelectrode spacing that there exists an optimum pin spacing for maximum macroscopic current density. The position of the maximum is seen not to change rapidly with anode voltage as predicted by Equation (14).

B. DESCRIPTION OF THE EXPERIMENTAL FACILITY

A partial description of the prototype experimental apparatus was given in the Semi-Annual Report[1]. Since that time the experimental apparatus has undergone several significant changes that have resulted in a substantial improvement in experimental capability. This section describes the experimental apparatus as it now exists.

1. Vacuum System

An overall view of the entire experimental apparatus is shown in Figure 48. As can be seen from the photograph, the

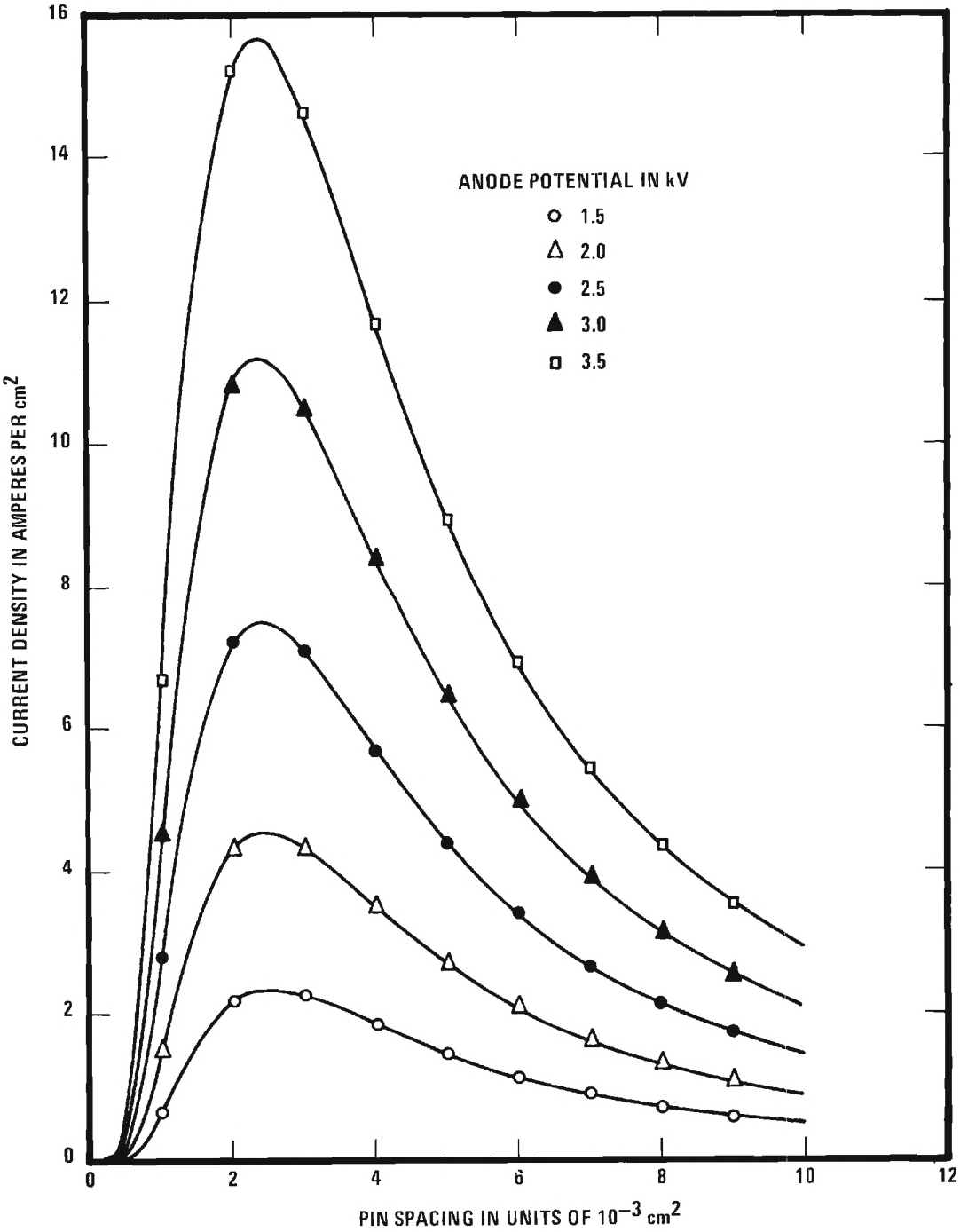

Figure 47. Theoretical Variation of Current Density as a Function of Pin Spacing for Various Values of Anode Voltage. The Interelectrode Spacing and Pin Radius Were Fixed at 0.010 Inches and 1.5 x 10^{-5}Cm Respectively.

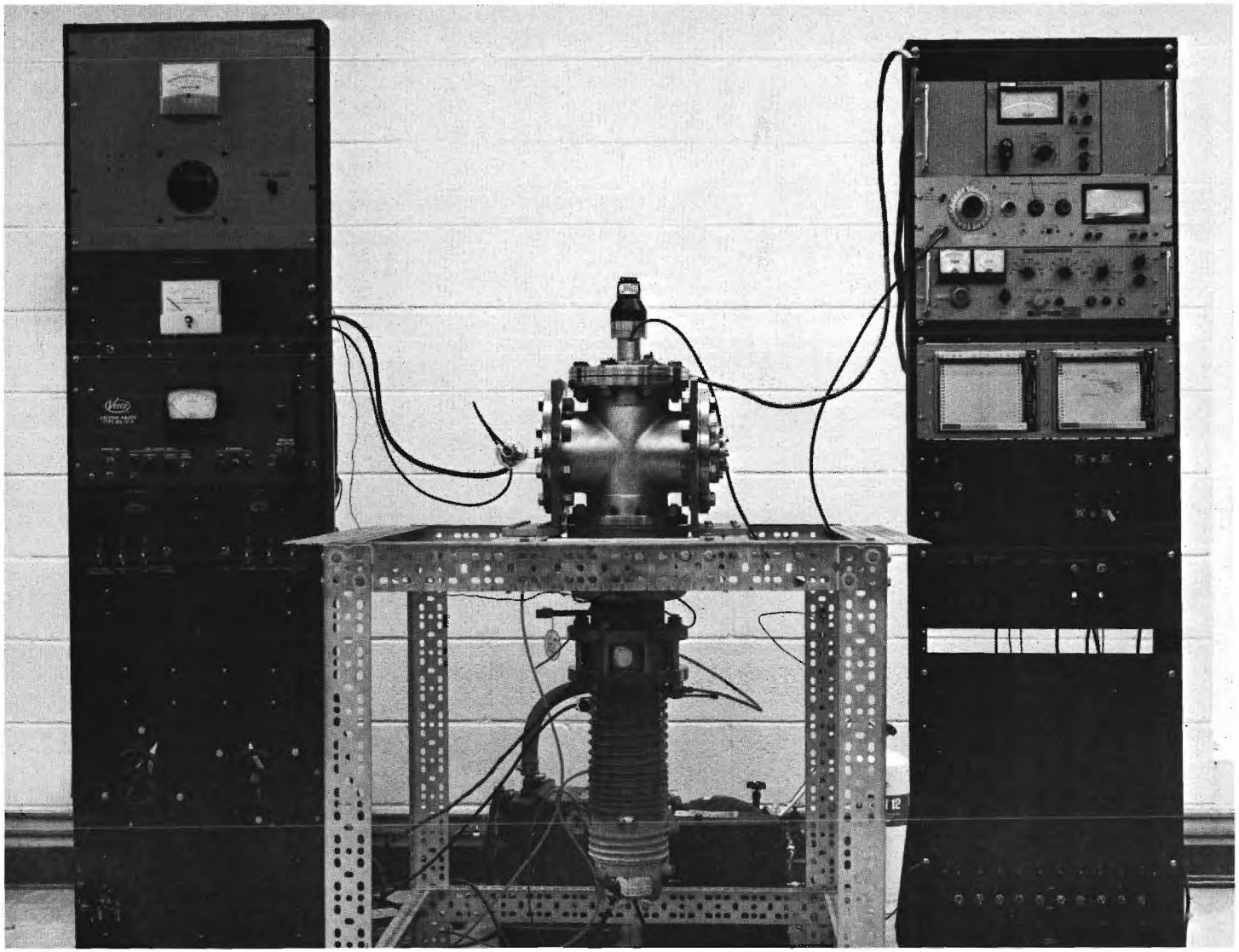

Figure 48. Overall View of the Electronic Experimental Apparatus.

vacuum enclosure is a "cross" configuration. The vacuum chamber and all vacuum components are made from stainless steel or other materials compatible with ultrahigh vacuum requirements. All vacuum seals are either of the aluminum o-ring or commerical Con-Flat types. The pumping system consists of a four-inch oil diffusion pump, Consolidated Vacuum Company type PMCU-4B, followed by a water cooled chevron baffle, type BCRU-40 and a zeolite molecular sieve trap, type TSMU-40. The diffusion pump is charged with Dow Corning Corporation type DC-705 silicone diffusion pump fluid.

The zeolite trap and vacuum chamber walls are heated to approximately 370° C and 200° C respectively for a period of from 24 to 36 hours. A resistive heating mantle is employed to heat the trap while an electrically heated oven is used to heat the vacuum chamber. After bakeout the trap heating mantle is switched off and the trap is cooled. When the trap has cooled for approximately one hour the vacuum chamber bakeout is turned off and the apparatus is allowed to cool. After a cooling period of about 12 hours, the pressure in the vacuum system is approximately 2.0×10^{-9} Torr as measured by a Bayard-Alpert type ionization guage.

2. Test Diode

A photograph of the test diode assembly is shown in Figure 49. The test diode is mounted to an experimental support

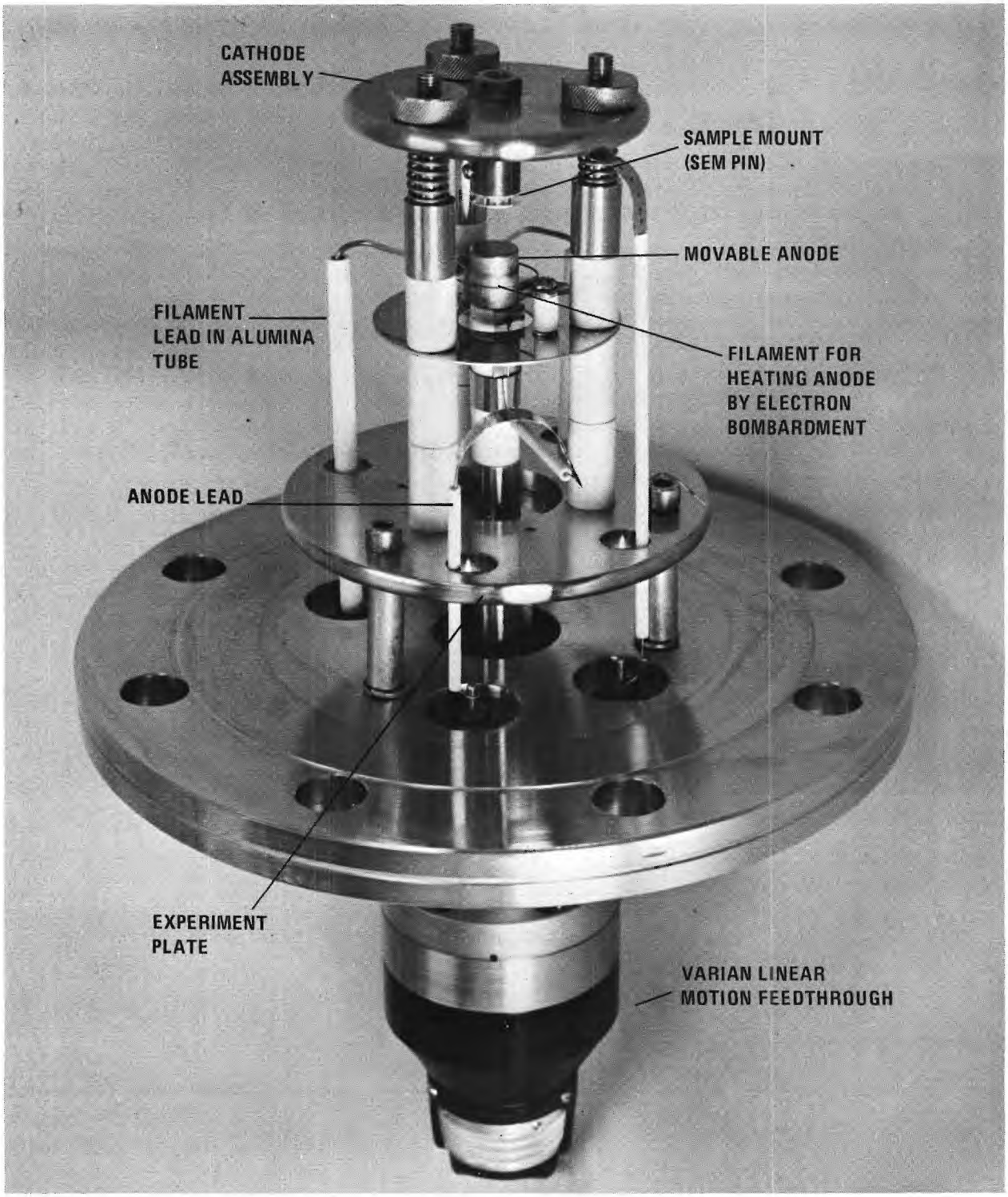

Figure 49. Photograph of the Test Diode Assembly.

plate which is suspended from the flange mounted on the top port of the cross. The plate is fastened to the flange in such a manner as to prevent mechanical stresses in the flange from being transmitted to the test diode.

As can be seen in Figure 49, the anode is secured to a Varian Model 954-5049 Linear Motion Feedthrough that provides a direct readout of the interelectrode spacing in 0.001 inch increments. Lateral guidance for the movable anode is provided by an adjustable bushing fastened to the experimental support plate. The anode is made from a molybdenum rod with a machined and polished face. The field emission cathode mount is also made from molybdenum, but is drilled to receive the pins used for mounting samples for viewing in the SEM. Such a feature is desirable to ensure the integrity of the sample while transporting it between the test diode and the SEM. The entire cathode mount assembly is secured by spring-loaded screws and can be positioned to compensate for a sample with slightly non-parallel faces. Also visible in Figure 49 is the tungsten wire filament used as a source of electrons for outgassing the anode by electron bombardment.

3. Instrumentation

The electronic instrumentation is mounted in the right-hand relay rack as shown in Figure 48. The left-hand relay rack contains the vacuum pump and chamber bakeout controls.

A Keithley Model 610R Electrometer is used for the DC emission measurements. Regulated DC power is supplied by a Fluke Model 413C Power Supply. This supply provides up to 3100 volts at 20 mA with an accuracy of $\pm$0.25 percent. Two Mosely Model 680 strip chart recorders are included for monitoring parameters such as electron current and pressure as a function of time.

When AC measurements are made, the power is supplied by a 6880 volt 0.291 A plate power transformer. By the use of appropriate multipliers and shunts, the AC current and voltage waveforms are displayed on a Tektronix Model 531 Oscilloscope. Several oscilloscope cameras are available for permanently recording the AC mode experimental data.

C. EXPERIMENTAL APPROACH AND PROCEDURES

Measurements of the total high field electon emission current were directed toward the evaluation of individual emitter samples with respect to various growth parameters and the determination of possible optimum or quasi-optimum operating conditions. Direct current electron emission measurements were selected as the primary tool in these assessments because of the large current range (greater than 15 decades) over which DC measurements can be made. Power frequency AC measurements were also made to give a dynamic analysis of the emitter current under both forward and reverse bias conditions. In addition, alternating current measurements provided experimental information as to the emission

current waveform and hence harmonic content. Such information is necessary in assessing the usefulness of a field emission diode as a frequency multiplier.

The low duty cycle pulsed emission[9] current was not measured since the current densities where this becomes necessary were not approached in the present studies.

It is now appropriate to describe the measurement procedures used in detail and to present a body of typical experimental results. These experimental results will then be analyzed in a later section of this chapter.

1. Test Procedures

Before electrical measurements were made, the sample was examined with the SEM to determine its growth characteristics and to provide a basis for the recognition and evaluation of any deleterious effects that might occur during the electrical tests. Since the same mounting pin used in the SEM also fits into the cathode assembly of the test diode, the transfer from the SEM to the test diode was accomplished with little chance of damage to the sample. After the pin holding the sample was placed in the test diode, the interelectrode spacing was adjusted. When the variable spacing diode was used, positioning was accomplished by finding the relative zero position and setting the calibrated dial to the desired spacing. The earlier diode assembly (see Semi-Annual Report[1]) which had no calibrated dial was adjusted

with a thickness gauge and an inside micrometer. Once the interelectrode spacing was set at a preliminary value (which was also the final value in the case of the nonadjustable diode) the test diode was securely bolted into the vacuum chamber and the pumpdown cycle initiated. As discussed previously, approximately 36 to 48 hours were required for the vacuum system to cool and stabilize at a pressure in the 10^{-9} Torr range.

The first series of electrical measurements normally involved the determination of the anode current as a function of various parameters with the range of measurements limited to regimes in which vacuum arcs did not occur. This procedure provided basic test data believed to be free from anomalies that could be caused by vacuum arcs. When sufficient data in this regime had been accumulated, the sample was removed from the test diode for SEM analysis. After SEM analysis the sample was replaced in the test diode and the maximum anode voltage increased and/or the interelectrode spacing reduced until vacuum breakdown occurred or the limit of the power supply capability was reached. The sample was then removed from the test diode for additional SEM analysis. If desired, the electrical test sequence could be broken into several segments interposed with SEM examinations.

The general philosophy of measurement discussed above was implemented with specific experimental techniques. The objective of a particular measurement sequence was first clearly defined. This fixed the parameters to be measured and set limits on other

quantities such as the maximum anode voltage, minimum interelectrode spacing and the maximum allowable pressure rise. Only after this preliminary analysis was completed were the actual measurements made. A detailed summary of the techniques used in the measurement of the various electron emission properties is given below.

(1) The DC electron emission current was measured as a function of the anode voltage (up to the maximum voltage as set by vacuum breakdown or other considerations) for all currents within the range of the electrometer. Measurements were made both in the direction of increasing voltage and in the direction of decreasing voltage. This is necessary since there is apparently some "memory" or hysteresis effect in the current-voltage relationship. Since a protective resistance was employed in series with the test diode, it was necessary to calculate the potential drop across this resistance and subtract it from the power supply voltage in order to get the actual anode to cathode potential. The "reverse" DC emission current was usually measured in addition to the normal or "forward" current. The procedure followed was exactly the same as used for the determination of the forward current, but the power supply and electrometer polarities were reversed.

(2) The AC emission current was measured as a function of the anode voltage by a procedure that is similar to that used for the DC measurements. A Simpson Model 260 Multimeter connected

across the power transformer was used to set the anode voltage. The emission current was determined by monitoring the voltage drop across a known precision resistance with a Tektronix Model 531 Oscilloscope. The presence of hysteresis was detected by following the same procedure used in the DC measurements. Since an AC voltage waveform was applied to the diode, both forward and reverse currents were measured simultaneously.

(3) To make emission current measurements as a function of interelectrode spacing, the anode potential was set to the desired value and the anode position varied with the linear motion feedthrough. Measurements were made in both directions to account for possible electrical hysteresis. No problems due to mechanical backlash in the linear motion feedthrough have been encountered.

It should be noted that all of the above measurements were not made for each data run; only those measurements necessary to attain the experimental objective were performed.

D. EXPERIMENTAL RESULTS AND DIFFICULTIES

This section presents a summary of the typical electron emission performance of the UO_2-W composites and discussion of possible explanations for any unusual performance of these materials. The theory presented in the previous section is correlated with the experimental results wherever possible. Electrical measurements are given along with pre- and post-emission SEM micrographs of the composites that serve to relate the emission

data to the microstructure of the sample. Some major experimental difficulties are also discussed.

1. Experimental Difficulties

Before any detailed discussion of specific experimental results it is helpful to briefly review some of the general problems encountered in the measurement processes. The problem thought initially to be of most significance was that of the nonzero reverse current. It was found that every sample produced a reverse current when the power supply polarity was reversed. Potential sources of such a reverse current include the following: high field emission from the anode, gas breakdown within the vacuum system and leakage currents across the anode-cathode insulators. One unusual property of the reverse current was that it never appeared until an emitter had been operated for approximately 10 hours and its magnitude changed after the occurrence of some unusual event, such as a violent arc, within the test diode. The slow appearance of the reverse current and its subsequent behavior suggested that it was in some way connected with material removed from the sample. This hypothesis was tested in several ways. First, the reverse current was measured as a function of gas pressure. It was found that the reverse current did not increase with pressure, thus providing an indication that gas breakdown was not the problem. The sample used in the gas pressure test was then removed and the diode was operated with a polished Mo cathode, but with the same anode used in the previous test. This anode

bore evidence of a contaminated surface. When the all Mo diode was operated, a small reverse current was initially measured, but no forward current could be detected. After a period of reverse operation a small forward current could also be observed, thus indicating that perhaps some transport of material from the contaminated anode to the polished cathode had occurred. Although the Keithley Model 610 Electrometer had always indicated an interelectrode resistance of greater than 10^{14} ohms, a guard circuit was installed to remove the possibility of leakage currents across the interelectrode insulation. The test diode was then reassembled with no sample and clean polished electrodes. No forward or reverse current or currents in the guard circuit could be detected. This result indicated that the probable source of the reverse current was field emission from a contaminated anode. An x-ray analysis of a previously used anode had shown the presence of U and some W on the anode face. Since the work function of U (3.3 eV) is lower than that of Mo (4.3 eV), the field emission properties of the Mo anode would be enhanced by the presence of the U contamination. It is also possible that electron bombardment produces areas of localized melting on the anode and a subsequent resolidification in a geometrical configuration that realizes a higher local electric field than does the polished plane electrode. In any case, the reverse current has no effect on measurements made in the forward direction since it is present only when the diode polarity is reversed.

Another problem that hampered precise experimental measurements was the inherent instability of the emission current. This fact is perhaps best shown from a consideration of the behavior of a typical sample. When a sample was first installed in the test diode, the measured current would initially be some low value and increase with time. The total increase might be as much as two orders of magnitude over a period of several hours. The current would then stabilize around some average value, but would fluctuate from a few percent to perhaps 50 percent. After several days, the current would finally stabilize to the extent that the maximum fluctuations would be reduced to several percent. However, if the anode voltage were changed, the current would again be initially unstable. Again, after a period of time, the current variations would tend to decrease while the absolute magnitude of the current would increase slightly over the initial value. Thus, measurements made over a long time period during which the current was allowed to stabilize at each value, gave different results from current measurements made over a shorter time period where larger variations in current were observed.

The slow initial buildup of the current density might be explained from a consideration of the variations in pin height. Consider, for example, the case of three pins, two of the same size and one slightly taller. The tall pin would tend to raise the local equipotential around it and depress the potentials of the neighboring pins. This would result in a larger initial electric field at the tip of the taller pin. After a period of

operation, localized heating of the tall pin would tend to reduce its size and blunt its tip due to surface migration[9], or perhaps be destroyed by a vacuum arc[13,14]. Thus the interference effects of the taller pins would be slowly reduced and allow the remaining pins to produce useful emission. It should be emphasized that this explanation is purely speculative in nature.

The reason why the current is unsteady after a change in anode voltage might be explained by reference to Figure 46, which gives the current density as a function of anode voltage with pin radius as a parameter. When the anode voltage is changed, for example from 1000 V to 2000 V, appreciable current is produced by groups of pins with larger radii and pins with smaller radii carry an even greater current. The process of pin tip shaping due to surface migration and/or selective damage can now once more occur. The process continues until a condition of equilibrium is reached at which time the pin current is again stable. This explanation should also be considered of a speculative nature.

2. Typical Emission Results

Typical emission data for three representative samples are discussed below. The general growth parameters of those samples for which data are presented are summarized in Table X.

TABLE X

GROWTH PARAMETERS OF EXPERIMENTAL SAMPLES USED FOR EMISSION STUDIES

Experiment or Sample Number	Growth Designation	Average Pin Tip Radius (cm)	Average Pin Spacing (cm)
2	199	2.1×10^{-5}	6.0×10^{-4}
3	3-1	1.5×10^{-5}	4.0×10^{-4}
4	13-33	0.5×10^{-5}	2.5×10^{-4}

Direct current emission data from Sample No. 2 are presented in Figure 50. Note that a hysteresis effect is visible in the forward current curves and that there is a nonzero reverse current. Alternating current measurements were also made on Sample No. 2 and these results are presented in Figure 51. Figure 51a shows both the forward and reverse currents simultaneously while Figure 51b presents an expanded view of the reverse current. The forward current conduction angle was about 100 degrees, indicating that harmonics higher than the fundamental were present.

Post-emission scanning electron micrographs of Sample No. 2 are shown in Figure 52. As evident from Figure 52a, there is considerable damage to the sample including craters produced by severe arcs. These arcs probably occurred when the diode pressure

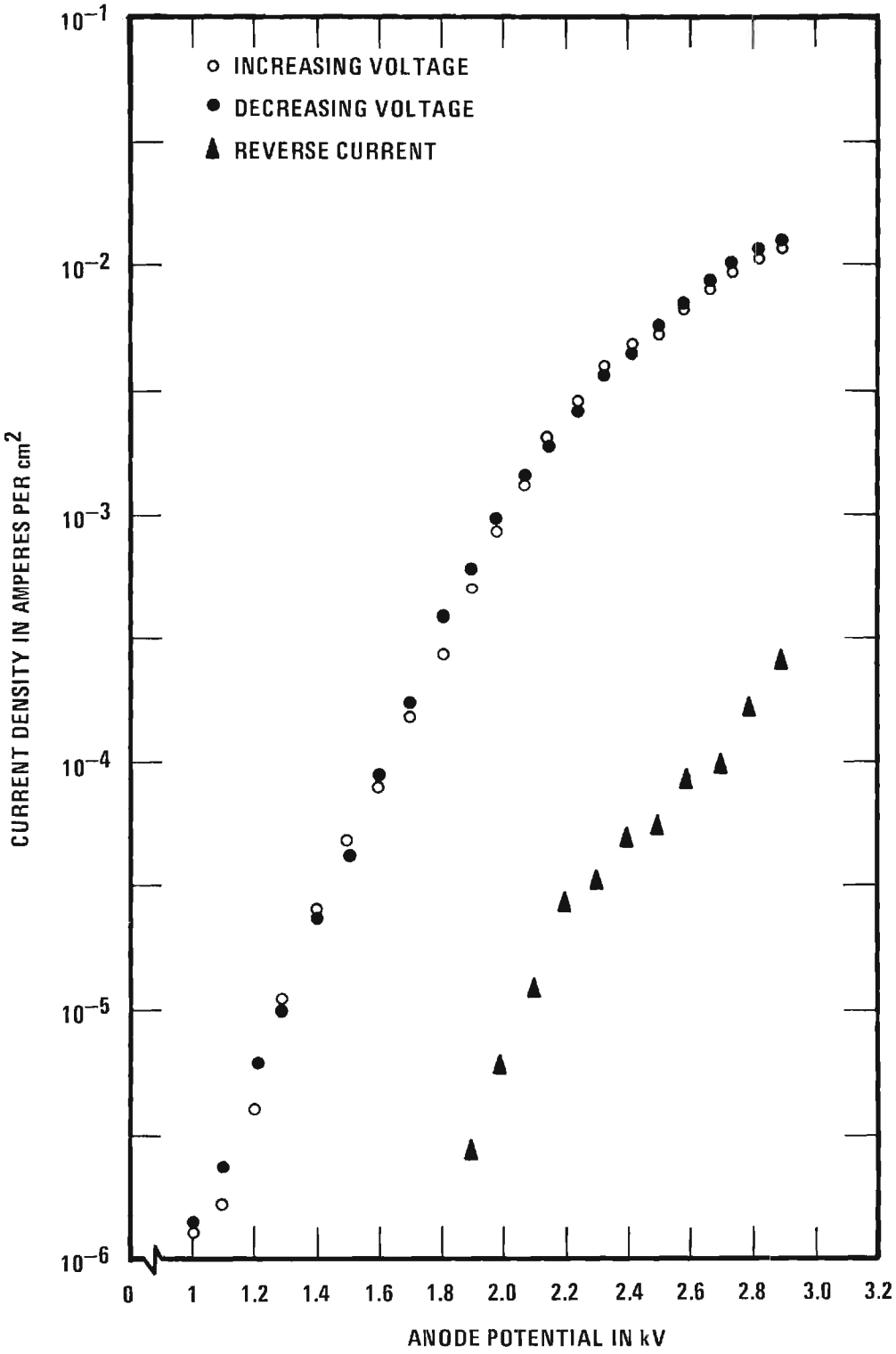

Figure 50. DC Field Emission Current Density as a Function of Anode Potential for Sample No. 2.

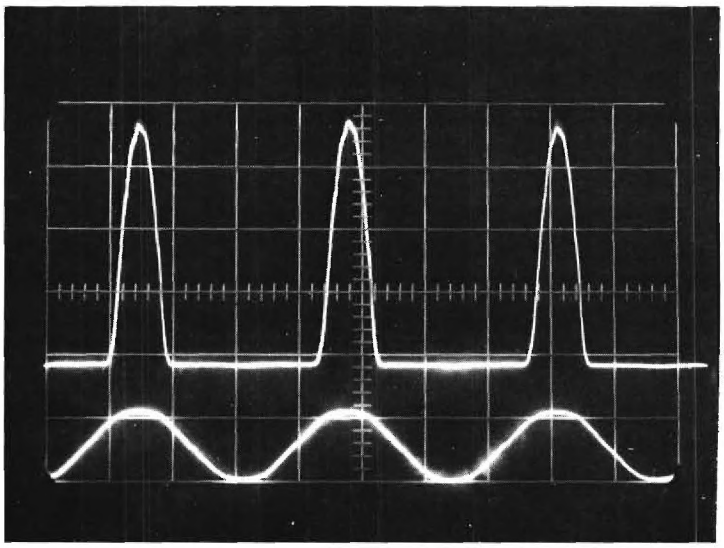

(a) Upper Trace: Anode Current, 2mA per Division. Lower Trace: Anode Potential, 500V per Division.

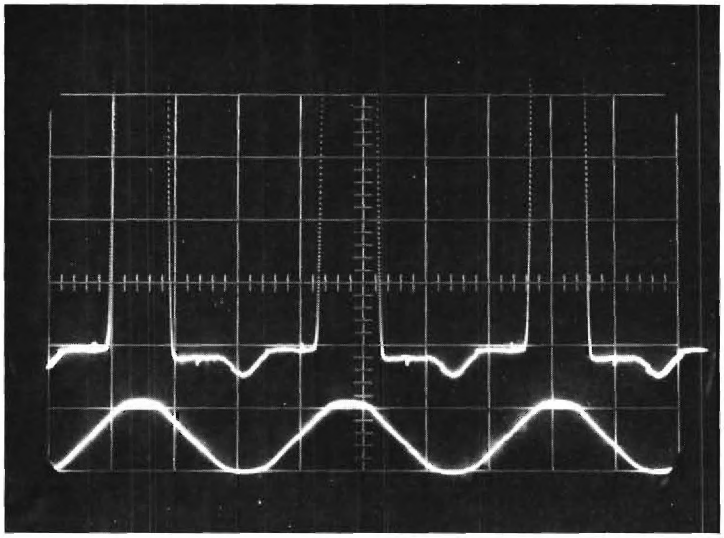

(b) Upper Trace: Anode Current, 100μA per Division. Lower Trace: Anode Potential, 500V per Division.

Figure 51. Field Emission Current as a Function of a Sinusoidal Anode Potential for Sample No. 2. The Active Emitting Area of the Sample Was Approximately 0.3cm^2.

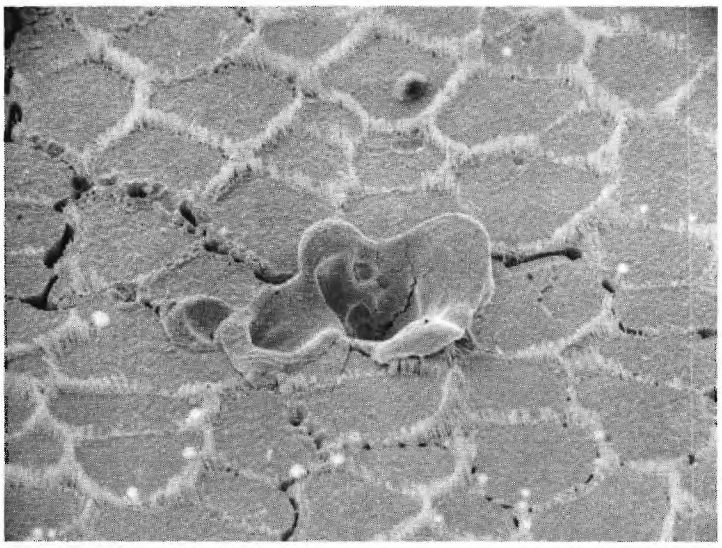

(a) Low Magnification Showing Crater and General Features. 232X.

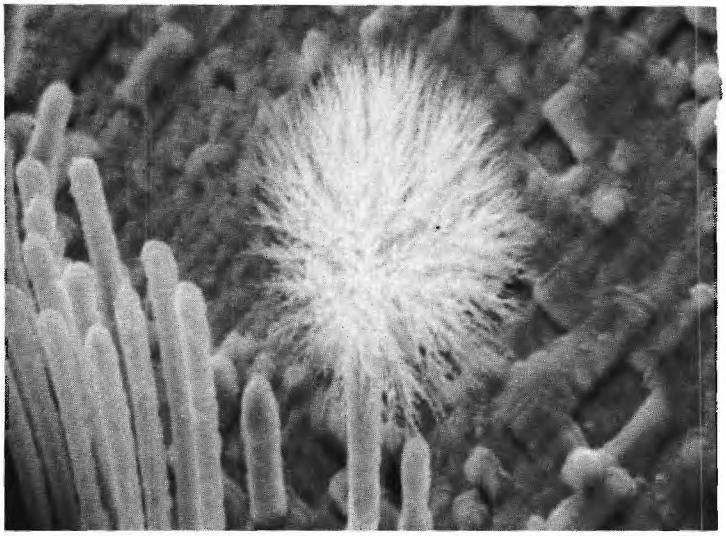

(b) High Magnification Showing Ion Etching of the Matrix and "Exploded" Pin Tips. 3000X.

Figure 52. Scanning Electron Micrographs of Sample No. 2 Displaying Post-Emission Damage.

was intentionally varied from about 3×10^{-8} Torr to almost 10^{-5} Torr. Evidence of ion etching, probably due to the action of the ionized background gas, can be seen in Figure 52b. An unusual feature visible in both Figure 52a and 52b is the occasional ball-like growth at the fiber tips. The origin of these "exploded tips" is unknown.

Although Sample No. 2 was subjected to rather extreme abuse, the major effects upon emission current appeared to be of a transitory nature. After a vacuum arc or gas discharge, the magnitude of the measured current dropped considerably, but increased somewhat after several hours of nondestructive operation. Recovery was never complete, but was always substantial, a typical value being about 50 percent. The reason for this behavior is at present unknown.

Data depicting the emission performance of Sample No. 3 are given in Figure 53. It is seen that these curves qualitatively agree with those for Sample No. 2. Sample No. 3 was subjected to two stages of investigation. The sample was first placed into the diode and operated with a maximum anode voltage in such a manner that the maximum pressure did not exceed 1×10^{-8} Torr. The interelectrode spacing was fixed at 0.010 inch. Figures 54a and 54b show the pre- and post- emission SEM photomicrographs. No evidence of damage to the sample is visible in the micrographs. After the post-emission SEM examination, the sample was returned to the experimental apparatus for further study. When the anode

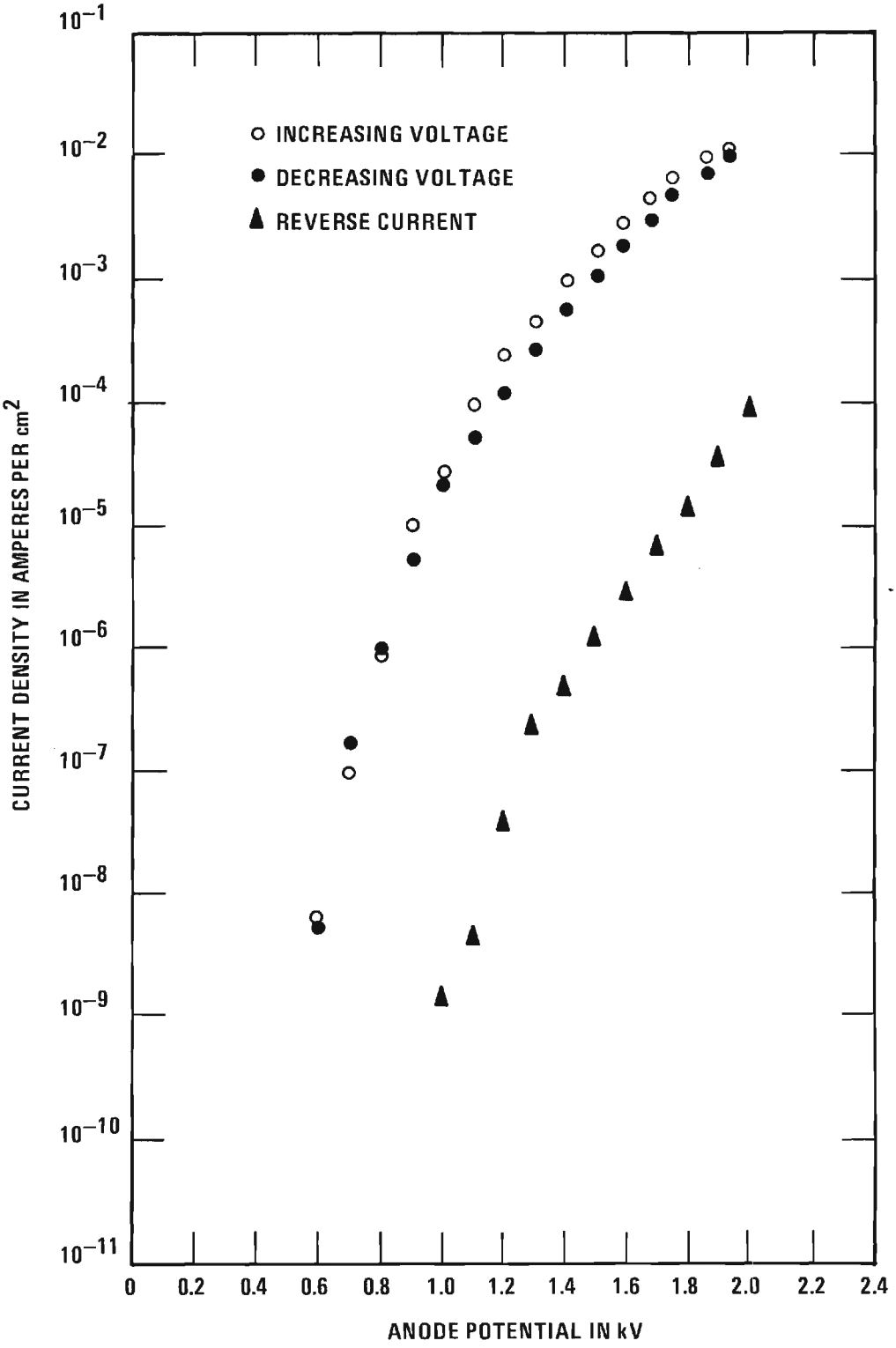

Figure 53. DC Field Emission Current Density as a Function of Anode Potential for Sample No. 3.

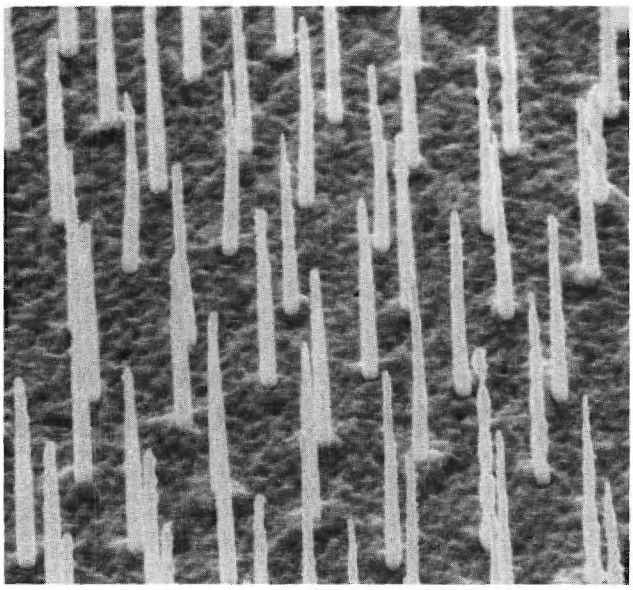

(a) Pre-Emission. 5200X.

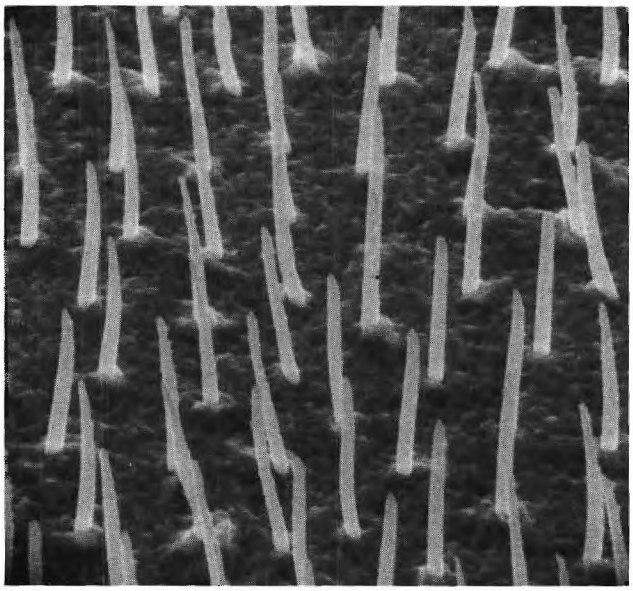

(b) Post-Emission. 5700X.

Figure 54. Scanning Electron Micrographs of Sample No.3.

potential was increased to the limit of the power supply capability (approximately 3.1 kV), the electron emission increased by only a factor of three, an increase much less than anticipated. In addition the maximum attainable current decreased with time to a final value not significantly greater than that previously obtained with a 2.0 kV anode potential. Some external evidence of arcing was noted when the sample was operated at the higher voltages. After the second emission test was completed, subsequent SEM examinations disclosed some interesting features which are shown in Figure 55. There are a few widely scattered craters apparently the result of arcs. No evidence of the matrix etching found on Sample No. 2 was seen. The most interesting damage observed was the presence of a few isolated areas of small size where the W pins were completely "melted down" into the matrix. Surrounding the completely melted pins are a few partially melted pins and other pins that show no apparent damage. This pattern of damage, particularly the partially melted pins, is similar to that observed by Cline[14] in a Ni-W eutectic array. This pin "melt down" can be explained by at least two hypotheses. First it is possible that only a few pins are continuous through the matrix. These few pins carry the total emission current, their tips become hot enough to produce W vapor and a vacuum arc develops selectively destroying the pins. Another hypothesis is that the pin "melt down" occurs in pins having a significantly smaller radius that are perhaps also taller than their neighbors. Joule heating of the pin tips could again lead to a selectively destructive vacuum arc.

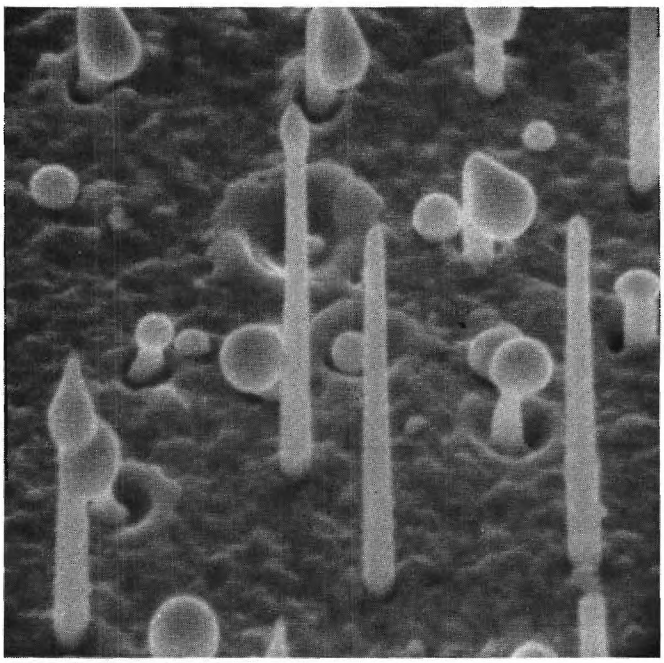

Figure 55. Scanning Electron Micrograph of Sample No. 3 Taken After Second Emission Test Showing Melted and Partially Melted Pins. 10,700X.

Emission data for Sample No. 4 are presented in Figure 56. These data indicate a behavior similar to that noted in previous samples. The reverse current which is not shown was always less than one percent of the forward current. Figure 57 shows the variation of the measured anode current density as a function of the interelectrode spacing with constant anode potential. This variation agrees qualitatively with that predicted by Equation (30), but is more directly obvious if Equation (30) is simplified for the typical minimum interelectrode spacings and growth parameters of the present work. One then obtains,

$$J = C_3 \frac{1}{L^2} \exp(-C_4 L) \qquad \text{(Eq. 31)}$$

where C_3 and C_4 are constants for a particular pin radius, anode voltage and pin spacing. Since the range of variation of L in Figure 57 is less than ten to one, the exponential clearly dominates and the behavior of J as a function of L should approximate a straight line as shown in Figure 57. Micrographs of Sample No. 4 both before and after the electron emission test are shown in Figure 58. The pins originally were almost conical with tip radii of approximately 5×10^{-6} cm.* After the emission test, some of the pins had been melted down into the substrate in a manner similar to Sample No. 3.

*This sample was chemically etched using the procedures described in Section IV, Chemical Etching of UO_2-W Composites, to intentionally sharpen the individual tungsten pins.

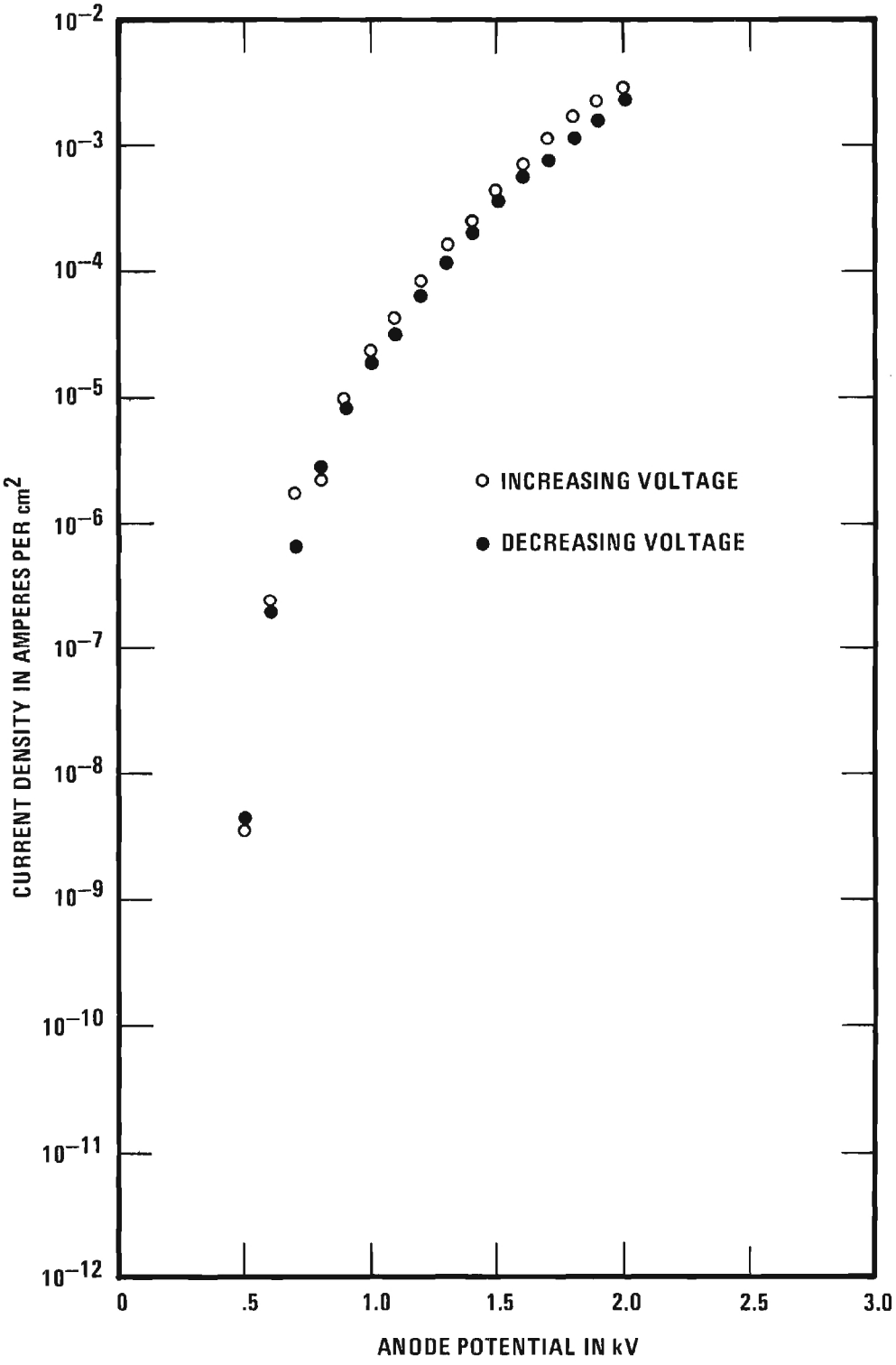

Figure 56. DC Field Emission Current Density as a Function of Anode Potential for Sample No. 4.

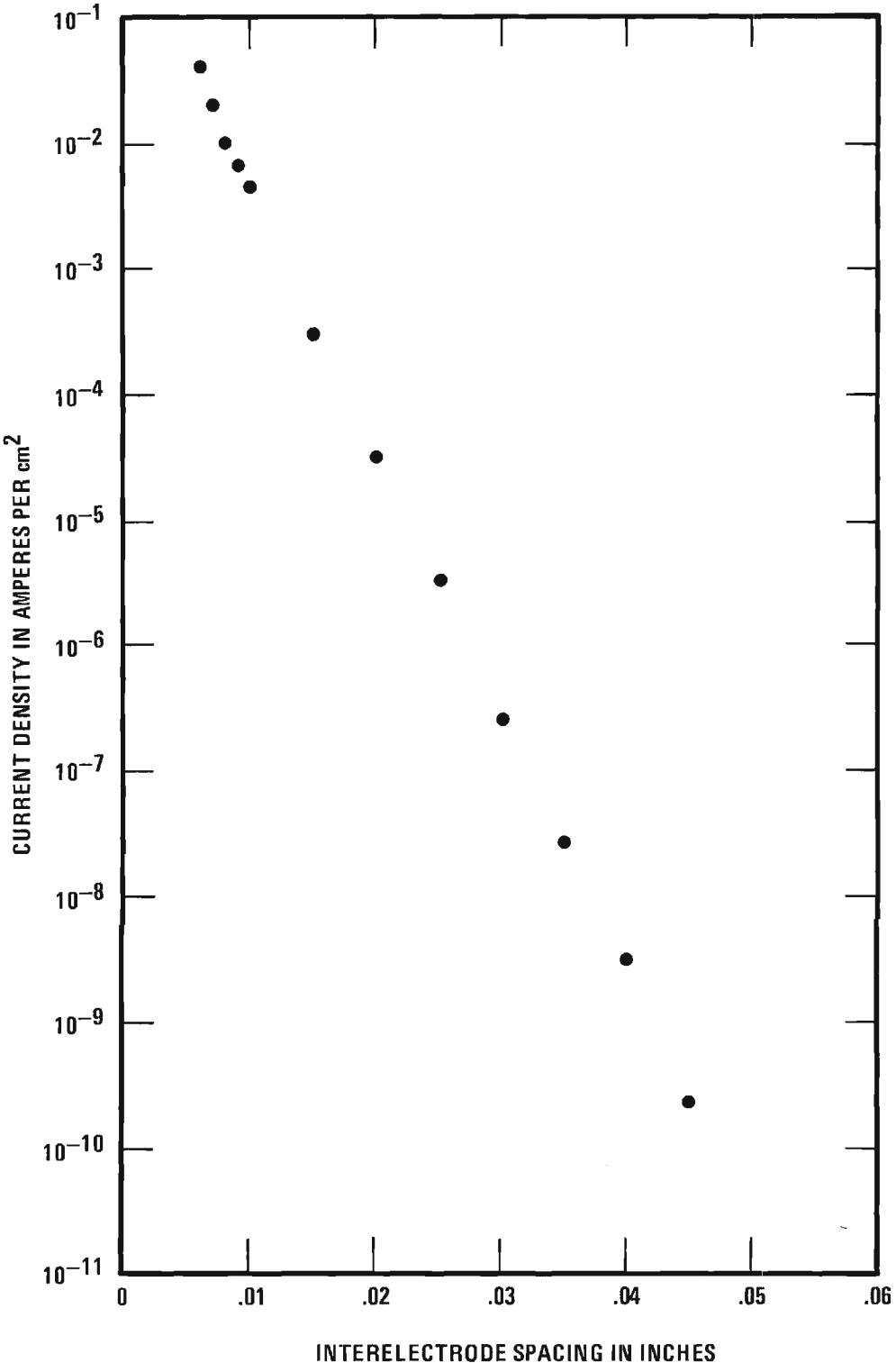

Figure 57. Current Density as a Function of Interelectrode Spacing for Sample No. 4. The Anode Potential Was Fixed at 2000 Volts.

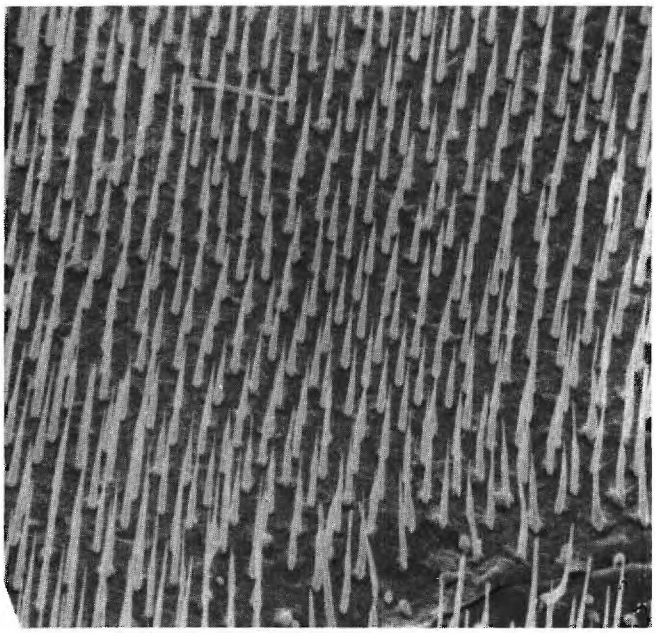

(a) Pre-Emission. 1750X.

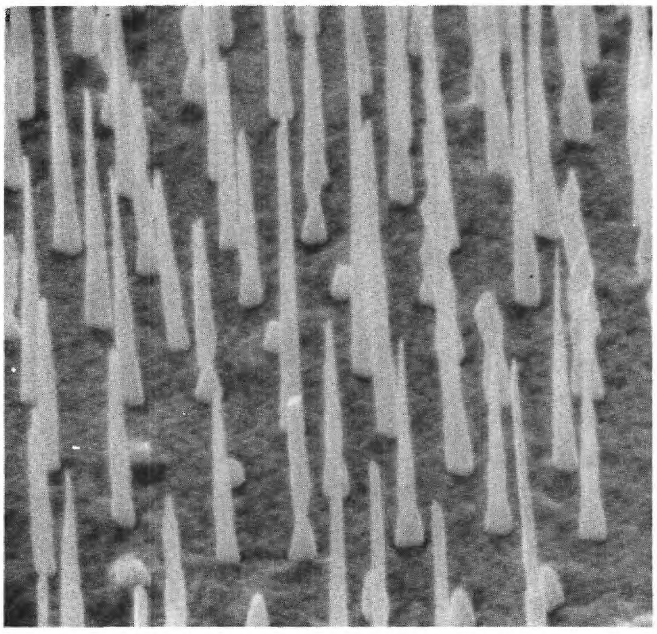

(b) Post-Emission Showing Melted and Partially Melted Pins. 5650X.

Figure 58. Scanning Electron Micrographs of Sample No. 4.

SECTION VI

SUMMARY

During the last year, work has been underway on ARPA Order No. 1637 for the development of melt-grown oxide-metal composites containing between 4 and 50 million less than 1μ diameter tungsten fibers per square centimeter, uniformly embedded in an oxide matrix, and the evaluation of these materials for electron emission applications. The research program is divided into four areas to meet the project objectives:

1. Induction Coupling and Solidification Behavior of Oxides and Oxide-Metal Mixtures.
2. Structural and Chemical Characterization of Oxide-Metal Composites.
3. Composite Growth in Oxide-Metal Systems and the Formation of Optimum Emitting Arrays.
4. Field Emission Theory and Experimental Results.

A number of oxides, oxide compounds and oxide-oxide and oxide-metal mixtures were tested to determine their suitability for induction melting using high frequency rf heating. Only ZrO_2 (CaO or Y_2O_3 stabilized), WO_3, Pr_2O_3, NiO, Cr_2O_3, TiO_2, CeO_2, ZnO-TiO_2 and ZnO-Al_2O_3 mixtures, $BaFe_{12}O_{19}$, Fe_2TiO_5 and $NiTiO_3$ were melted from the many materials tested; and, of this list, only the stabilized ZrO_2, CeO_2 and $NiTiO_3$ established stable

enough molten geometries to warrant further study with metal additions.

Several approaches including higher preheat temperatures (designed to decrease the resistivity of the oxides) were employed to increase the probability of melting the high resistivity oxides. $BaZrO_3$ which could not be coupled to after preheating to 1400°C and exposure to a 27 mhz rf field was successfully heated by a rf field after preheating to 1900°in a glassy carbon tube.

Mixtures of UO_2-W and stabilized ZrO_2-W readily form eutectic structures; however, very limited success in forming ordered structures was achieved using other metal additions (i.e. Mo, Ta, Nb) with these oxides. An analysis of some of the difficulties encountered in internally melting pure oxides and and oxide-metal mixtures with rf heating and future approaches designed to increase the list of materials which may be induction heated are presented.

Techniques and procedures which provide adequate characterization of oxide-metal composites and the structural and chemical information necessary to interpret these structures were developed using scanning electron microscopy (SEM), non-dispersive x-ray analysis, and x-ray diffraction. Scanning electron micrographs were used to analyze the various oxide-metal structures and the growth modes of individual tungsten fibers. Mutual oxide-metal orientation relationships were

determined in selected UO_2-W samples and show the dominant growth direction to be [111] for the UO_2 matrix and [110] and [100] for the tungsten fibers.

The growth of UO_2-W and stabilized ZrO_2-W has progressed to the point where an analysis of the solidification behavior can be made by varying controllable parameters. The influence of growth rate on tungsten fiber density and diameter was established in the system UO_2-W. Fiber diameters between 0.28 and 0.49 microns and fiber densities between 15 and 42 million per cm^2 were achieved. Major progress has been made in establishing the growth conditions suitable for melting stabilized ZrO_2-W mixtures, and composite samples containing approximately 13 million 0.60 micron diameter fibers have been grown.

The chemical etching technique used to dissolve the surface of the oxide matrix and expose the W fibers for emission testing and analysis in the SEM is described. Additional etching techniques directed towards "pointing" the exposed tungsten pins for enhanced emission performance have been very successful. Initial attempts to selectively dissolve the metal fibers from the oxide matrix are also described.

Preliminary experimental results indicate that the UO_2-W composite materials have considerable potential as field emission cathodes. Emission current densities approaching 0.1 A/cm^2 have

been obtained with anode voltages of less than 3 kV and inter-electrode spacings of approximately 0.01 inch.

The field emission current has been measured as a function of applied voltage for several composite emitters with different growth parameters. Anomalies in the emission behavior of the material have been noted and several hypotheses developed to explain the observed effects.

A mathematical model that qualitatively predicts how the emission characteristics vary with pin spacing, pin radius, electrode spacing and anode voltage has been developed. The effects of a pin tip radius distribution, the possible nonuniformity of pin emission and the presence of adsorbed gases have been included in the mathematical model.

REFERENCES

1. A. T. CHAPMAN, et. al., "Melt-Grown Oxide-Metal Composites", Report No. 1, ARPA Contract DAAHOI-70-C-1157, January 1971.

2. A. T. CHAPMAN, et. al., J. Am. Cer. Soc., 53 (1) 60 (1970).

3. M. D. WATSON, et. al., J. Am. Cer. Soc., 53 (2) 112 (1970).

4. D. N. HILL, "Internal Zone Melting of Refractory Oxides Using Induced Eddy-Current Heating," M. S. Thesis, School of Ceramic Engineering, Georgia Institute of Technology, September 1969.

5. A. T. CHAPMAN and G. W. CLARK, J. Am. Cer. Soc., 48 (9) 494 (1965).

6. B. HONIGMANN, Gleichgewichts-Und Wachstumsformen von Kristallen, Steinkopff Verlag, Darnstadt, (1958).

7. M. G. FONTANA, Ind. and Eng. Chem., 44 (1) 91A (1952).

8. J. D. LEVINE, RCA Review, 32 144 (1971).

9. W. P. DYKE and W. W. DOLAN, Adv. Elect. and Elect. Phys., 8 89 (1956).

10. A. G. P. VAN OOSTROM, Philips Res. Repts. Suppl., 1 1 (1966).

11. R. GOMER, Field Emission and Field Ionization, Harvard University Press, Cambridge, Mass. (1961).

12. D. MENZEL and R. GOMER, J. Chem. Phys., 41 3311, 3329 (1964).

13. M. P. REECE, Proc. IEE (London), 110 796 (1963).

14. H. E. CLINE, J. Appl. Phys., 41 76 (1970).

DISTRIBUTION LIST

DISTRIBUTION	NO. OF COPIES
DIRECTOR ADVANCED RESEARCH PROJECTS AGENCY ATTN: PROGRAM MANAGEMENT DR. M. J. SINNOTT WASHINGTON, D. C. 20301	5
COMMANDING GENERAL U.S. ARMY MISSILE COMMAND ATTN: AMSMI-RND REDSTONE ARSENAL, ALABAMA 35809	20
DEFENSE DOCUMENTATION CENTER CAMERON STATION ALEXANDRIA, VIRGINIA 22314	20
COMMANDING GENERAL U.S. ARMY MATERIAL COMMAND ATTN: AMCRD-PT WASHINGTON, D. D. 20315	1

Unclassified

Security Classification

DOCUMENT CONTROL DATA - R & D

(Security classification of title, body of abstract and indexing annotation must be entered when the overall report is classified)

1. ORIGINATING ACTIVITY *(Corporate author)*

School of Ceramic Engineering
Georgia Institute of Technology

2a. REPORT SECURITY CLASSIFICATION

Unclassified

2b. GROUP

3. REPORT TITLE

MELT-GROWN OXIDE-METAL COMPOSITES

4. DESCRIPTIVE NOTES *(Type of report and inclusive dates)*

Final (10 June 1970 - 9 June 1971)

5. AUTHOR(S) *(First name, middle initial, last name)*

Alan T. Chapman, James F. Benzel, Robert K. Feeney, Reiner J. Gerdes, John W. Hooper

6. REPORT DATE	7a. TOTAL NO. OF PAGES	7b. NO. OF REFS
July 1971	127	14

8a. CONTRACT OR GRANT NO.	9a. ORIGINATOR'S REPORT NUMBER(S)
DAAHOI-70-C-1157	B414-2
b. PROJECT NO. PAN W699	
c.	9b. OTHER REPORT NO(S) *(Any other numbers that may be assigned this report)*
d.	ARPA ORDER NO. 1637

10. DISTRIBUTION STATEMENT

This document may be further distributed by any holder only with the specific prior approval of Director, Advanced Research Projects Agency, 1400 Wilson Blvd., Arlington, Virginia 22209.

11. SUPPLEMENTARY NOTES	12. SPONSORING MILITARY ACTIVITY
	Advanced Research Projects Agency 1400 Wilson Blvd. Arlington, Virginia 22209

13. ABSTRACT

Research was initiated to understand and control the parameters leading to the successful growth of refractory oxide-metal composites consisting of small metal fibers uniformly embedded in the oxide matrix, and to evaluate the electron emission performance of these structures. Numerous oxides, binary oxide compounds, oxide-oxide and oxide-metal mixtures were tested to determine their suitability for induction melting using rf frequencies between 3 and 32 mhz. Procedures employing scanning electron microscopy and x-ray diffraction were developed to characterize oxide-metal composite samples. Metallic fiber shapes have been related to crystallographic morphology. Mutual oxide-metal orientations were determined in selected UO_2-W samples. The influence of growth rate on W fiber density and size was studied in the system UO_2-W. Extensive areas of uniform W fiber growth were achieved in the stabilized ZrO_2-W system. Chemical etching techniques have been developed to shape tungsten pins for enhanced electron field emission. A theoretical analysis of expected electron field emission from an array of metallic pins has been performed using pin geometries and electrical variables. Suitably prepared UO_2-W samples were tested in a simple diode geometry and field emission performance measured as a function of voltage and interelectrode spacing. Post-emission damage to the composite structures has been analyzed. (U)

DD FORM 1 NOV 65 1473 (PAGE 1)

S/N 0101-807-6801

Unclassified

Security Classification

14 KEY WORDS	LINK A		LINK B		LINK C	
	ROLE	WT	ROLE	WT	ROLE	WT
Oxide-Metal Composites		4				
Field Emission		4				
Rf Heating		3				
Fiber Growth Forms		2				
Emission Theory		3				
Oxides		2				
Refractory Metals		2				
Unidirectional Solidification		4				
UO_2		2				
ZrO_2 (Stabilized)		1				
Internal Melting		3				
Etching		2				
Tungsten Fibers		4				
Electron Emitting Arrays		4				
Oxide-Metal Solidification		3				
High Field Emission		4				